國立交通大學

光電工程研究所

博士論文

次世代高效率氮化鎵發光二極體之奈米製程與元件特性之研究

Study of Nanofabrication Techniques and Device Characteristics of High Efficiency GaN-based Light Emitting Diodes for Next-generation Solid State Lighting

研究生:	邱清華	Student:	Ching-Hua Chiu
指導教授:	郭浩中 教授 余沛慈 教授	Advisor:	Dr. Hao-Chung Kuo Dr. Peichen Yu

中華民國九十八年十二月

次世代高效率氮化鎵發光二極體之奈米製程與元件特性之研究

Study of Nanofabrication Techniques and Device Characteristics of High Efficiency GaN-based Light Emitting Diodes for Next-generation Solid State Lighting

研究生：邱清華
指導教授：郭浩中 教授
余沛慈 教授

Student：Ching-Hua Chiu
Advisor：Dr. Hao-Chung Kuo
Dr. Peichen Yu

國立交通大學 電機資訊學院
光電工程研究所
博士論文

A dissertation
Submitted to Institute of Electro-Optical Engineering
College of Electrical Engineering and Computer Science
National Chiao Tung University
in partial Fulfillment of the Requirements
for the Degree of
Doctor of Philosophy
in

Electro-Optical Engineering

November 2009

Hsinchu, Taiwan, Republic of China

中華民國九十八年十二月

次世代高效率氮化鎵發光二極體之奈米製程與元件特性之研究

學生：邱清華　　　　　　　　　　指導教授：郭浩中 博士
余沛慈 博士

國立交通大學光電工程研究所

摘　要

近年來，三五族半導體尤其是氮化鎵材料系列由於發光波長涵蓋了短波長的紫外光波段和大部分的可見光，其相關的光電元件如發光二極體、雷射和光偵測器等元件被大量的研究，同時這些光電元件被大量的應用在新一代光儲存、平面顯示、生物檢測和照明等光電產品中，也由於新的應用產品刺激下，氮化鎵材料的研究越來越受到大家的重視。

本論文主要在於開發製作氮化鎵奈米結構並應用奈米結構於氮化鎵發光二極體元件上，同時研究奈米發光元件及結構之製作、材料特性、及光電特性。主要分為四個部分，第一部份為開發一個新穎性的奈米結構製作技術，用以製作氮化鎵奈米柱結構。利用調變製程參數得到不同形狀的奈米結構，針對不同深度、不同直徑大小的奈米助陣列探討其發光特性、抗反射特性，同時利用 valence force field (VFF)模型瞭解氮化鎵材料在應用釋放過程中對材料特性的影響為何。第二部分為應用奈米結構在氮化鎵發光二極體上，利用表面蝕刻技術，製作高深寬比的氮化鎵奈米結構提升元件出光效率。在考量到蝕刻對元件可能的電性影響後，我們嘗試了化學合成的方式，在元件表面上化學合成氧化鋅奈米柱結構降低表面全反射以提升元件萃取效率。最後我們結合了再磊晶的技術，在 SiO_2 奈米柱結構上進行再磊晶同時改善元件內部量子效率和光萃取效率。

在本論文的後半部，我們針對氮化鎵發光二極體的內部量子效率進行研究，採用了圖案化基板的方式提升元件的內部量子效率。在第三部分，我們改善了傳統光學方法量測內部量子效率的方法，首先調變激發雷射的光波長，接著利用一連串的變溫和變功率光學方法定義並量測元件內部量子效率，同時分析了在光學量測過程中內部載子發光機制等特性。在本論文的最後一部分，延續內部量子效率的研究議題，我們建立了一套可控制環境溫度的電注入量測設備，這將幫助我們進行一系列不同溫度和電流注入下的效率量測，不僅可幫助我們更瞭解內部量子效率的變化情形，更可對高電流注入下效率急

降的有更深入的瞭解。同時，利用 APSYS 模擬軟體模擬低溫下元件的行為，對次世代高效率元件的設計和製作有絕對的幫助。

Study of Nanofabrication Techniques and Device Characteristics of High Efficiency GaN-based Light Emitting Diodes for Next-generation Solid State Lighting

Student: Ching-Hua Chiu
Advisor: Dr. Hao-Chung Kuo
Dr. Peichen Yu

Institute of Electro-Optical Engineering
National Chiao Tung University

Abstract

Recently, Nitride (III) light-emitting diodes (LEDs) with emission wavelength ranging from ultraviolet to the short-wavelength part of the visible spectrum have been intensely developed in the past 10 years. Due to the rapid developing in efficiency improvement, applying the opto-electronic device such as LED, laser and photo-detectors into our life becomes possible. Besides, because of the next generation application in optical storage, flat display, bio-detection and general lighting, the research about GaN lighting devices attracted more and more attentions.

In this study, we mainly focus on developing GaN nano structures and applying these nano structures on GaN LED. The device fabrication process, efficiency improvement, material and opto-electronic characteristics of the nano-structured GaN-based LEDs will be also discussed. The entire dissertation could be divided into four parts. The first is developing a novel GaN nano structure fabrication process. By well control the metal depositing thickness, annealing temperature, etching conditions, we could achieve different length and diameter GaN nanorod arrays. The emission and anti0refelction characteristics of the fabricated nanorod structures will be discussed. Besides, we applied the valence force field model to help us to realize the influence of strain relaxation within GaN multiple quantum wells (MQWs).

The second part of this dissertation is applying these nano structures on the surface of GaN-based LEDs to improve the lighting efficiency. We first utilizing etching method assisted by spinning nano spheres on device surface serving as masks to form high-aspect-ratio GaN nanorods. However, considered the possible deterioration of reduced current spreading paths, we then adopted a bottom-up method to synthesize ZnO nanorod on the surface to suppress the total internal reflection and improve the light extraction efficiency.

The third method we used to improve the device performance is combing the overgrowth technique on nano-patterned sapphire substrate to improve the internal quantum efficiency (IQE) and light extraction efficiency simultaneously.

At the later half of this dissertation, we focused on the studying of the IQE performance of GaN-based LEDs. We grow our LED structure on the patterned sapphire substrate (PSS) and an increment in IQE is expected. In the third part of this study, we modified the traditional method for IQE measurement. We firstly modify the excitation laser wavelength and a serious of power and temperature dependent study was performed to define the IQE of LED device. The internal carrier lighting mechanism was also studied. The last part of this dissertation is based on the third part but a electrical injection setup was established. This instrument enabled us doing a serious of temperature and injection current dependent measurement. It not only helped us understand more about the IQE, but also well for discovering the origins of efficiency droop phenomenon. Besides, simulation software of APSYS was also performed to simulate the device performance under different temperature. The output of this dissertation provided a great help on realizing the solid state lighting in next generation.

誌 謝

回首三年多來的博士生生涯，一切好像昨日發生的事一般，一幕一幕浮現在眼前，好像很遙遠，卻又清晰的像昨天才發生的一樣。回想這博士生涯，一路跌跌撞撞走來，到了畢業這天，要感謝的人實在太多了，能夠在這個大家庭學習成長，真的是一件很幸福的事，王老師的笑聲永遠那麼開朗，每次聽到都讓我覺得人生永遠充滿希望；郭老師待人處事和做研究的方法一直是我們學習的最佳榜樣，真的讓我學到很多書本以外的知識，看到一個更大的世界；盧老師對研究和教導學生的熱情讓學生學習到很多，每次和老師討論都可以從老師身上學習到很多；最後要感謝余老師對我研究內容的包容和指導，每次和您的合作都讓我獲益良多，讓我學習到做研究的態度和方法。

謝謝實驗室一起合作努力的學長、同學和學弟們，謝謝小強、小朱、泓文、佳恩、逸駿、主力、小賴、德宗、鴻儒、鎮宇和亞儒學長的指導和幫忙，讓我從什麼都不懂得新生到今天能夠順利畢業，尤其小強、小朱和泓文學長更是在我最矇懂無知和無助的時候帶我走出困境最重要的學長，主力學長在製程的大力幫忙和李博的專業討論，讓我論文能夠順利產出，真的謝謝你們。還要謝謝我的同學們，士偉、明華、俊榮、碩均和振昌，一起分擔老師交代的工作，一起承受老師的砲火，雖然我早一點點離開，但我相信你們一定馬上就會畢業，我們再一起在外面打拼！另外感謝跟我一起努力的學弟妹們，閔安、Joseph、鏡學、幸助，你們之後要辛苦一點了，但我相信現在的努力總有一天會有回報的，實驗室的榮景以後就要靠你們維持了；還要謝謝昀恬、柏駿、承恩、恕帆、小柯、政暐、治凱、睿中、勁生、小昕、阿菲、家齊、佑國、瑋庭、育霖和大為，跟你們一起合作的經驗真的很難得，有你們的努力付出和合作，才能有那麼多論文的產出，我才能順利的畢業；還要感謝這幾年來在實驗室許許多多的學弟妹們，像是輝閔、金門、孟儒、子維、晁恩、阿綱、小馬、玫君、依嚀、哭哭、嗡嗡嗡、阿翔、獸皇、詳淇、小邱，雖然沒有和你們真的合作過，但是因為你們，實驗室多了許多歡樂，讓每天的生活都多采多姿，豐富了我的博士生涯。

另外還要感謝在我博士論文研究中曾經幫助過我的老師們，感謝台大吳育任老師在理論和模擬上的幫忙；台大黃建璋老師在奈米球技術的支持和去張家界開會時對我的照顧；成大張守進和賴韋志老師在研究上和計畫上的支持和幫忙；清大吳孟奇老師在我博士口試時的指導；長庚郭守義老師研究上的討論和去上海開會時對我的照顧，真的謝謝各位老師的幫忙，才能讓我順利畢業。

最後要感謝我的家人，我的父母和兩位哥哥，因為有你們的支持，我才能全心全力的投入在我的博士研究中，可以沒有後顧之憂的為研究而努力付出，還有小豬，我們在一起已經六年多了，我的大學、研究所和博士班都是在你的陪伴下完成的，真的謝謝你對我的包容和照顧，希望我們未來還是能夠一直快樂的一起走下去。

清華　　于 98 年 12 月 22 日
交通大學光電所

CONTENTS

Reference

Reference

List of Figures

Chapter 1

Chapter 2

Chapter 3

Chapter 4

Chapter 5

CHAPTER 1

Introduction

1-1 Wide bandgap III-N materials

Wide bandgap nitride materials have attracted great attention over the past decades. The bandgap of the III-nitrides like AlN, GaN and InN material cover a very wide range from 0.9 to 6.1 eV which represents the emission wavelength from deep ultraviolet (UV) to infrared (IR) region as shown in figure 1.1. This wide emission wavelength range makes it promising for applying in the applications of optoelectronic devices such as flat panel display, competing storage technologies, automobiles, general lighting and biotechnology, and so on [1-4]. It is worth noting that as the rapid developing of the blue region material research, we are able to fill up the visible light gap and make the full color display by semiconductor material becomes possible. Besides, the emitted short wavelength light in the blue and UV region is especially suitable to pump up the yellow light and comes out a white light output by mixing the original blue source and excited yellow light which realized the solid state lighting. The III-nitride semiconductor material enjoyed some unique properties that not only suitable for lighting source in short wavelength in visible region but also high-speed/high-power electron device [5]. For example, it has high bond energy (~2.3 eV), high-saturation velocity (~2.7 x 10^4 cm/s), high-breakdown field (~2 x 10^6 V/cm), and strong excitonic effects (>50 meV) [6-7]. However, considered as a next generation high efficiency lighting devices, III-nitride semiconductors have some inherent drawbacks to deteriorate the lighting efficiency like internal piezoelectric field and spontaneous polarization at heterointerface leading to the quantum confined Stark effect (QCSE) and causing charge separation between electrons and holes in quantum wells [8-9]. Even though, it is still worth to devote more effort to overcome such problems for its great potential for realization of next generation solid state lighting.

1-2 GaN-based LEDs

Basically, the blue GaN-based LED confronts some severe problems lowering the efficiency and hindering the realization of solid state lighting. Lack of suitable substrate for GaN epitaxy is the most important issue. Nowadays, GaN material was grown on sapphire susbtrate, which has a 15% smaller lattice constant than GaN, and different thermal expansion coefficient. That leads to a very high defect density and cracking of the layers when the structures are cooled down after growth. The problem was firstly solved by Amano and

Akasaki by designing and growing a AlN buffer layer in 1986 [10]. Also, Nakamura grew GaAlN buffer layers on top of sapphire in 1991 [11] which make it possible to grow GaN on sapphire. In addition to the invention of buffer layer, Prof. S. Nakamura also solved the high growth temperature problems by his two-flow growth reactor which opens the door of high quality GaN material on sapphire [12].

The third problem of for GaN-based LED is p-type doping. Every semiconductor lighting device needs p-n junctions. Previous to Akasaki's work p-type doping of GaN was impossibly. Akasaki (1988 at Nagoya University) found that samples after Low Energy Electron Beam Irradiation treatment (LEEBI) showed p-type conductivity [13-14]. Thus Akasaki demonstrated that in principle p-type doping of GaN compounds was possible. Nakamura was then found the solution to the puzzle of p-type doping. He found that previous investigators had annealed the samples in Ammonia (NH_3) atmosphere at high temperatures. Ammonia dissociates above 400 ^{o}C, producing atomic hydrogen. Atomic hydrogen passivates acceptors, so that p-type characteristics are not observed. Nakamura solved this problem by annealing the samples in Nitrogen gas, instead of Ammonia [15].

Benefit by the effort of such pioneers, the blue GaN-based light emitting diode (LED) is now successfully commercialized. The typical structure of a blue GaN-based LED is illustrated in figure 1.2. The layer of n-type GaN contains an excess of electrons, whereas the p-type layer is a region from which electrons have been removed (i.e., in which "holes" have been formed). If a forward bias is applied, electrons and holes can recombine, releasing energy in the transition layer in the form of light. The energy of the photon corresponds to the voltage bias in the transition region (the "bandgap"). Sapphire and silicon carbide are often used as substrates, which allow for large-area heteroepitaxial growth.

1-3 GaN Nano-structures

By the rapid developing of nano-structure fabrication techniques, we are now having the ability to fabricate GaN nano-structures. It is believed that nano-structures have totally different properties than the bulk material, so that attracted considerable interest for potential application to electronic and optoelectronic devices. By well control and shrink the structure sizes, we could not only save space and increase the capacity of a single chip, but also brings the benefits of quantum effects. The term we called "nano-structures" in this thesis means that one or more dimensions have been restricted to lengths in the order of the mean free path of charge carriers or excitons in the material. In general, the electron Fermi wavelength was far shorter than the size of bulk material so we could not observe the quantum confinement effect.

However, if we could condense one direction size smaller than the Fermi wavelength that the electron was forced to be freely moved in other two dimensions as shown in figure 1.3; such structure was called as a quantum well system. Furthermore, once there was a system with sizes smaller than the Fermi wavelength in two directions; we called it quantum wire. Of course, if we are able to reduce the structure size smaller than one wavelength in three directions, that was called as quantum dot. Actually, we had applied the concepts of nano-structure to modify and improve the device performance in many electronic or lighting devices like quantum wells in LED. It benefits to confine the electrons and holes in the quantum wells and improve the lighting efficiency effectively.

1-4 Overview of this thesis

This study has focused on fabricating a high efficiency GaN-based LED for next generation solid-state lighting by applying nanotechnology. The nanofabrication techniques and the device characteristics will be discussed in the thesis.

Since the overall efficiency of a LED could be viewed as a product of internal quantum efficiency (IQE) and extraction efficiency (ExE), we should put attention on both sides to meet the requirement of next-generation lighting devices. Therefore, the chapter 2 in this thesis will first introduce some nano-structures fabrication process and the characteristics including the comparison between nano-structure and bulk materials. Some simulation was performed to help understanding the inside information. Chapter 3 reports some high efficiency GaN-based LEDs employing nanotechnologies to improve the lighting efficiency. There are three different kinds of high efficiency LEDs demonstrated in this chapter. We first combined wafer bonding and laser lift-off (LLO) techniques to form a vertical-injected LEDs. Then, two methods to form high aspect ratio GaN nanorod by inductively coupled plasma (ICP) etching and ZnO nanorod by synthesizing in aqueous solution at room temperature. Both of them could help a lot to improve the ExE effectively. Third, by applying the nanorod fabrication technique shown in chapter 2, we form SiO_2 nanorods on the sapphire surface and regrowth GaN epi-layers on top of it. It not only improves the crystal quality but also benefits to ExE as well. The details of fabrication and device characteristics will be shown in this chapter.

For IQE issues, we had established an IQE measurement system by both photoluminescence (PL) and electroluminescence (EL) methods. The facilities and IQE measurement mechanism will be introduced in chapter 4. In chapter 5, we compared the IQE characteristics of two set of samples, LEDs on pattern sapphire substrate (PSS) and with different quantum well thickness by PL and EL methods, respectively. It not only helps to realize the IQE but also the efficiency droop performance. Finally, chapter 6 is the summary of this thesis.

Reference:

1. S. Nakamura, M. Senoh, N. Isawa, and S. Nagahama, Japan Journal of Applied Physics **34**, L797 (1995)
2. S. Nakamura, T. Mukai, and M. Senoh, Applied Physics Letter **64**, 1687 (1994)
3. S. Nakamura, M. Senoh, S. Nagahama, N. Iwasa, T. Yamada, T. Matsushita, Y. Sugimoto, and H. Kiyoju, Applied Physics Letter **70**, 868 (1997)
4. S. Nakamura, Science **281**, 956 (1998)
5. Y. Arakawa, IEEE Journal of Selected Topics in Quantum Electronics **8**, 823 (2002)
6. H. Morkoc, Nitride Semiconductors and Devices (Springer Verlag, Heidelberg), 1999
7. S. N. Mohammad, and H. Morkoc, Progress in Quantum Electronics **20**, 361, (1996)
8. F. Bernardini and V. Fiorentini, Physica Status Solidi B **216**, 391 (1999)
9. A. Hangleiter, J. S. Im, H. Kollmer, S. Heppel, J. Off, and F. Scholz, MRS Internet Journal of Nitride Semiconductor Research **3**, 15 (1998)
10. H. Amano, N. Sawaki, I. Akasaki, and Y. Toyoda, Applied Physics Letter **48**, 353 (1986)
11. S. Nakamura, Japan Journal of Applied Physics **30**, L1705 (1991)
12. S. Nakamura, T. Mukai, M, Senoh, S. Nagahama, and N. Iwasa, Journal of Applied Physics **74**, 3911 (1993)
13. H. Amano, N. Sawaki, I. Akasaki, and Y. Toyoda, Applied Physics Letter **48**, 353 (1986)
14. H. Amano, N. Sawaki, I. Akasaki, and Y. Toyoda, Japan Journal of Applied Physics **28**, L2112 (1989)
15. S. Nakamura, S. Iwasa, M. Senoh, US patent 5306662

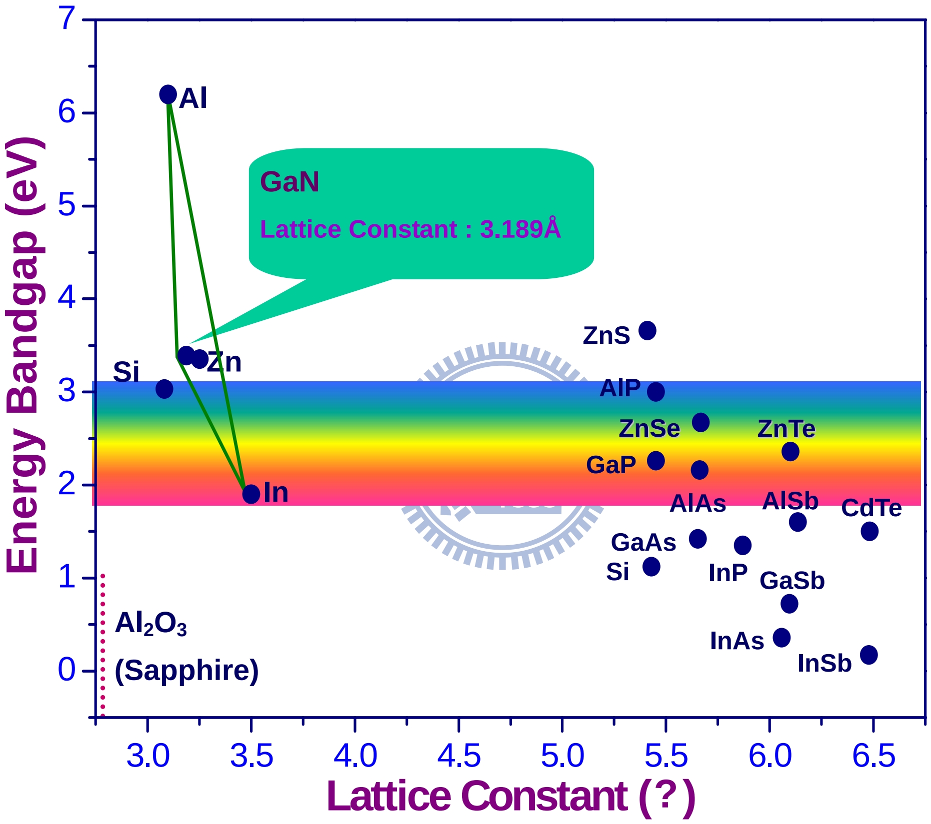

Figure 1.1 The bandgap diagram of compound semiconductor materials.

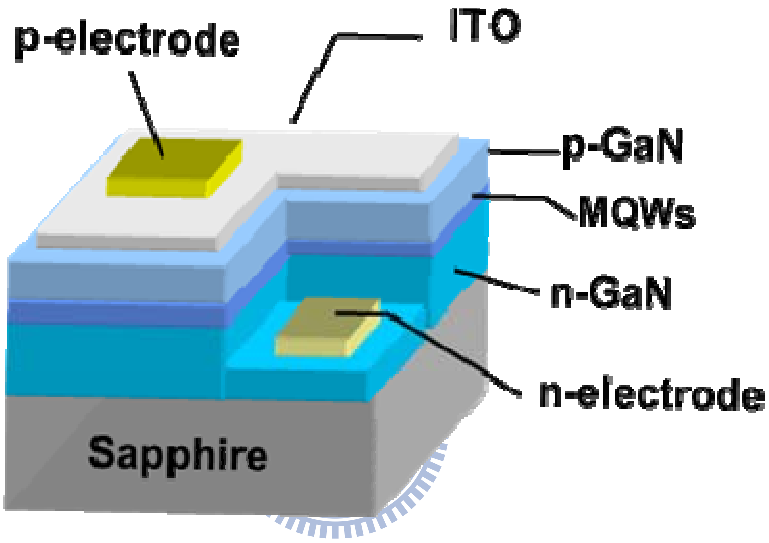

Figure 1.2 The schematic of typical p-side up GaN-based LED

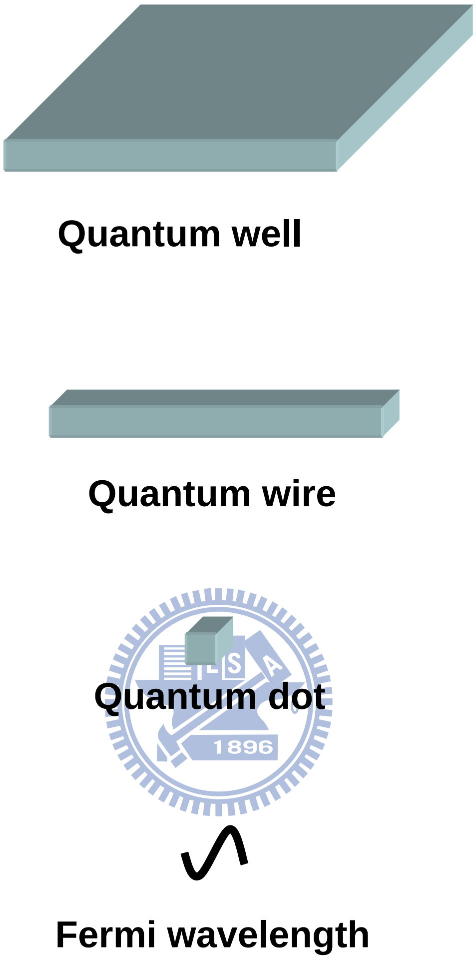

Figure 1.3 Schematic of quantum confined structures and Fermi wavelength

CHAPTER 2

Optical Properties and Strain Analysis of InGaN/GaN Nanorods

With the rapid development of nano-fabrication technology, fabrication and studies of nanorods in GaN-based semiconductors have attracted considerable interest for potential applications in electronic and optoelectronic devices due to the quantum confinement and the strain relaxation effect [1]. It is also reported that the InGaN/GaN nanorods can exhibit optical and electrical properties that are different from those in the bulk materials

GaN nanorods have been produced by various fabrication methods. In 1997, Han *et al.* first proposed synthesizing GaN nanorods by using carbon nanotubes as templates [2]. The dimension of the synthesized GaN nanorods could be up to 25 m in length and ranging from 4 to 50 m in diameter. However, preparing the carbon nanotube is rather complicated. The growth of single-crystal GaN nanorods by hybrid vapor-phase epitaxy [3] has been developed by Kim *et al.*A mask-free simple process by inductively coupled plasma-reactive ion etching (ICP-RIE) dry etching to fabricate GaN nanorods was proposed by Yu *et al.* [4]. The growth of GaN nanorods by using ferrocene as the catalyst, so-called vapor–liquid–solid (VLS) mechanism, was also demonstrated [5]. Fabrication of GaN nanorods by e-beam patterning and ICP etching was proposed by Chen *et al.* [6].

By the benefit of development of these nano-structure fabrication techniques, several GaN devices were then fabricated and the characteristics were studied. Johnson *et. al* demonstrated a single GaN nanowire lasing phenomenon in [7]. It is the first demonstration of single GaN nanowire laser. Han *et. al.* performed the photoconduction studies on GaN nanowire transistors under UV and polarized UV illumination in 2004 [8]. Besides, Kim *et. al.* demonstrated a high brightness LEDs by fabricating high quality, dislocation-free InGaN/GaN nanorods [9]. Finally, in 2006, Son *et. al.* demonstrated a UV photodetector by using a single GaN nanorod with p-n junction [10]. From these literatures, we could conclude that by the help of GaN nanostructure, we could obtain most of opto-electronic devices like laser, LED and photodetector from blue to UV region.

However, most of these GaN nano-structures are formed by epi-growth methods, which is not suitable for mass production in the present production. In addition, the typical structures prepared by these methods do not contain active layers, which limit the potential applications for optoelectronic devices. We developed a novel method to form GaN nanorod with InGaN/GaN multiple quantum wells (MQWs). The details of the nanostructure fabrication and characteristics will be introduced in this chapter.

2-1 Fabrication Process

Generally, this nanorod fabrication process could be applied on any type of semiconductor material like Si, GaAs, GaN or sapphire substrate. In this chapter, we selected to form nanorod on the surface of GaN-based LED. The samples we used in this chapter were grown by metal–organic chemical vapor deposition (MOCVD) with a rotating-disk reactor on a *c*-plane sapphire (0001) substrate at a growth pressure of 200 mbar. The epitaxial structure consisted of a 30-nm-thick GaN nucleation layer, a 2-μm-thick unintentionally doped GaN buffer layer, a 2-μm-thick Si-doped n-GaN layer, an unintentionally doped InGaN/GaN MQW active region, and a 0.2-μm-thick Mg-doped p-GaN. The MQW active region consists of ten pairs of 3- and 7-nm-thick InGaN wells and GaN barriers.

Based on our previous experimental results, a thin metal film can be self-assembled into nano-scaled islands after rapid temperature annealing (RTA), and the metal islands can result in better distribution uniformity with a dielectric film deposited underneath the metal layer. Therefore, the nanorod formation process was started from depositing a thin dielectric film on top of the GaN LED surface as shown in figure 2.1. A 100-nm-thick SiO_2 layer was first deposited on the epi-surface of LEDs by plasma-enhanced chemical vapor deposition (PECVD). Then, we deposited a thin metal, Ni in this thesis, on top of SiO_2 layer on the purpose to form etching masks. We selected Ni metal because it could be obtained easily by E-gun evaporator. Besides, it has better etching selectivity to general semiconductor material like GaAs and GaN than other metals which enable us to form high aspect ratio nano-structures. A thin Ni metal layer was then deposited on the surface of the SiO_2 layer (figure 2.1(a)).and subsequently undergone the RTA process to form the self-assembly nanometer sized Ni clusters (figure 2.1(b)). The sample with Ni nanomasks on the surface were subsequently performed reactive ion etching (RIE) to remove SiO_2 to transfer the nanoscaled pattern into the SiO_2 and ICP to form GaN nanorod structures (figure 2.1(d)). The samples were then etched by the ICP-RIE system (SAMCO ICP-RIE 101iPH) operated at 13.56 MHz under a gas mixture of Cl_2/Ar = 45/30 SCCM through individual electronic mass flow controllers. The ICP source power, bias power, and the chamber pressure of the ICP-RIE system were set to 400W, 100 W, and 0.66 Pa, respectively. After the etching process, we use heated nitric acid to remove residual Ni masks and buffered oxide etchant (BOE) to remove the SiO_2 on top of GaN nanorods (figure 2.1(e)). The details of each step will be introduced as followed.

Effect of dielectric layer

As mentioned in previous paragraph, more uniform nano-masks could be obtained if an underneath dielectric layer was deposited first. The difference between these two cases, annealing with and without underneath dielectric layer was shown in figure 2.2. Figure 2.2 is the scanning electron microscope (SEM) images. Figure 2.2(a) shows the annealing results on top of dielectric layer and (b) shows that on GaN surface. A discrete Ni nano-cluster array could be observed at the surface. In this figure, the diameter is ranging from about 90 to 140 nm. On the other side, the annealed Ni nano-clusters on bare LED surface show a non-uniform pattern in the diameters and behaved a sheet-like result instead of dot-like structure. This difference could be explained by the strain effect. The room temperature lattice constant of Ni was about 0.352 nm and that of the corresponding crystalline GaN surface to be 0.318 nm in *a* direction and 0.518 nm in *c* direction. This gives the room temperature strains were $\varepsilon_{a(GaN/Ni)}$= 10% and $\varepsilon_{c(GaN/Ni)}$=-32%. However, the dielectric SiO_2 has a lattice constant to be 0.49 nm in the *a* direction and 0.54 nm in the *c* direction gives the room temperature strains as $\varepsilon_{a(SiO2/Ni)}$= -28% and $\varepsilon_{c(Si3N4/Ni)}$ =-35% respectively. This means that the deposition of Ni on SiO_2 bears a higher tensile strain in both *a* and *c* directions which results in a smaller and more uniform nano-cluster array in the surface [11]. Besides, by depositing a dielectric underneath layer like SiO_2 or Si_3H_4, we could sustain the large strain between these two layers which means we could ignore possible strain variation resulted from substrate. That means we are able to form these kind of nano-structure at any material surface as long as there is no temperature issues.

Effect of Ni thickness

Regarding to the geometry and density of the formed Ni nano-clusters, we conclude two main factors, the Ni layer thickness and the RTA temperature. In order to find out the effect of different thickness, we varied the deposited Ni thickness from 50 to 200 Å on the surface of 100 nm SiO_2 layer on top of GaN-based LED. The RTA temperature and maintain time was fixed at 850 ^{o}C with a ramp of 40 ^{o}C/sec and 60 sec to form nano-clusters. The diameter and density of the formed nano-clusters were shown in figure 2.3. We could find that the average diameter was 120 ± 20, 180 ± 20, 220 ± 20, and 300 ± 30 nm while the deposited Ni thickness increasing from 50 to 200 Å. On the other side, the density decrease from 3 to 0.5 x 10^9 cm^{-2} with the increasing thickness. We could conclude that the diameter was proportional to the Ni thickness but the density has an opposite trend.

Effect of RTA temperature

Besides the Ni thickness, RTA temperature is another very important factor to determine the geometry of formed nano-clusters. In this case, we fixed the thickness of Ni layer and varying the RTA temperature from 800 to 900 ^{o}C with a constant ramping speed of 50 ^{o}C/sec lasting for 60 sec, and the results were shown in figure 2.4. As the RTA temperature increased from 800 to 900 ^{o}C, the diameter increased steadily from about 210 ± 20 to 300 ± 20 nm. Here we could find out a maximum in density at the RTA temperature of about 850 ^{o}C which implies a shortest spacing between each cluster at the surface. From observation of these two factors, it is easier for Ni to migrate and results in a smaller cluster size and higher distribution density. That also indicates that we could modify the diameter and density by well control the initial Ni thickness and RTA temperature.

2-2 Height-dependent Antireflection Properties

Recently, the interests in nano-scaled antireflection (AR) textures have been extended to disordered structures, where the fabrication cost is significantly reduced without the requirement of the electron beam lithography. Moreover, a variety of materials, including Si, GaAs, and glass [12], are available for the applications, offering versatile device possibilities. While several studies have been made on the reflectivity characterizations of disordered nanostructures [13-15], few reports have discussed the correlation between the reflective characteristics and the structural properties, such as geometric shapes, dimensions, and densities. Calculations on the reflectivities of nanostructures are also a challenge due to the nature of disorder, hindering further progress in device design and analysis. In this work, we have fabricated GaN nanorod structures with three different heights: 300, 550, and 720 nm. Since GaN is a wide bandgap material [16], the observed AR characteristics can be correlated with the structural properties. The fabrication process and AR characteristics of GaN nanorod with different height will be discussed and an algorithm based on a rigorous coupled-wave analysis (RCWA) method is also developed in this section.

Sample preparation

Based on previous GaN nanorod fabrication experience, in this section, we fabricated three different set of GaN nanorods with heights of h=300, 550 and 720 nm, corresponding to the etching times of 60, 90 and 120 sec, respectively. Figures 2.5(a) to (c) show the cross-sectional views of the fabricated samples. The respective etching rates were approximately 5, 6.11, and 6 nm/sec, indicating a slower etching rate at the beginning period due to the unapparent initial bombardment efficiency. However, the etching rate was decreased again at the etching time of 120 sec because, as shown in figure 2.5(b), the lateral etching of nanorod became noticeable, limiting the etch depth. A deeper nanopillar structure could be achieved if the flow rate of the etching gas (Cl_2) was reduced along with an increase in ICP power. It is found that the flow rate of Cl_2 and ICP power are critical in controlling the shape of nanorod.

Reflectivity measurement

The reflectivity of the n-GaN nanopillars was characterized as a function of the incident angle for both s- and p- polarizations, using a linearly polarized He-Ne laser at λ= 632.8 nm. The incident power was set to 3 mW with a spot size of ~1mm. As shown in the inset of figure 2.6, light struck on the sample at an incident angle θ_i, with respect to the surface normal, while the detector on the other side received the reflected light at the same angle, $\theta_o=\theta_i$. Both angles were varied from 20° to 80°. The system was calibrated with a silicon substrate before measurements. For reflectivity spectroscopy, the incident light was obtained from a monochromator using a xenon lamp with wavelengths ranging from 300 to 1800 nm.

The measured angle-dependent reflectivities for GaN nanorods of different heights are shown in figure 2.6(a) for s-polarization and (b) for p-polarization. The calculated reflectivities of bulk GaN (n=2.5) for both polarizations are also plotted for reference. As shown in figure 2.6, the angular reflectivities in GaN nanorod structures have been drastically reduced from those of bulk. As shown in figure 2.6(a), the reflectivities of s-polarization for h=550 and 720nm are nearly identical, showing excellent AR characteristics (<3%) up to an incident angle of 50^o. The reflectivities for h=330nm are relatively high and the interference from air/GaN and GaN/sapphire interfaces can also be observed. The interference characteristics completely vanish for h=550 and 720 nm, since the scattering on the nanorod surfaces give rise to phase randomization. As shown in figure 2.6(b), the measured reflectivities for three different heights are lower than 3% up to an incident angle of 60° for p-polarization. It is worth noting that the reflectivities of nanorod decrease as the incident angle increases before Brewster's angle, similar to those of bulk. Although Brewster's angle becomes indiscernible in nanorod structures, minimal reflectivities occur at incident angles of 53.5^o, 48.8^o, and 46.4^o for h=300, 550, and 720 nm, respectively, showing a linear correlation between the pillar height and the incident angle of the minimal reflectivity. This characteristic can also be observed in the reflectivity ratio of polarizations, that is, the ratio of the reflectivity of the s-polarization to that of the p-polarization, denoted as I_s/I_p. As shown in Fig. 3, the bulk GaN exhibits a peak of $I_s/I_p > 10^4$ at Brewster's angle of 63.5^o, while I_s/I_p drops significantly to <20 for all nanorod structures. As the height of the nanorod increases, the peak of I_s/I_p shifts towards a smaller incident angle. Figure 2.7 suggests that the reflectivities become polarization-insensitive even in a shallow nanostructured surface. It is also worth noting that the ratio I_s/I_p is enhanced at small incident angles, since the spatial symmetry of bulk at the normal incidence is altered by the nanostructures. Similar results have been observed in GaN nano-wires on sapphire with different coverage ratios [17].

The reflectivity spectroscopy with light incident at an angle of 32^o is shown in figure 2.8. Bulk GaN exhibits reflectivities of ~23% for s-polarization and ~13% for p-polarization in the wavelength range between 300 nm and 1800 nm, while the GaN nanopillars of h=720 nm show reflectivities <5% in the 300-1200 nm wavelength range, and <10% in λ=1200-1800 nm for both polarizations.

Reflectivity simulation

The measured data for GaN nanorods with a height of 720nm shows superior angular and spectral antireflection. However, the reflective characteristics of nanorods of different heights do not show significant differentiation that could determine the best fabrication parameters. Although the random variation of pillar widths and positions can not be accurately controlled, it is of great interest to understand the structural properties, such as the density, geometric shapes, and dimensions that contribute to superior AR characteristics. A thorough theoretical study can facilitate the design and fabrication of nano-structured AR surfaces. Therefore, a theoretical model based on a RCWA method is developed to investigate the dependence of the AR characteristics on the structural properties of nanorods.

The RCWA method is often employed to solve the diffraction and transmission efficiency of optical diffractive elements, where the reflectivity is obtained as a sum of the reflected diffraction efficiencies of different diffraction orders. In order to minimize the calculation errors arising from periodic boundary conditions in disordered structures, a unit-cell is defined with dimensions at least an order of magnitude larger than the incident wavelength. The size of unit cell and randomness of nanorod positions have also been studied to ensure convergence. Calculations show that a refractive-index gradient between air (n=1) and bulk GaN (n=2.5) is the key element to significantly reduce the reflection, since the incident light can hardly experience the changes in dielectric environments. Therefore, the shape of nanorods, which determines the refractive-index gradient, is desired to be a cone-like structure. The periodic SWS with shapes of pyramids are nearly ideal AR structures, since the nano-pyramids provide a linear gradient of the refractive indices between air and the silicon substrate [18]. In order to apply the design concept to disordered structures, we can define the fill factor as the ratio between the areas covered by nanorod with respect to a unit cell. It is desirable that the fill factor at the base of the nanorods approaches one while that at the top approaches zero.

We first investigate the origins of the omnidirectional antireflection by fitting the measured data. Since both the density and the base/top diameters of the nanorods determine the fill factors, the random variation in the pillar width is neglected for simulation. Moreover, a linear refractive-index gradient is assumed. Figure 2.9(a) shows the refractive-index profile of a unit cell, which consists of 7x7 random nanorod s with a height of 720nm. The unit cell has an area of ~1.6 μm^2, corresponding to a density of ~$3\times10^9 cm^{-2}$. The top/bottom diameters of the pillars with h=300nm, 550nm, and 720nm are chosen to be 140/170, 100/180, and 80/190 nm, respectively. The calculated reflectivities of random nanorod s are plotted as a function of the incident angle in figure 2.9(a) for (b) h=300nm, (c) h=550nm, and (d) h=720nm. Since the latter two share a similar refractive index gradient and fill factors in simulation, we attribute the omnidirectional antireflection to the tapered refractive-index profile due to the slight lateral etching of the nanopillars, as seen in figure 2.5(c) for h=550nm and figure 2.5(d) for h=720nm. On the other hand, the AR properties for h=300nm are limited by the etch depth and the pillar profile.

2-3 Size-dependent Optical Characteristics and Strain Relaxation Analysis

In GaN material system, there inherently exists large internal strain in GaN material and the MQWs and QCSE effect leading to the wave-function separation in electrons and holes. Since it has been known that fabricating nano-structures could modify and reduce the existing strain, it is of great interest to investigate the degree of strain relaxation by different GaN nanorod sizes. In this section, we fabricated four different sizes of GaN nanorods by depositing different thickness of Ni layer ranging from 50, 100, 150 to 200 Å. With fixed RTA temperature of 850 °C and RIE and ICP etching process to define SiO_2 and transfer it into GaN layer, we could get different diameter and density of nanorod arrays. From observation of SEM images from these fours samples with different initial Ni thickness as shown in figure 2.10, we could find the diameter of formed nanorods were 120 ± 20, 180 ± 20, 220 ± 20, and 300 ± 30 nm and the density decreased as thicker Ni thickness.

Optical properties

Figure 2.10 (a) and (b) shows the measured PL from a regular LED and nanorod LEDs with various average diameters at low temperature 20K and room temperature, respectively. The pumping powers for all measurements are 15 mW at a laser spot size of 200 μm. As shown in figure 2.10(a), as the averaged rod diameter becomes smaller, the emission peak shows a clear blue shift. The PL intensity is strongest for LEDs with the smallest averaged diameter, 120 nm. The intensity decreases as the diameter becomes larger. However, the PL characteristics at room temperature are slightly different from those at the low temperature 20 K. First, the emission peak still has a clear blue shift as the diameter becomes smaller. Second, the PL intensity is strongest for LEDs with an averaged diameter of 220 nm. PL intensities are deteriorated at room temperature for nanorod LEDs of 120 and 180 nm. The PL intensity of the regular LED is much weaker than nanorod LEDs due to a stronger QCSE and lower light extraction efficiency. Figure 2.11 shows the peak energy shift versus the rod diameters. The PL peak position of the regular LED is also plotted as the reference point. We can find that the fitted slopes at room temperature and 20 K are around 17.047 and 16.323 eV·nm, respectively.

The changes in PL intensity could be due to the absorption of excitation, the emission volume, light extraction efficiency, and defect densities of the nanorod LEDs. Therefore, it is hard to quantitatively analyze the size-dependent characteristics of the PL intensity and we will discuss qualitatively later. On the other hand, the blue shift of the spectrum is large (>100 meV) and cannot be simply explained by the band-filling effect or the carrier screening of QCSE. In particular, the power density of PL is not strong enough to induce a very high carrier density in the MQWs. The other possibility is the strain relaxation of the QW [18]. For InGaN/GaN, QW structures grown along *c*-axis, there exists a strong strain-induced piezoelectric polarization field inside the device. This will contribute to the band bending and red shift of spectrum, known as the QCSE. For the QW structure at the edge of nanorod surface, the lateral confinement of the QW is weak such that the relaxation of the InGaN QW layer is possible. The relaxed strain reduces the piezoelectric field inside theQWso that the spectrum shows a blue shift of the emission wavelength. This blue shift should be observed for low power, high-power, low-temperature, and room-temperature PL measurements.

As mentioned earlier, the PL intensity of the nanorod with the smallest diameters is the strongest at low temperature. However, at room temperature, the PL intensity maximum occurs for nanorod LEDs with an average diameter of 220 nm. The effects of extraction and absorption may be neglected since they were measured from the same samples only at different temperatures. It is possible that the defect density contributes to the decease of the PL intensity. Therefore, we conduct the time-resolved photoluminescence (TRPL) for both cases. Figure 2.13(a) and (b) shows the measured TRPL at low temperature 20 K and room temperature, respectively. As shown in figure 2.13(a), the fitted decay times are 25.34, 18.13, 13.49, and 7.39 ns for nanorod diameters of 300, 220, 180, and 120 nm, respectively. The nanorod LEDs with the diameter of 120 nm have the smallest decay time. If the carrier decaying process is dominated by radiative recombination, the smallest diameter nanorod has the best efficiency. This can be also observed with the PL spectrum intensity, as shown in Figure 2.11(a). However, at room temperature, we can find that the nanorod LEDs with the diameter of 220 nm have the strongest emission intensity. However, as shown in figure 2.13(b), the TRPL shows that the decay time of 120 nm nanorod has the smallest decay time. It is well-known that the PL decay lifetime is determined by both the radiative and nonradiative processes. If the radiative lifetime dominates, the emission intensity should be strongest for the smallest nanorod size due to the smallest decay time. However, the intensity of nanorod LEDs with a diameter of 120 nm exhibits an opposing behavior, as shown in figure 2.11(b). Hence, we conclude that the nonradiative decay process dominates and reduces the emission intensities at room temperature. The nanorod LEDs with a diameter size smaller than 180 nm may have a large defect density. Although the nanorod LEDs with a small averaged diameter can increase the radiative recombination rate, the increased nonradiative recombination rate cancels the effect of radiative rate enhancement and limits the internal quantum efficiency.

VFF simulation

In order to confirm the observed wavelength blue shift, we first apply the valence force field (VFF) model [19]. Once the atoms' positions are known, calculating the strain tensor distribution is straightforward. To maintain the symmetry in a wurtzite structure, free-standing, cylindrical-shaped GaN nanorods consisting of ten-pair $In_{0.2}Ga_{0.8}N$ MQWs are defined with various diameters ranging from 120 to 300 nm. The nanorod has a fixed boundary condition at the bottom and free boundary conditions on other sides. Figure 2.14 shows the calculated strain distribution for the nanorod with a diameter equal to 120 nm. Figure 2.14(a)–(c) shows the strain tensor ε_{xx}, ε_{yy}, and ε_{zz} of the cross section of $x - z$ plane at the center of y-axis, respectively. Figure 2.14(d) shows the line plot at $r = 58$ nm and $r = 0$ nm (center) of strain tensor. Both strain tensors show considerable relaxations on the outer shell of the nanorod, and as-grown-like strain distributions in the center of the nanorod. As shown in figure 2.14(a), the strain relaxation of εxx occurs at a distance of 20 nm from the edge of the nanorod. At r = 58 nm, where the change of strain from the nanorod center is most significant, there exist substantial strain variations on the QW/barrier interfaces and a slight tensile strain of εxx in the barriers. There is also a slight strain relaxation of *_yy* due to the circular shape of the rod. We also observe a vertical distribution of εzz in the *Z*-direction, mainly arising from the stacking of MQWs.

Figure 2.15(a)–(d) shows the strain tensors ε_{xx} for nanorod diameters equal to 120, 180, 220, and 300 nm, respectively. As shown in figure 2.15, the major strain relaxation region is limited to 20 nm from the edge, regardless of the rod diameters. Therefore, the ratio of strain-relaxed MQW region to the strained region size becomes larger as the diameter decreases. With the calculated strain information, it is possible to calculate the emission spectra of nanorod LEDs with different sizes. Both in-plane and vertical strain tensors contribute to the polarization field and can be calculated by the following equation:

$$P_{ez} = e_{31}(\varepsilon_{xx}+\varepsilon_{yy})+e_{33}\varepsilon_{zz} \tag{2-1}$$

where $e31$ and $e33$ are the piezoelectric coefficients and can be found in Ambacher *et al.* [20]. Based on the calculated strain, as shown in figure 2.14, and the induced polarization harge calculated by

$$\rho_{pz}(x,y,z) = \frac{P_{ez}(x,y,z+dz)-P_{ez}(x,y,z)}{dz} \tag{2-2}$$

The calculated results are subsequently inserted into the self-consistent Poisson, Schr¨odinger, and drift-diffusion solver to calculate the band structure of the MQWs. The parameters needed for the band structure calculation can be found in Ambacher *et al.* [20].

Figure 2.16 shows the calculated band structures of the ten-pair MQW structure for different strain conditions: (a) at the center and (b) at the edge of the nanorod with a diameter of 120 nm. The polarization charge density induced by strain is taken into account as a function of the depth and the spontaneous polarization. As shown in Fig. 7, the band bending at the center of the nanorod is the strongest while the band bending at the edge is the weakest at r = 58 nm, where the strain relaxation reaches the maximum. In order to compare the PL intensity and compare the energy shift of the emission peak at different regions, we use the following equation to calculate the emission intensity and the energy shift.

$$R_{spon} = \int d(\hbar\omega)\frac{e^2 n_r \hbar\omega}{m_0{}^2 \varepsilon_0 c^3 \hbar^2}\sum_{i,j}\int \frac{2}{(2\pi)^2} d\mathrm{k}\left|a \bullet \mathrm{p}_{i,j}\right|^2 \times \frac{1}{\sqrt{2\pi}\sigma}\exp\left(\frac{-(E_{i,j}-\hbar\omega)^2}{2\sigma^2}\right) f^e f^h \tag{2-3}$$

where $E_{i,j}$ is the averaged energy separation between the electron state i and hole state j, n_r is the refractive index, and σ is the inhomogeneous broadening factor. $f^e(\mathrm{k})$ and $f^h(\mathrm{k})$ are the Fermi–Dirac distribution of electrons and holes, respectively. $|a \cdot \mathrm{p}_{i,j}\ |2$ is the momentum matrix element between the electron state, i, and the hole state, j. The calculated results are shown in figure 2.17. Figure 2.17(a) shows the calculated emission spectra of the MQW structure at different regions of the nanorod structure with a diameter of 120 nm and under an injected electron density of 8×10^{11} cm^{-2} ($n_{3\mathrm{d}} \sim 2.7 \times 10^{18}$ cm^{-3}). The average hole density is around 7×10^{12} cm^{-2}, which is much higher than electron density due to the heavier effective mass and smaller diffusion length so that more holes stay inside the QW after electron–hole pairs are generated. As shown in figure 2.17 (a), the emission intensity near the edge is the strongest. For r<45 nm, the emission strength does not change much, and this can be explained by the insignificant strain variation from the center, as shown in figure 2.14. Moreover, figure 2.17(b) shows the calculated emission peak shift and emission rates as a function of the radius of the cylindrical nanorod under an injected electron density of 8×10^{11} cm^{-2}. The maximum emission peak shift occurs at r=58 nm where 200 meV blue shift is achieved, compared to the emission from center of the nanorod. At r=60 nm, the strain relaxation is not the maximum at the surface so that the energy shift maximum does not occur here. The emission rate reaches the maximum at edge and decreases rapidly from r=60 nm to r=45 nm. The emission rates are almost constants for r<45 nm, where the electron–hole wavefunction overlap does not change too much here. Since the center of MQWs are still suffered from the strain with its magnitude comparable to that of the as-grown planar structure, the PL from the center of the nanorod contributes to the red-edge emission, which is partially overlapped with the PL from the strained region. Therefore, we believe that the majority of the nanorod PL blue shift originates from the strain relaxed region, within a distance of ~15 nm near the edge of the nanorod, as shown in figure 2.17(b). Moreover, the variation of strain tensors in the relaxation region results in a spatially varied polarization field, leading to a broadened emission spectrum.

Reference:

1 C. H. Chiu, M. H. Lo, T. C. Lu, P. Yu, H. W. Huang, H. C. Kuo, and S. C. Wang, IEEE Journal of Lightwave Technology **26**, 1445 (2008).

2 W. Q. Han, S. S. Fan, Q. Q. Li, and Y. D. Hu, Science **277**, 1287 (1997).

3 H. M. Kim, D. S. Kim, T. W. Kang, Y. H. Cho, and K. S. Chung, Applied Physics Letter **81** 2193, (2002).

4 C. C. Yu, C. F. Chu, J. Y. Tsai, H. W. Huang, T. H. Hsueh, C. F. Lin, and S. C. Wang, Japan Journal of Applied Physics **41**, L910 (2002).

5 W. Q. Han and A. Zettl, Applied Physics Letter **80**, 303 (2002).

6 H. S. Chen, D. M. Yeh, Y. C. Lu, C. Y. Chen, C. F. Huang, T. Y. Tang, C. C. Yang, C. S.Wu, and C. D. Chen, Nanotechnology **17**, 1454 (2006).

7 J. C. Johnson, H. J. Choi, K. P. Knutsen, R. D. Schaller, P. D. Yang, and R. J. Saykally, Nature Material **1** 106 (2002).

8 S. Han, W. Jin, D. H. Zhang, T. Tang, C. Li, X. L. Liu, Z. Q. Liu, B. Lei, and C. W. Zhou, Chemical Physics Letter **389**, 176 (2004).

9 H. M. Kim, Y. H. Cho, H. Lee, S. I. Kim, S. R. Ryu, D. Y. Kim, T.W. Kang, andK. S. Chung, Nano Letter **4** 1059 (2004).

10 M. S. Son, S. I. Im, Y. S. Park, C. M. Park, T.W. Kang, and K. H. Yoo, Material Science and Engineering C-Biomimetic and Supramolecular System **26**, 886 (2006).

11 J. D. Carey, L. L. Ong and S. R. P. Silva, Nanotechnology **14**, 1223 (2003).

12 D. S. Hobbs, B. D. MacLeod, and J. R. Riccobono, Proc. of SPIE **6545** 65450Y-1-14, (2007)

13 G. R. Lin, Y. C. Chang, E. S. Liu, H. C. Kuo, and H. S. Lin, Applied Physics Letter **90**, 181923 (2007).

14 Y. Kanamori, K.-I. Kobayashi, H. Yugami, K. Hane, Japan Journal of Applied Physics **42**, 4020 (2003)

15 Y. Zhao, J. Wang and G. Mao, Optics Letter **30**, 1885 (2005)

16 S. Nakamura, M. Senoh, S. Nagahama, N. Iwasa, T. Yamada , T. Matsushita, H. Kiyoku, and Y. Sugimoto, Japan Journal of Applied Physics **35**, L74 (1996).

17 Y. Du. S. Han, W. Jin, C. Zhou, and A. F. J. Levi, Applied Physics Letter **83**, 996-998 (2003)

18 P. Yu, C. H. Chiu, Y.-R.Wu, H. H.Yen, J. R. Chen, C. C. Kao, H.-W. Yang, H. C. Kuo, T. C. Lu, W. Y. Yeh, and S. C. Wang, Applied Physics Letter **93**, 081110 (2008).

19 Y.-R. Wu, M. Singh, and J. Singh, Journal of Applied. Physics **94**, 5826 (2003).

20 O. Ambacher, J. Majewski, C. Miskys, A. Link, M. Hermann, M. Eickhoff, M. Stuzmann, F. Bernardini,V. Fiorentini,V. Tilak,B. Schaff, and L. F. Eastman, Condens. Material **14**, 3399 (2002).

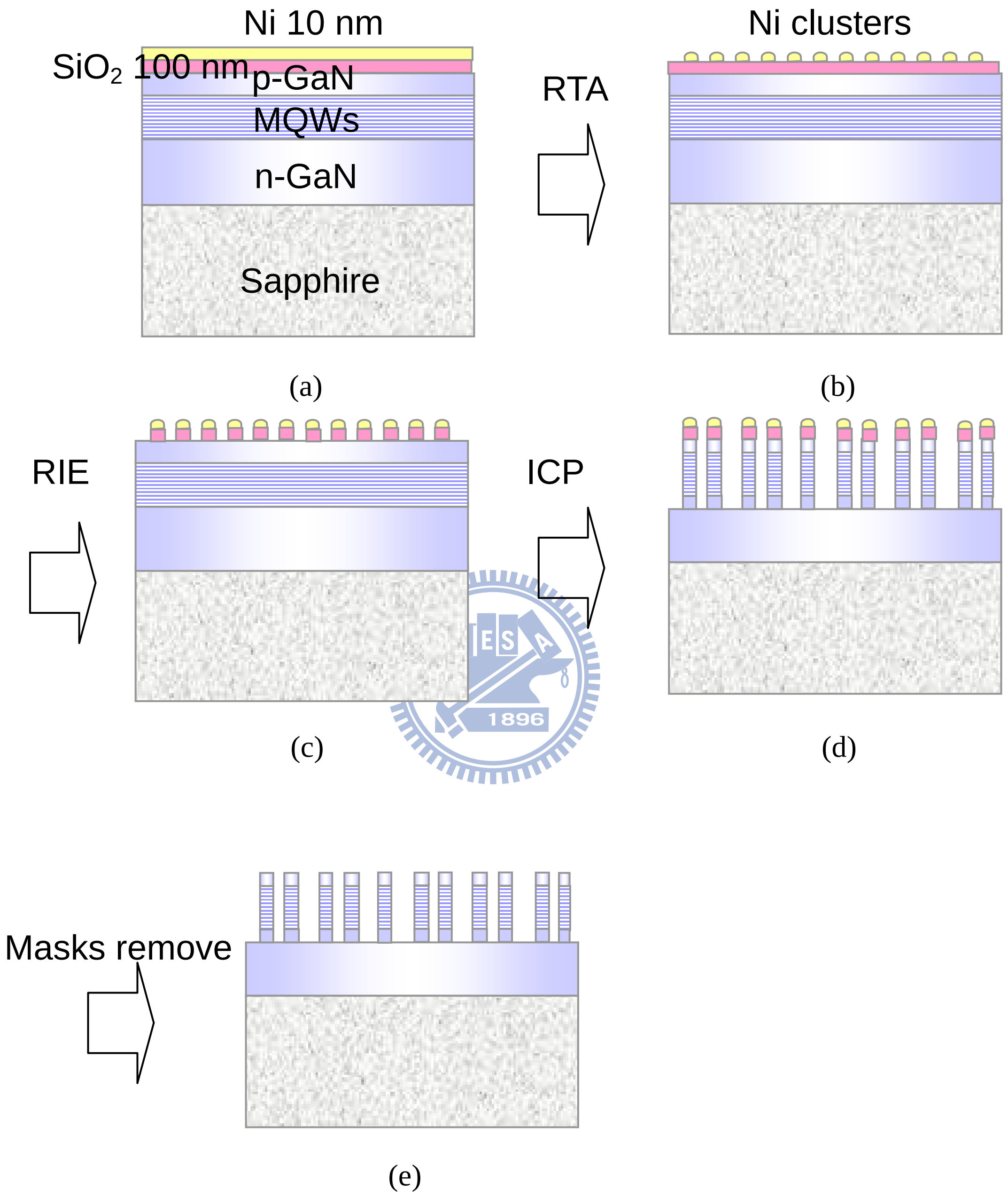

Figure 2.1 Schematic of GaN nanorod fabrication process

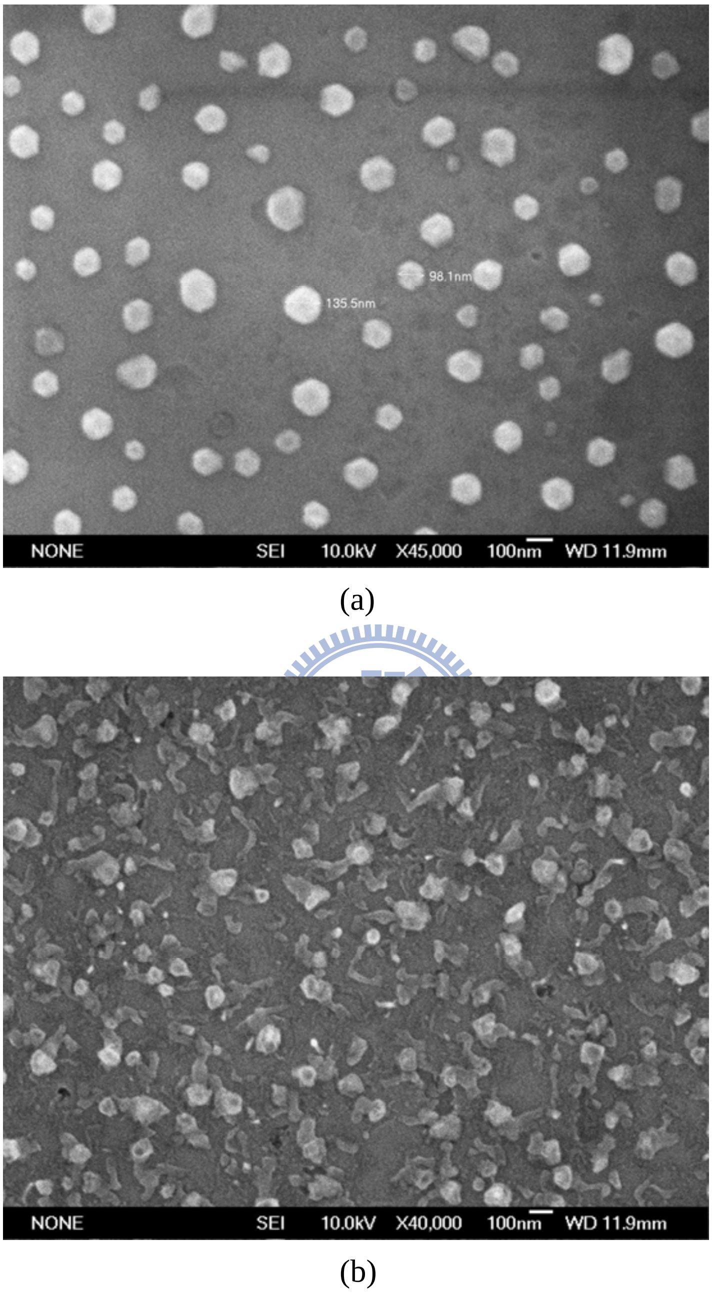

(a)

(b)

Figure 2.2 SEM images of nano-clusters formed on the surface of (a) SiO_2 layer and (b) GaN material.

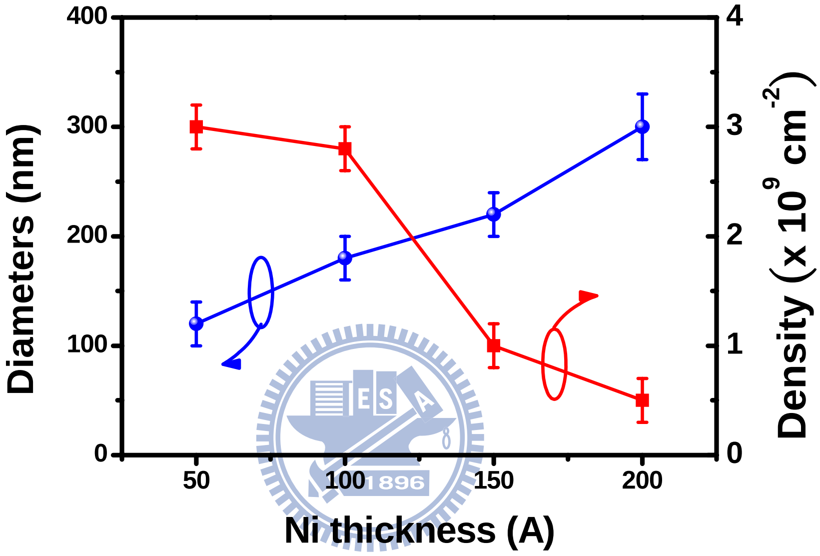

Figure 2.3 The relationship of diameters and densities of the formed Ni nano-clusters versus the Ni thickness.

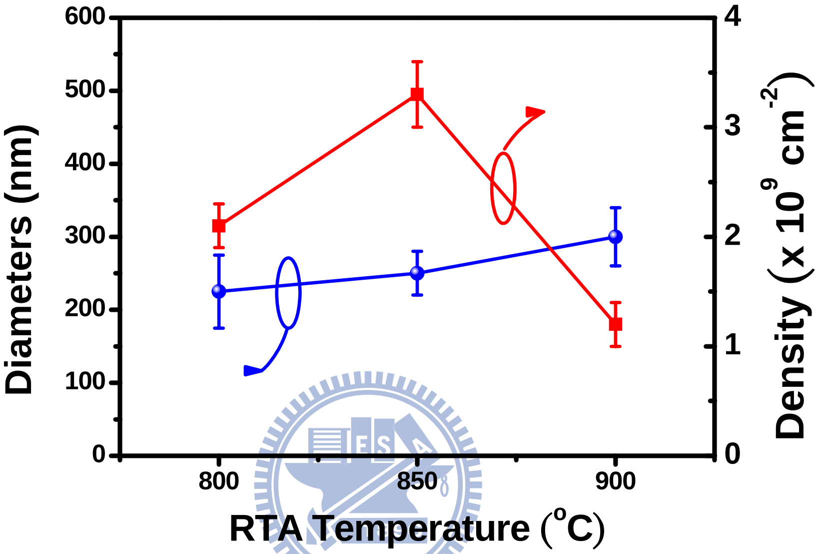

Figure 2.4 The relationship of diameters and densities of the formed Ni nano-clusters versus the RTA temperature.

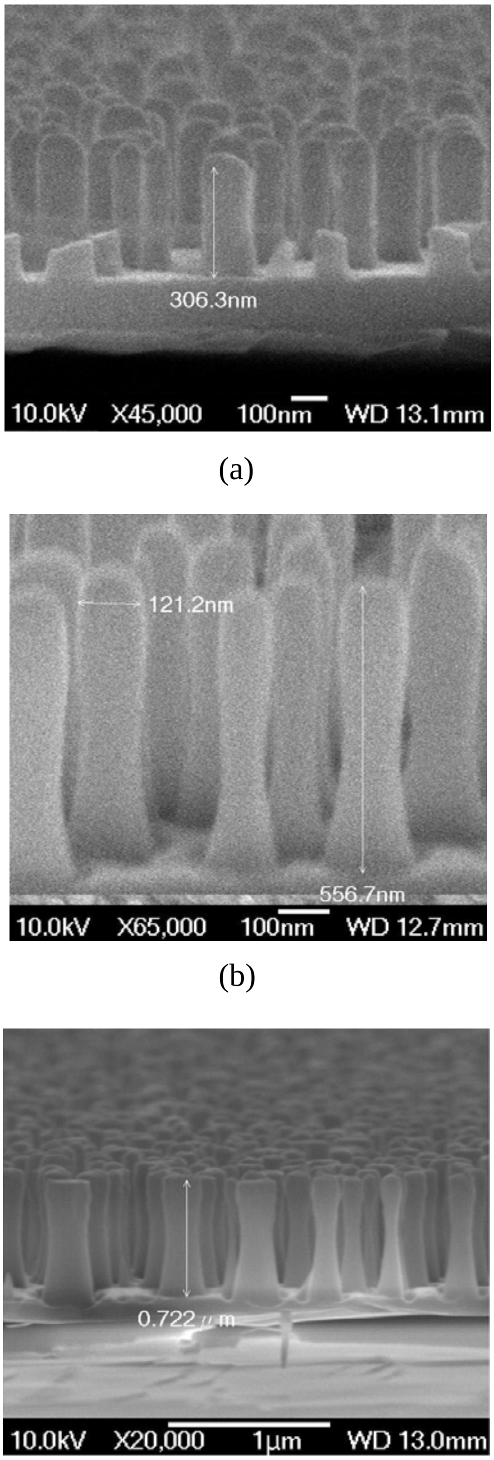

(a)

(b)

(c)

Figure 2.5 Cross-sectional views of the FESEM graphs for fabricated nanorod structures with heights of (a) 300 nm, (b) 550 nm, and (c) 720 nm.

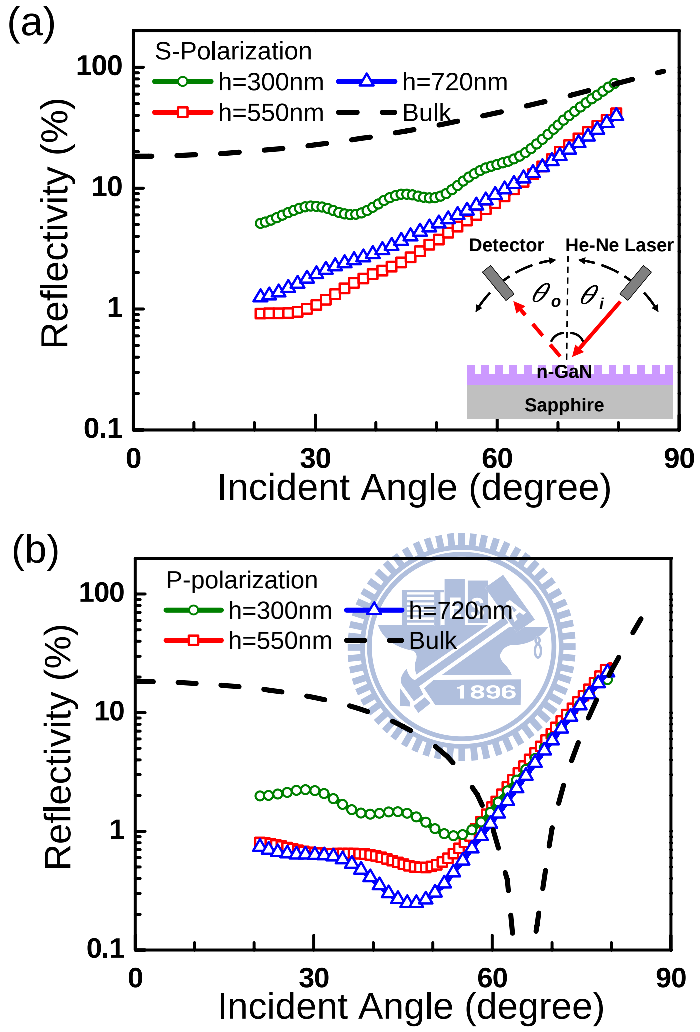

Figure 2.6 Measured reflectivities of GaN nanorods with three different heights: h=350nm, 550nm, and 720nm, for (a) s-polarization and (b) p-polarization. The inset shows a schematic of the measurement setup.

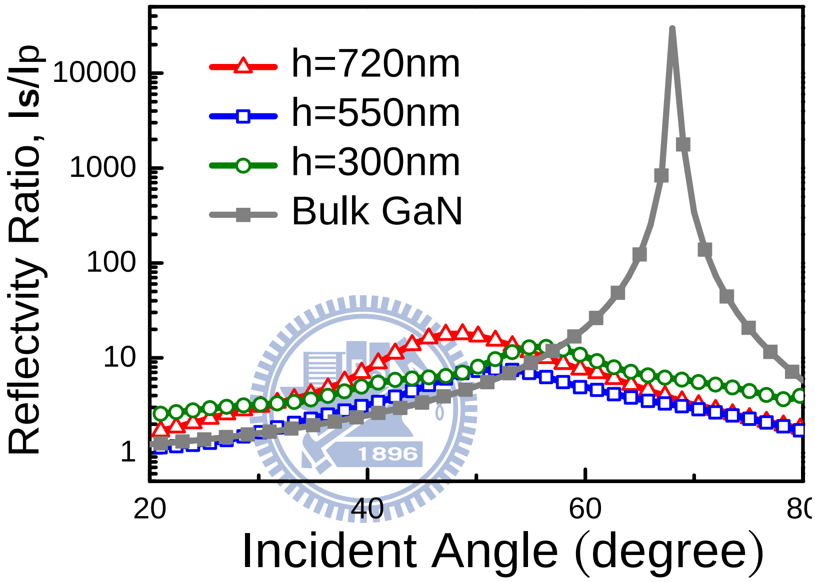

Figure 2.7 The reflectivity ratio of polarizations, I_s/I_p for bulk GaN, and nanorods of h=300, 550, and 720 nm is plotted as a function the incident angle. The reflectivities of nanorod structures are polarization-insensitive compared to those of bulk.

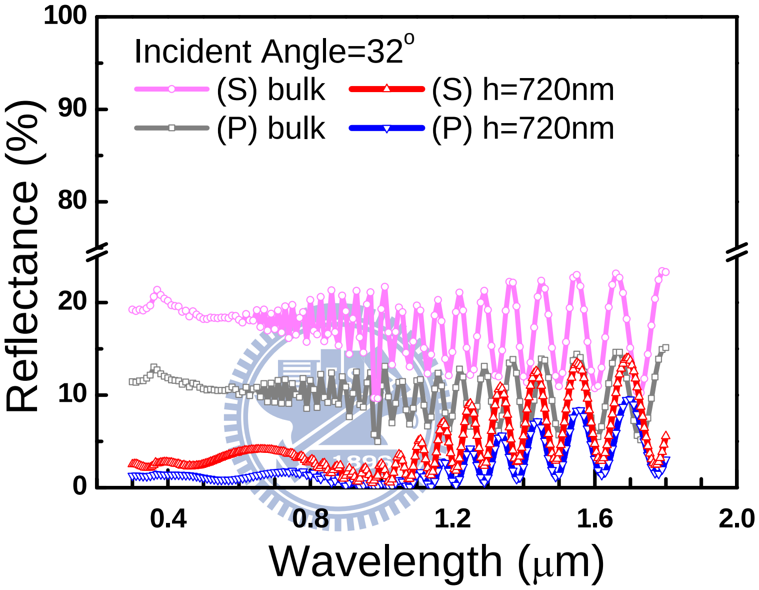

Figure 2.8 The reflectivity spectroscopy for bulk GaN and the nanopillars with a height of 720 nm at an incident angle of 32^{o}.

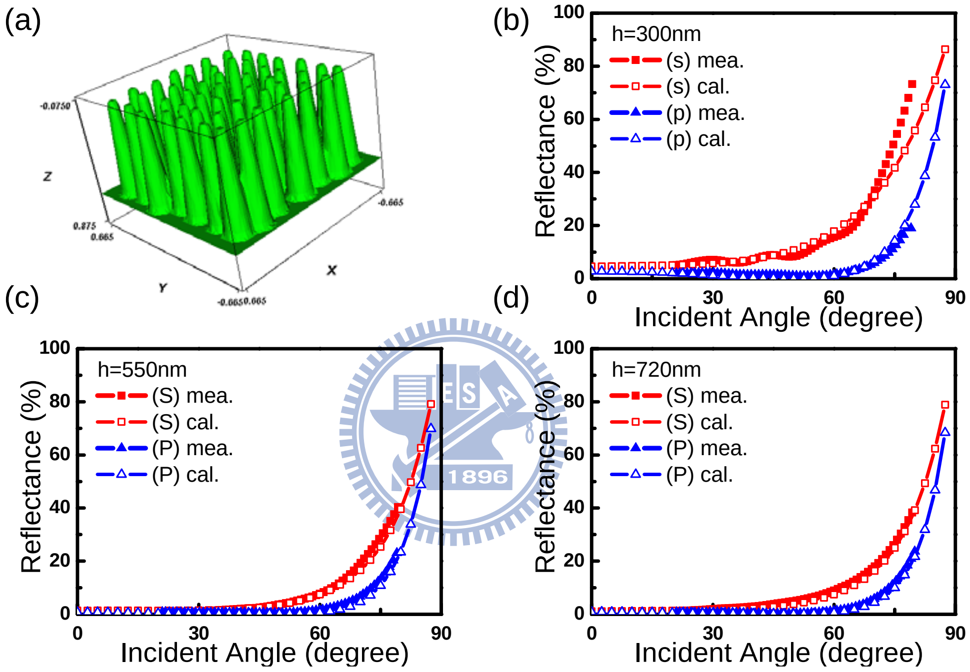

Figure 2.9 (a) The index profile consists of 7x7 random nanorodrs with a height of 720 nm. Calculated reflectivities of GaN nanorods are plotted as a function of the incident angle for three different heights: (b) h=300 nm, (c) h=550 nm, and (d) h=720 nm, for both s- and p-polarizations.

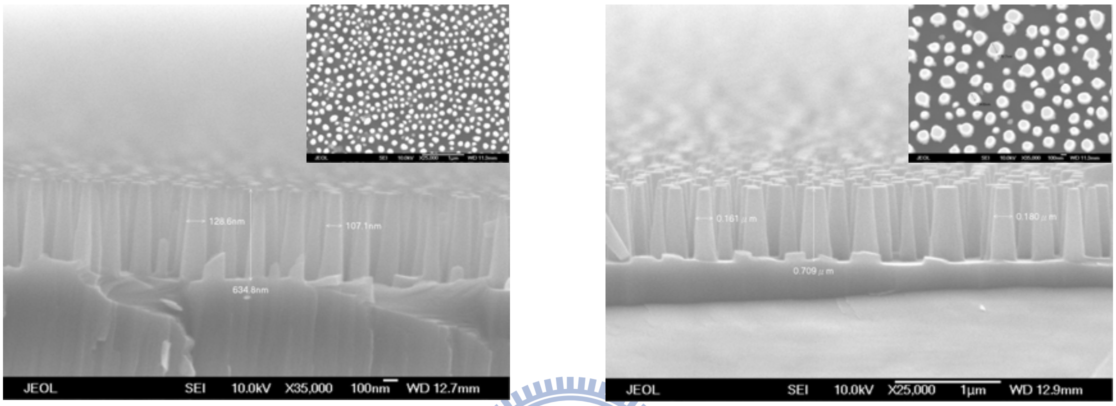

Ni 50A, Ave. Dia. 100nm

Ni 100A, Ave. Dia. 180nm

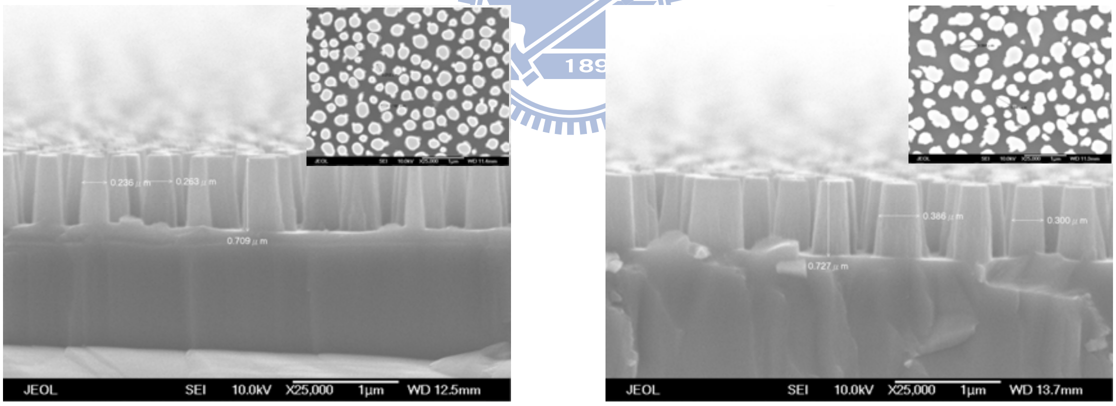

Ni 150A, Ave. Dia. 220nm

Ni 200A, Ave. Dia. 300nm

Figure 2.10 SEM images of GaN nanorods with diameter of (a)120 ± 20, (b)180 ± 20, (c)220 ± 20, and (d)300 ± 30 nm.

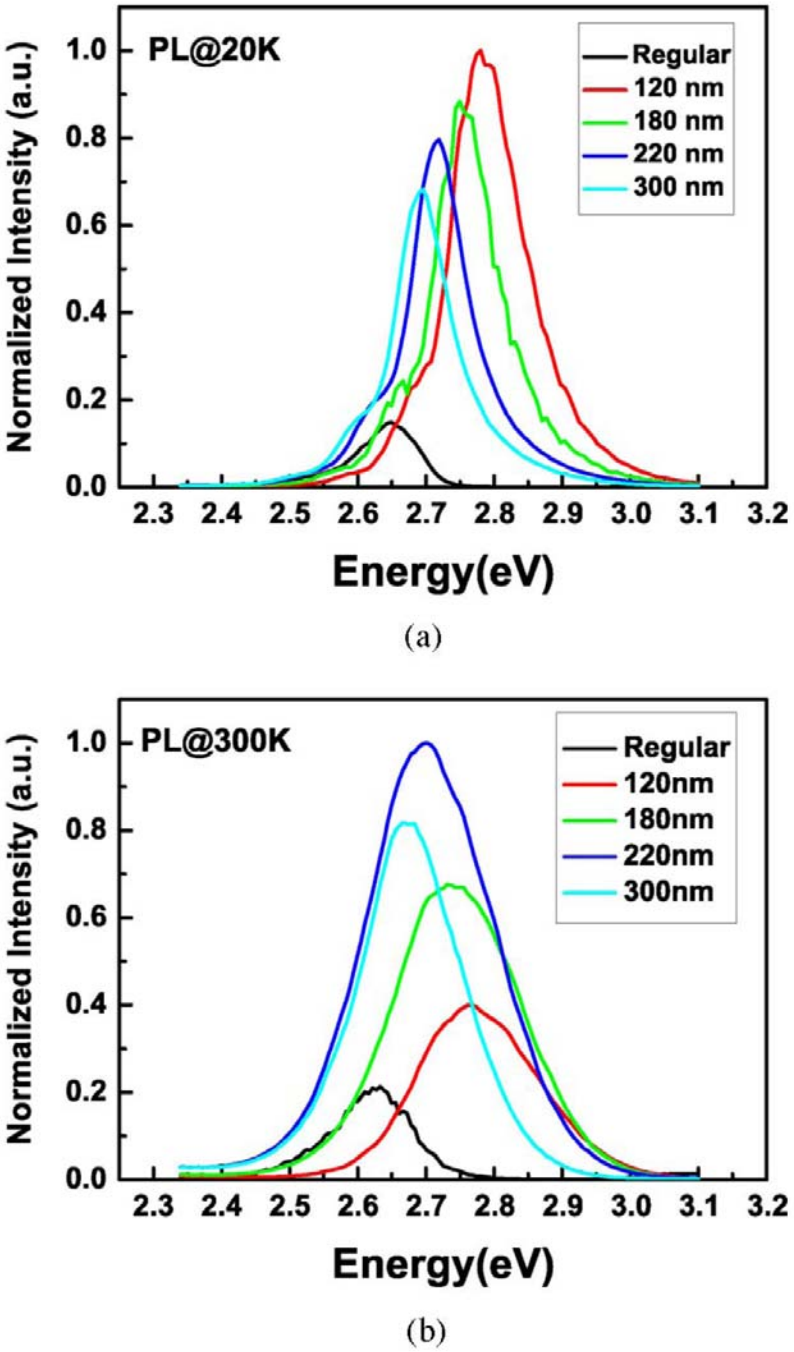

(a)

(b)

Figure 2.11 PL spectra of a bulk material and nanorod arrays with different sizes at (a) 20 K and (b) room temperature.

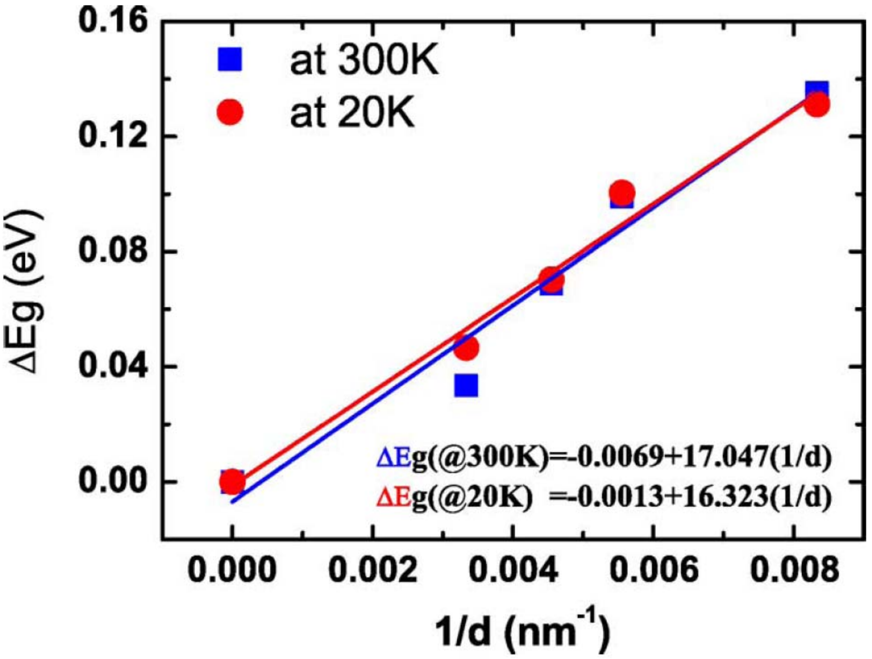

Figure 2.12 Measured peak shift and fitted curve versus nanorod diameters at room temperature and at 20 K.

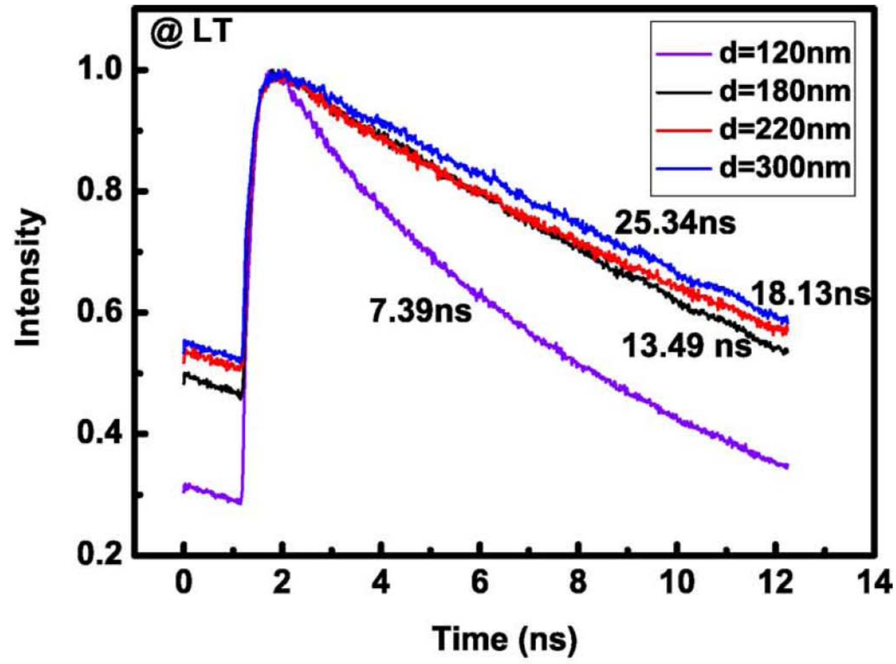

(a)

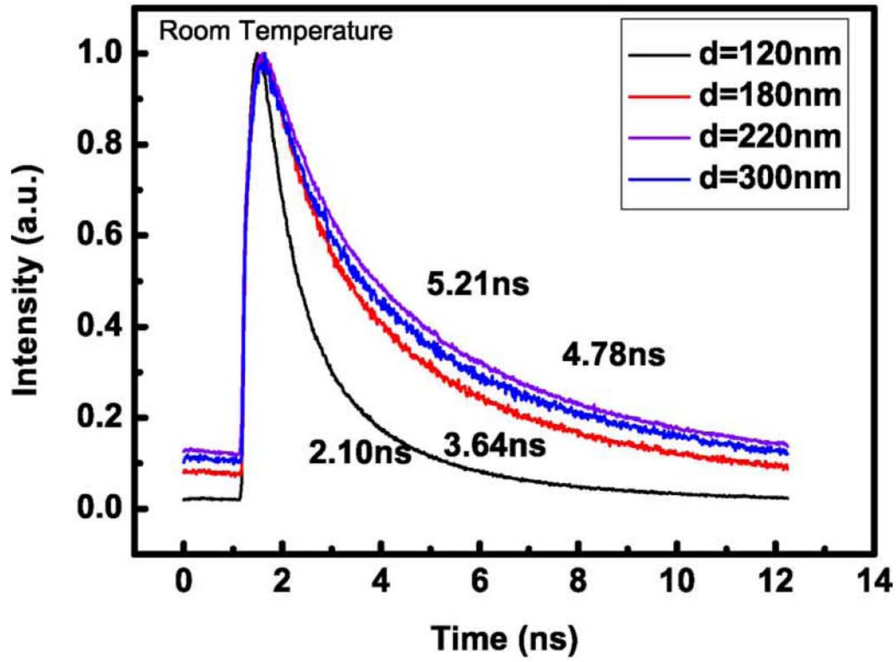

(b)

Figure 2.13 (a) TRPL for GaN nanorods with different sizes at 20 K. (b) TRPL for GaN nanorod with different sizes at room temperature.

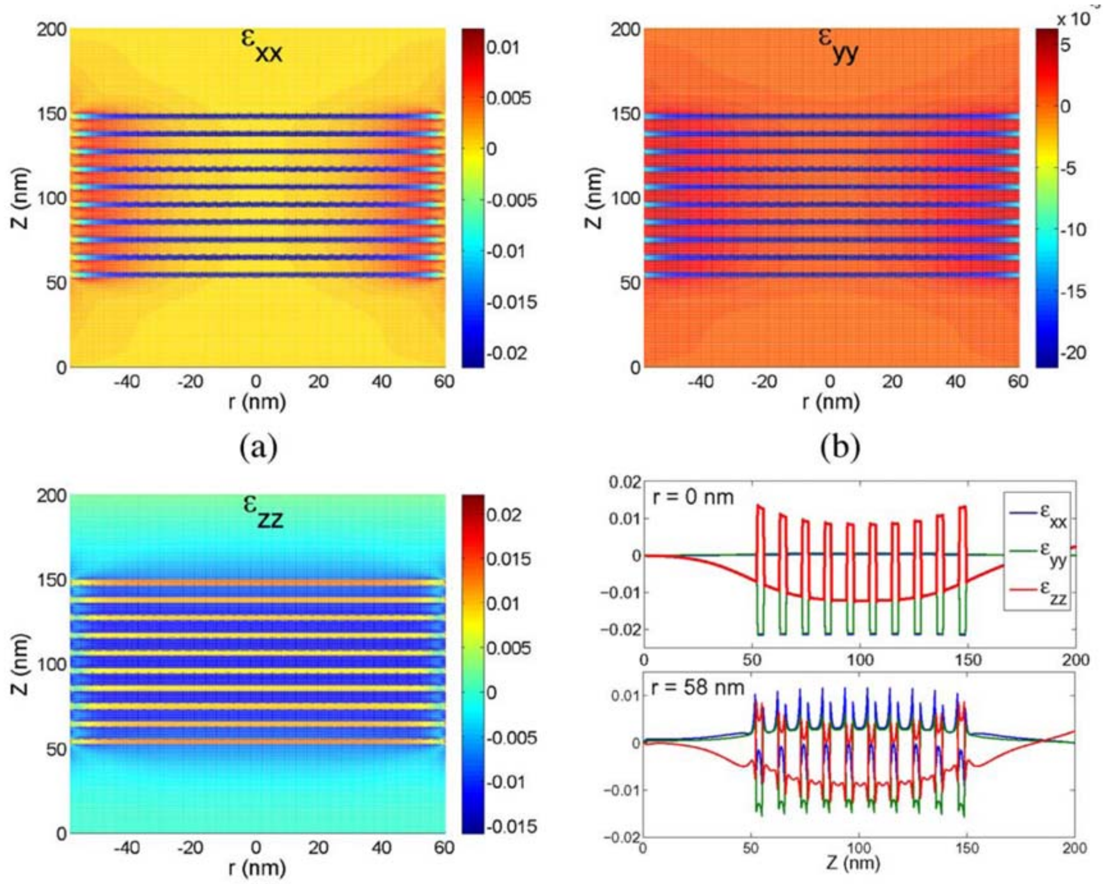

(a) (b)

(c) (d)

Figure 2.14 Calculated strain distributions of MQWs embedded in a free-standing, cylindrical-shaped nanorod with a height of *Z*=200 nm and a width of *d*=120 nm for (a) in-plane strain tensor ε_{xx} and (b) in-plane strain tensor ε_{yy} , (c) vertical strain tensor ε_{zz} , and (d) 2-D plots of strain tensors at the center and at the edge of the nanorod.

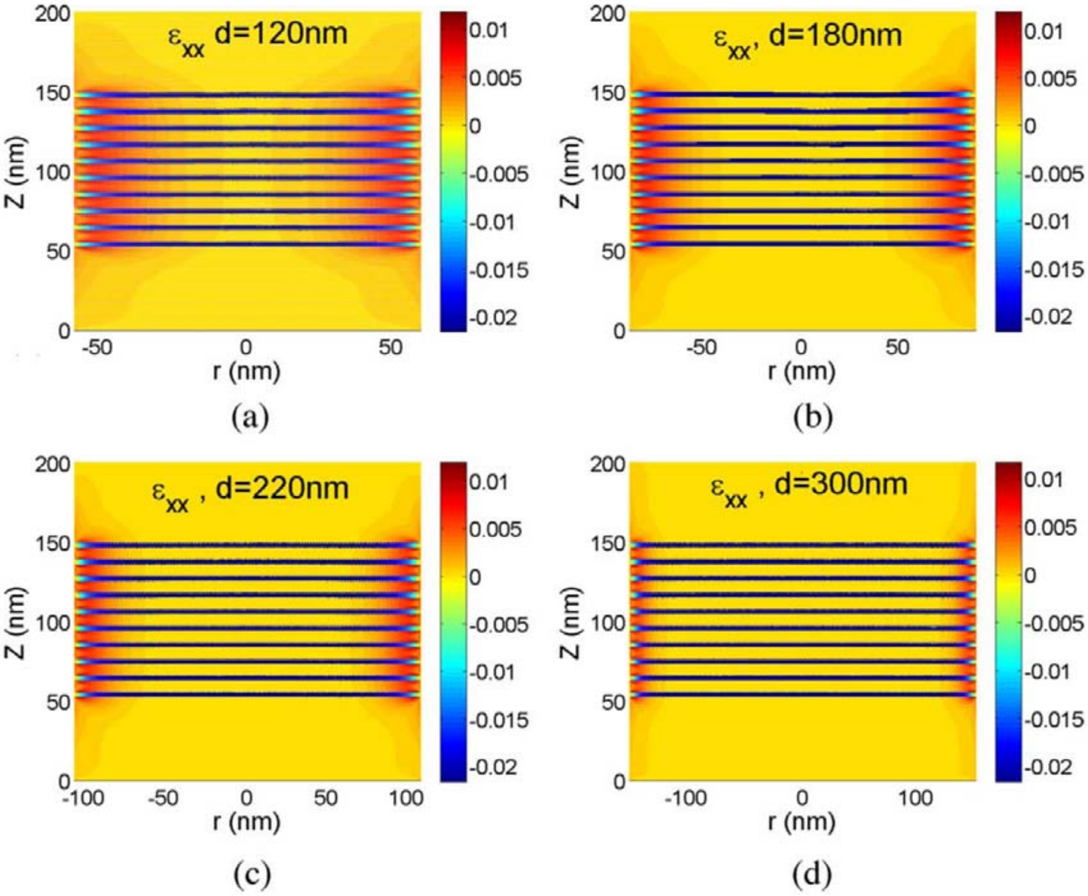

Figure 2.15 Calculated strain ε_{xx} for GaN nanorods with various averaged diameters. (a) 120 nm. (b) 180 nm. (c) 220 nm. (d) 300 nm.

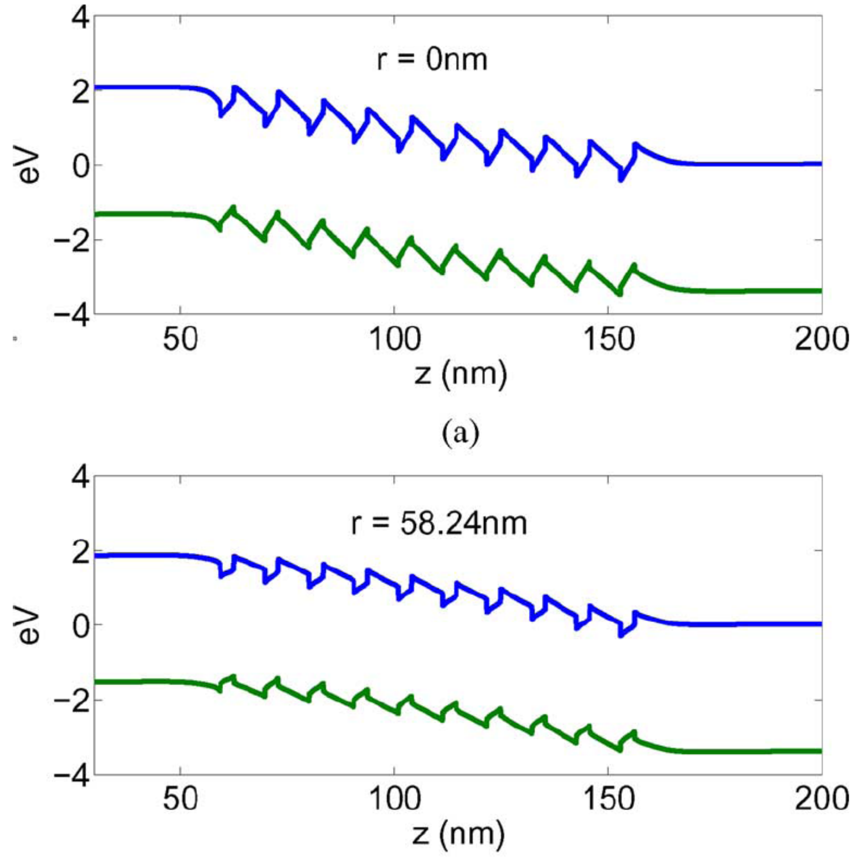

(a)

(b)

Figure 2.16 Calculated conduction and valence band profiles of the MQWs embedded in a nanorod with a diameter of 120 nm at (a) center (*r*=0 nm) and (b) edge (*r*=58.24 nm) of the nanorod.

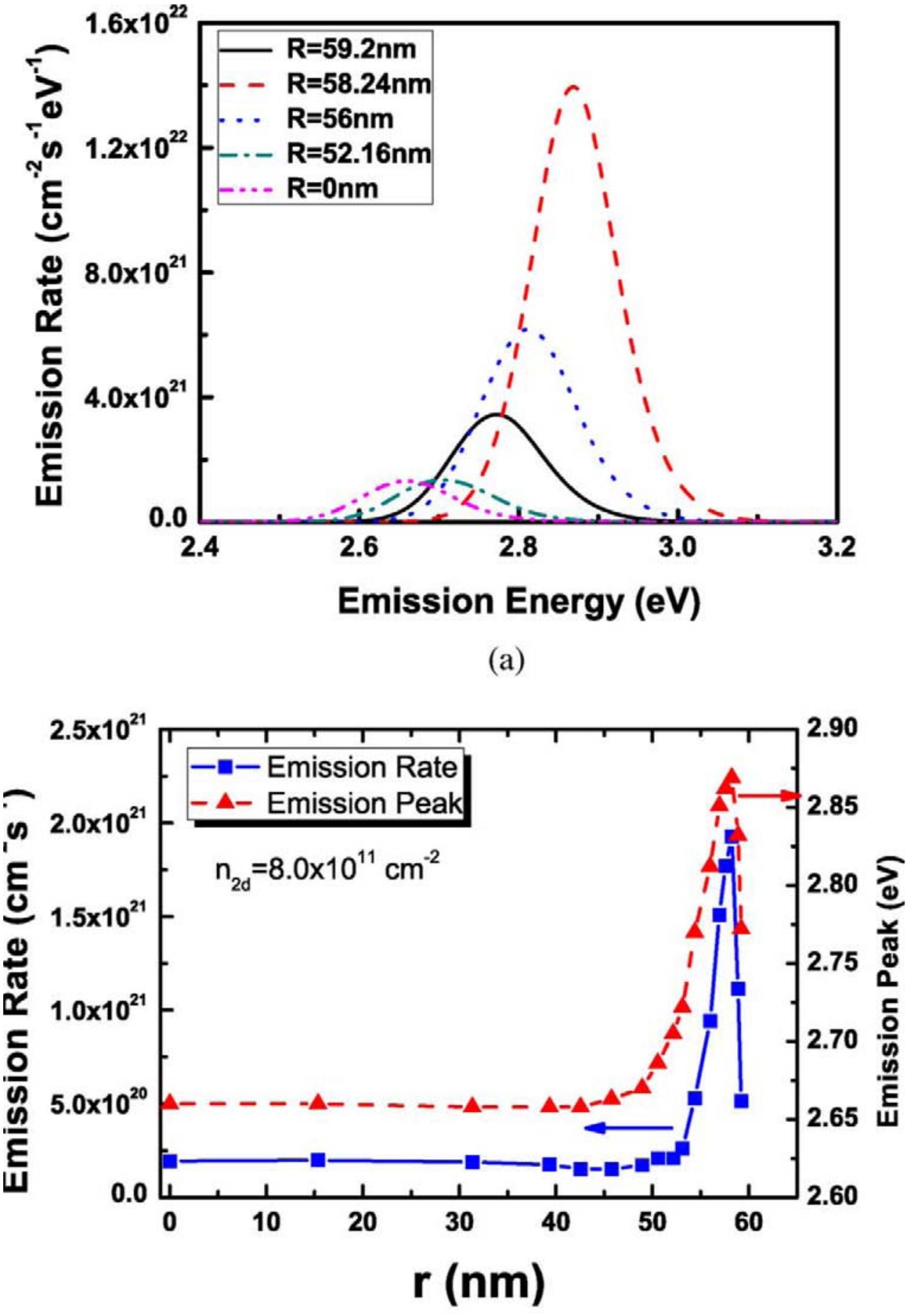

(a)

(b)

Figure 2.17 (a) Calculated spontaneous emission rates as a function of emission energy at different positions of the nanorod with a diameter of 120 nm under the injected electron density at 8 × 10^{11} cm^{-2}. (b) Calculated spectrum peak shift and emission rates from the center to the edge of the nanorod.

CHAPTER 3

High Efficiency Nano-structured GaN-based LEDs

Over the past decade, GaN-based LEDs have been extensively studied due to widely tunable emission wavelengths ranging from ultraviolet to blue/green. High-efficiency white light LEDs using GaN-based blue LEDs and phosphors have also received much interest for their potentials in a variety of applications, such as back lights for cell phones [1], outdoor displays [2], and most importantly, replacing incandescent or fluorescent mercury (Hg) and xenon (Xe) lamps for general lighting devices. However, a majority of applications are currently hindered by the low luminescence efficiency. As for the replacement of conventional fluorescent lighting sources with solid-state lighting, it is highly necessary to improve the ExE as well as IQE of LEDs. It is also well known that the external quantum efficiency (EQE) of the GaN-based LEDs is often low due to the large refractive index difference between the nitride epitaxial layer and the air. For GaN-based LEDs, the refractive indexes of GaN (n_{GaN}) and the air (n_{air}) are 2.5 and 1, respectively. Thus, the critical angle for the light generated in the InGaN–GaN active region to escape is about 23° [3]. This indicates that just a small fraction of light generated in the active region of the LED can escape to the surrounding air. Consequently, the external quantum efficiency of conventional GaN-based LEDs is limited to only a few percent. In order to increase the ExE from LEDs, it is very important that the photons generated into LEDs find the escape cone. In this chapter, we will first demonstrate a novel vertical-LED structure and combined the nano-technologies developed in the previous chapter into these LEDs. Three different types of vertical-LEDs will be introduced in this chapter.

3-1 High-aspect-ratio GaN Nanorod Vertical-LED

In this section, we attempted to fabricate a high-aspect-ratio GaN nanorod array on the surface of so-called vertical-LEDs. It could result in a rough surface and destroy the surface flatness; hence, lower the possibility of TIR happened at the GaN/air interface and result in a higher ExE. The high-aspect-ratio GaN nanorods were formed by spinning nano particles on the surface and performed the ICP dry etching. By well controlled the etching condition, we could have manually increase the etching selecting ratio between the spun nano particles and GaN material and forming a high-aspect-ratio GaN nanorods on the surface. The fabrication process and the device characteristics will be discussed in this section.

Fabrication process of vertical-LEDs

The schematic illustrations of the GaN-based vertical-LEDs process flow chart were shown in figure 3.1. The GaN-based LED structure with dominant wavelength at 460 nm used in this study was grown by MOCVD on *c*-plane sapphire substrates. The LED structure consists of 30-nm-thick low temperature GaN buffer layer, 2-μm-thick undoped GaN layer, a 2-μm-thick highly conductive n-type GaN layer, a 0.2-μm-thick 20 pairs of InGaN/GaN multiple quantum-well (MQW), a 0.2-μm-thick p-type GaN layer (figure 3.1(a)). A transparent conductive layer (TCL) was firstly deposited on the surface on the purpose of ohmic contact and current spreading. In our case, we used to deposit 250-nm-thick indium-tin-oxide (ITO) layer, Ni/Al or Ni/Ag alloy serving as the TCL. The general thickness of the Ni layer is less than 10 Å in order to maintain the good electrical conductivity and high transmission properties as well. Subsequently an adhesive/mirror comprised of Ti/Al/Ti/Au (2-μm-thick) was deposited by E-gun evaporator. A bonding metal alloy of Ti/Ni/AuSn with a thickness of 500/1000/20000 Å was deposited on the Si carrier substrate. Basically, the Si wafer has a higher thermal conductivity of 1.457 W/cm·°C [4] than sapphire of 0.35 W/cm·°C at room temperature. That means after the bonding process, the Si substrate played the role of a heat sink and we could dissipate large amount of generated heat from the Si substrate which enable us operate at a higher current injection condition.

After sample preparation, we then performed the bonding process to bond LED sample to the Si substrate. These two wafers were placed in contact with each other immediately using a designed fixture that ensured uniform pressure on each of the wafers. Then, the fixture was loaded into an oven and annealed at temperature of 350 ˚C for 30 min in nitrogen ambient (figure 3.1(b)). We note that we should control temperature profile during the whole bonding process especially the temperature cooling period. Since the thermal expansion coefficient (CTE) was different between these two wafers, $2.6\text{x}10^{-6}$ for Si and $2.6\text{x}10^{-6}$ $°\text{C}^{-1}$ for sapphire, the bonded sample might be crack if the we cooling down the samples too fast. The wafer-bonded samples were then taken to undergo the laser lift-off (LLO) process to remove the sapphire substrate and transfer the epi-structure onto the Si wafer. A KrF excimer laser (Lambda Physick LPX200) at wavelength of 248 nm with pulsewidth of 25 ns was used to remove the sapphire substrate (figure 3.1(c)). The incident laser flux was set to a value of about 0.6 J/cm^2. The laser beam with a size of 1.2 mm x 1.2 mm was incident from the polished backside of the sapphire substrate into the sapphire–GaN interface to decompose the GaN into Ga and N_2. The sample was placed on a 2-D stage with a precision controller.

Therefore, we could scan the whole samples with fixed laser power uniformly. After the entire LED wafer was illuminated by the laser beam, the sapphire substrate was separated from the bonded LED structure. The details of the LLO process can be described in [5].

The third part of the vertical-LED was the chip process. The first step is removing of u-GaN layer by ICP dry etching. By removing the un-GaN layer with poor electrical conductivity, we could deposit the contact metal on the exposed n-GaN layer to lower the operation voltage. The second step is to define the mesa structure with dimension of 1 x 1 mm^2 using standard photolithography and ICP dry etching processes for electrical current isolation (figure 3.1(d)). Then the exposed active region at the sidewalls of epi-layers was passivated by 240-nm-thick SiO_2 film layer to avoid possible leakage current by PECVD. After the surface of n-GaN was cleaned using diluted HCl : H_2O (1 : 1) solution for 1 min, a bonding pad comprised of Cr/Pt/Au was deposited by E-beam evaporator (figure 3.1(e))

.

3-1.1 Fabrication of high-aspect-ratio GaN nanorod vertical-LEDs

Here, we take the vertical-LEDs prepared in the previous paragraph for the following high-aspect-ratio GaN nanorod fabrication process. The self-assembled silica nanospheres were employed as the lithographic and etch masks as shown in figure 3.2, which provide greater etching selectivity to n-GaN layer than other polymers. The silica spheres were first suspended in deionized (DI) water diluted in a solution of surfactant at a volume ratio of 5 : 1, and then spin-coated on the n-GaN surface, followed by heating treatment for adhesion. The surfactant can lower the surface tension and then help the particles spread across the GaN surface. The coated sample was then etched by ICP-RIE, using Cl_2 and Ar as the etch gases at a fixed flow rate of 45 and 30 sccm, respectively. The ICP source power and, bias power and chamber pressure were set to be 400/100 W and 0.66 pa. The etching time was about 4 min. The device was immersed in DI water with sonification for 3 min to remove residual silica particles. Finally, a bonding pad comprised of Cr–Pt–Au was deposited by electron-beam evaporation on the back side of Si substrate.

3-1.2 Characteristics of high-aspect-ratio GaN nanorod vertical-LEDs

The results of the fabricated device like SEM images, device performance and simulation results will be discussed in this section.

SEM images

Figure 3-3(a) shows the SEM image of the spin-coated silica spheres on GaN. The closely packed silica nanospheres have a mean diameter of 100 nm with a uniformity of better than 1%. The cross-sectional SEM image of the fabricated nanorod arrays patterned by silica spheres is shown in figure 3.3(b). These nanorods are vertically aligned to the surface normal of GaN and uniformly distributed over the entire surface. Moreover, the dense nanorod arrays exhibit uniform dimensions with a base diameter of 200 nm and a length of 1.3 m, which resemble cone structures. Since the dimensions of nanorods are comparable to the emission wavelength, the spatially varied rod profiles can enhance optical transmission by collectively functioning as a gradient index layer, similar to that of a zero-order grating [6]. The enhancement in light extraction is also verified by finite-difference time-domain (FDTD) calculations.

Device performance

The forward current–voltage (*I*–*V*) characteristics at room temperature for the high-aspect-ratio GaN nanorod vertical-LEDs with and without nanorod arrays are plotted in figure 3.4. The measured forward voltages at an injection current of 350 mA for vertical-LEDs with and without nanorod arrays are 4.69 and 4.50V, respectively. The slightly increased forward voltage for the vertical-LEDs with nanorod arrays is attributed to the reduced lateral-current spreading on n-GaN, giving rise to a slightly increased resistivity. Nonetheless, both *I*–*V* curves are nearly identical, indicating the negligible impact of nanorod arrays. Figure 3.4 also shows the corresponding light output intensity versus forward current (*L*–*I*) characteristics. At an injection current of 350 mA, the light output power of the vertical-LEDs with nanorod arrays is 316 mW, approximately enhanced by 40% compared to that without nanorods, 226 mW. The peak emission wavelength is the same as that of a conventional vertical-LED, occurring at 465 nm. The inset of figure 3.4 demonstrates the uniform illumination from the VI-LEDs with nanorod arrays at a driving current of 350 mA under an optical microscope. The measured far-field emission profiles are shown in figure 3.5 for vertical-LEDs with and without nanorod arrays. As seen in figure 3.5, the emission from vertical-LEDs with high-aspect-ratio nanorods is mainly enhanced along the surface normal view angle of 30°. The integrated intensity is improved by a factor of 38% within a view angle of 20°.

Simulation results

A two-dimensional finite-difference time-domain (FDTD) method with perfectly matched layer boundary within a condition is employed to investigate the emission characteristics from high-aspect-ratio nanorod arrays. The simulated far-field patterns are plotted in figure 3.6 for comparison. Figure 3.6(a) and (b) show the snap shots of wave propagating across a GaN–air interface and an interface with nanorod arrays, respectively. The time-varying current-excited radiation source is placed 2 m below the GaN–air interface. The dimensions of nanorods are extracted from the SEM picture shown in figure 3.3. As shown in figure 3.5, a conventional GaN–air interface results in Lambertian-like radiation patterns with a view angle at the full-width at half-maximum of 120°. The radiation pattern from the nanorod arrays is relatively collimated 100°. As shown in figure 3.6(b), the nanorods suppress the TIR at GaN–air interface, effectively reducing the energy confined in GaN slab. The light extraction enhancement is due to similar mechanisms provided by other surface roughness techniques. However, as shown in Fig. 4(c), the nanorods also act as waveguiding channels for the emitted light, resulting in a relatively collimated radiation pattern. Calculations show that the height of nanorods to be at least a few wavelengths long to provide a sufficient guiding effect. Moreover, the closer the nanorod array to MQWs, the better the directionality. However, the distance in this device is limited to 1 m, which is optimized for current spreading.

3-2 Integrating ZnO Nanorod Arrays on GaN-Based Vertical-LEDs

In previous section, we had demonstrated a high efficiency GaN-based vertical LEDs by fabricating high-aspect-ratio GaN nanorod on the surface. However, we would also investigate a slightly increased operation voltage because the etching process would unavoidably thin the n-GaN layer and decrease the current spreading path as shown in figure 3.7. Therefore, it is interesting to find out another method to reach an improvement in light output power but still keep the good lateral current spreading. Therefore, in this section, we try to find a bottom-up method to form a rough surface and improve the device performance. The details of fabrication process and device characteristics will be discussed in this section.

3-2.1 Synthesize of ZnO nanorod array

Similar to previous part, we take the vertical-LEDs and synthesize the ZnO nanorod on the surface to improve the ExE. ZnO nanorod arrays were synthesized on the surface of the GaN-based vertical-LED n-side surface to provide an omnidirectional extraction surface and the gradually changed effective refractive index. A 15 nm thick ZnO thin films were first deposited on the n-GaN surface of the vertical LED by radio-frequency magnetron sputtering [7]. Zinc nitrate hexahydrate $[Zn(NO3)_2 \cdot 6H_2O]$ was used as the zinc precursor to synthesize the ZnO nanorod arrays. Methenamine ($C_6H_{12}N_4$), also called hexamethylenetetramine

(HMT), is a highly water-soluble, nonionic tetradentate cyclic tertiary amine used to comply simultaneously with the precipitation of the divalent post-transition metal Zn^{2+} ions, the nucleation growth of its stable oxide form, zincite ZnO. An equimolar (0.02 M) aqueous solution of $Zn(NO_3)_2 \cdot 6H_2O$ and HMT was prepared in a bottle. Subsequently, the GaN-based vertical-LED samples were placed inside the aqueous solutions at room temperature with a synthesis time of 5 h. After that, the GaN-based vertical-LED samples were removed from the aqueous solutions, rinsed with distilled water, and dried at room temperature overnight. The schematic of the proposed structure is shown in figure 3.8. The details of synthesizing the ZnO nanorod arrays can be found in [8].

3-2.2 Characteristics of integrating ZnO nanorod vertical-LEDs

The experiment results of the fabricated device will be discussed in this section.

SEM images

SEM images of the GaN-based vertical-LEDs with ZnO nanorod arrays synthesized in aqueous solutions at room temperature are shown in figure 3.9. Figure 3.9(a) shows the cross-sectional image of the synthesized ZnO nanorod arrays with dimensions of 30–90 nm in diameter and 100–300 nm in length, respectively. The random-sized ZnO nanorod arrays not only provide an omnidirectional extraction surface but a layer with a gradually changing refractive index, which could increase the probabilities for light extraction [9]. According to our previous work, the dimensions of the synthesized ZnO nanorod arrays could be controlled by the concentration of the aqueous solution and the growth time. The SEM images of the ZnO nanorod arrays on different surfaces, n-GaN, contact metal, and passivated SiO2 film, are shown in figure 3.9(b)-(d). The well-aligned high density, about 1.5×10^{10} cm^{-2}, of the synthesized ZnO nanorod arrays on the n-GaN surface is shown in figure 3.9(b). The growth direction of the synthesized ZnO nanorod arrays on the n-GaN surface is perpendicular to the n-GaN surface. In contrast to the n-GaN surface, there were nearly no ZnO nanorod arrays synthesized on the metal surface, as shown in figure 3.9(c). Figure 3.9(d) shows the SEM images of the passivated SiO_2 surface and a lower density, about 4×10^9 cm^{-2}, of ZnO nanorod arrays could be observed. This observation strongly reveals the importance of surface characterization on the growth behavior of the ZnO nanorods in the aqueous solution.

Device performance

Figure 3.10 shows the forward *I-V* curves for the GaN-based vertical-LED with ZnO nanorod arrays and that without ZnO nanorod arrays. It was found that the measured forward voltages under 200 mA injection currents at room temperature for the GaN-based LLO LED with ZnO nanorod arrays and that without ZnO nanorod arrays were approximately 4.26 and 4.33 V, respectively. The slightly lower forward voltage of the vertical-LED with ZnO nanorod arrays than that without ZnO nanorod arrays could be attributed to the current spreading layer of the synthesized ZnO layer on the surface. Figure 3.11 shows that the light-output intensity and the wall-plug efficiency (WPE) vs forward dc current for the GaNbased vertical-LED with ZnO nanorod arrays and that without ZnO nanorod arrays are taken as continuous-wave. At an injection current of 200 mA, the light-output powers of the GaN-based vertical-LED with ZnO nanorod arrays and that without ZnO nanorod arrays were approximately 220 and 158 mW, respectively. The emission wavelength of the GaN-based vertical-LEDs with and without ZnO nanorods were both at 460 nm. The GaN-based vertical-LED with ZnO nanorod arrays increased the output power intensity by a factor of 1.39, indicating that ZnO nanorod arrays provided an omnidirectional extraction surface with a gradually changing refractive index and had better light extraction efficiency than that without ZnO nanorod arrays. The WPE varies in a similar manner as the output power with forward dc current. The WPE of the GaN-based vertical-LED with ZnO nanorod arrays is 1.41 times higher than that without ZnO nanorods under all our measurement conditions. According to figure 3.11, at a driving current of 200 mA, the WPE values for the GaN-based vertical-LED, with and without ZnO nanorod arrays, were 25.8 and 18.3%, respectively.

To further investigate the influence of the omnidirectional extraction surface by ZnO nanorod arrays on light output performance of the GaN-based vertical-LEDs, intensity distribution measurements were performed on that with and without ZnO nanorod arrays. Figure 3.12(a) and (b) shows the photos of the GaN-based vertical-LEDs, with and without ZnO nanorod arrays, with injecting a 200 mA dc current in these two different devices, respectively. Each intensity distribution is also shown in the same figure. The electroluminescence intensities observed from GaN-based vertical-LEDs with ZnO nanorod arrays were obviously greater than those observed from that without ZnO nanorod arrays at the same injection current at the top surface area. Such an enhancement could be attributed to the omnidirectional extraction surface by ZnO nanorod arrays allowing photons to have a larger probability of being emitted from the device in the top emission direction, thus achieving even brighter LEDs.

3-3 GaN-based LEDs Regrowth on Nano-Patterned Sapphire Substrate

We had demonstrated two different kinds of vertical-LEDs with surface nano structure to form a roughened surface and improve the device luminescence efficiency. However, both structures were applied on the platform of vertical-LEDs which was more complex in fabrication process. Also, both of them were working on roughing the top surface. Therefore, we then try to develop a new method to improve the efficiency effectively on traditional sapphire structure instead of the vertical-type structure. In the third section of this chapter, we adopted the nanorod fabrication method to fabricate a SiO_2 nanorods structure on the surface of sapphire substrate serving as a nanorod-array patterned sapphire substrate (NAPSS). Then we regrowth LED epi-layers on the NAPSS by nanoscale epitaxial lateral overgrowth (NELO) method. It not only benefit to ExE by scattered the backside emission light upward, but also good for improve the crystal quality and enhance the IQE. The detail of the fabrication process and device performance will be discussed in this section.

3-3.1 Fabrication process of SiO_2 NAPSS

The preparation of the SiO_2 NAPSS template started with the deposition of a 200-nm-thick SiO2 layer on a *c*-face (0001) sapphire substrate by PECVD, followed by the evaporation of a 10-nm-thick Ni layer, and the subsequent rapid thermal annealing with a flowing nitrogen gas at 850 °C for 1 min. The resulting self-assembled Ni clusters then served as the etch masks to form a SiO_2 nanorod array using a reactive ion etch system for 3 min. Finally, the sample was dipped into a heated HNO3 at 100 °C for 5 min to remove the residual Ni masks.

3-3.2 Characteristics of GaN-based LEDs on SiO_2 NAPSS

The SEM images of NAPSS and the device characteristics will be shown and discussed in this section.

SEM images

Figure 3.13 shows the SEM images indicating that the fabricated SiO2 nanorods were approximately 100-150 nm in diameter with a density of 3 x 10^9 cm^{-2}. The spacing between nanorods was about 100-200 nm. Figure 3.13(a) also shows that the exposed sapphire surface was flat enough for epitaxy. As the deposition process began, localized and hexagonal islandlike GaN nuclei were first formed from the sapphire surface to initiate GaN overgrowth, as shown in figure 3.13(b). Figure 3.13(c) shows the cross-sectional SEM image of the GaN epilayer, where voids with a size varying from 150 to 200 nm were observed between the highlighted SiO_2 nanorods. The existing of the voids between nanorods observed from the micrographs suggested that not all the exposed surface enjoyed the same growth rate. Hence, only the regions with higher growth rates, which might be originated from larger exposed surface, could play the role of a seed layer, facilitating the lateral coalescence of GaN. Lastly, the growth of a conventional LED structure, which consists of ten periods of InGaN/GaN MQWs and a 100-nm-thick p-GaN layer, was completed by MOCVD. The p-GaN layer of the NAPSS LED was grown at the relatively low temperature of 800 °C, leading to the formation of hexagonal pits due to insufficient migration length of Ga atoms [10]. The SEM image of the roughened p-GaN surface with randomly distributed pits is shown in figure 3.13(d).

TEM images

The TEM was employed to investigate the crystalline quality of GaN layers epitaxially grown on a planar sapphire substrate and on a NAPSS. As shown in figure 3.14(a), the threading dislocation density (TDD) of GaN on the planar sapphire substrate was higher than 10^{10} cm^{-2} due to both the large lattice mismatch (13%) and the high thermal coefficient incompatibility between sapphire and GaN. On the other hand, the crystalline quality of GaN epilayer on a NAPSS was drastically improved from that grown on a planar sapphire substrate, as shown in figure 3.14(a). We found that a number of stacking faults often occurred above the voids between SiO_2 nanorods, where visible threading dislocations (TDs) were rarely observed in the vicinities. It is believed that the presence of stacking faults could block the propagation of TDs [11]. Moreover, the TDs of the GaN layer on a NAPSS mainly originated from exposed sapphire surface, which could be bent due to the lateral growth of GaN. The inset of figure 3.14(b) shows the TEM image of the dislocation bending with visible turning points. We summarized four potential mechanisms that were involved in the suppression of TDD, denoted as Types 1-4 and illustrated in figure 3.15.

As shown in figure 3.15(a), the TDs originated from the sapphire surface during the initial formation GaN growth seeds on a NAPSS. The presence of voids confirmed the lateral coalescence of GaN, leading to the bending of dislocations near the edge of SiO^2 nanorods. The bent TD eventually developed into stacking faults [12], as depicted by Type 1 in figure 3.15(b). Moreover, the coalescence fronts of GaN seeds provided a strain release layer where stacking faults could occur. These stacking faults were found mostly above the voids or the small GaN seeds [13], blocking the TD propagation, denoted as Type 2. Occasionally, the blocked dislocation might also be bent to form stacking faults [14]. If the growth rate was too slow to be a GaN seed, the dislocation could be blocked by the formation of voids, as illustrated by Type 3. Finally, we believed that the residual SiO2 between nanorods could prohibit the GaN growth and further reduce the dislocation formation from sapphire surface, as depicted by Type 4. It is also worth noting that the density of voids in the SiO_2 NAPSS was higher than that of a microscale PSS. Therefore, we believe that the formation of stacking faults and voids were involved in the reduction and bending of dislocations.

Device performance

The completed epitaxial structure then underwent a standard four-mask LED fabrication process with a chip size of 350 x 350 μm^2 and packaged into TO-18 with epoxy resin on top. The schematic of a fabricated NAPSS LED is shown in the inset of figure 3.16. The *I-V* characteristics of the NAPSS LED and a conventional LED with the same chip size were measured at room temperature, as shown in figure 3.16. The forward voltages at 20 mA were 3.27 V for the conventional LED and 3.31 V for the NAPSS LED.

The nearly identical *I-V* curves indicate that the nanoscale roughness on the p-GaN surface had little impact on the *I-V* characteristics. Moreover, the NELO of GaN did not deteriorate the electrical properties. Figure 3.17 shows the measured *L-I* curve for the NAPSS and conventional LED. At an injection current of 20 mA, the light-output powers were approximately 22 and 14 mW for the NAPSS and the conventional LEDs, respectively. The output power of the NAPSS LED was enhanced by a factor of 52% compared to that of the conventional LED. The inset shows the normalized electroluminescence spectra for both devices at an injection current of 20 mA. A minor wavelength blueshift of ~2 nm was observed for the NAPSS LED, attributed to the partial strain release by adopting the NELO scheme [15]. The EQE of the NAPSS LED was calculated to be ~40.2%, which is an increase of 56% when compared to that of the conventional LED, ~25.7%. We believe that the 56% enhancement in EQE originated from the improved IQE and the enhanced ExE. The SiO_2 NAPSS-assisted NELO method effectively suppressed the dislocation densities of GaN-based LEDs, which increased the IQE. Moreover, the embedded SiO_2 nanorods in the GaN epilayer contributed to light extraction due to scattering at the interfaces of different refractive indices. Ueda *et al* [16] reported that the output power linearly increased with the surface coverage ratio of nanosilica spheres. Therefore, the extraction efficiency was enhanced by the SiO_2 nanorod array.

Reference:

1 Y. Narukawa, I. Niki, K. Izuno, M. Yamada, Y. Murazki, and T. Mukai, Japan Journal of Applied Physics **41**, L371 (2002).

2 E. F. Schubert and J. K. Kim, Science **308**, 1274 (2005).

3 C. Huh, K. S. Lee, E. J. Kang, and S. J. Park, Journal of Applied Physics **93**, 9383 (2003).

4 H. R. Shanks, P. D. Maycock, P. H. Sidles, and G. C. Danielson, Physics Review, **130**, 1743 (1963).

5 C. F. Chu, F. I. Lai, J. T. Chu, C. C. Yu, C. F. Lin, H. C. Kuo, and S. C. Wang, Journal of Applied Physics **95**, 3916 (2004).

6 Y. F. Huang, S. Chattopadhyay, Y. J. Jen, C. Y. Peng, T. A. Liu, Y. K. Hsu, C. L. Pan, H. C. Lo, C. H. Hsu, Y. H. Chang, C. S. Lee, K. H. Chen, and L. C. Chen, Nature Nanotechnology **2**, 770 (2007).

7 C. C. Lin, C. S. Hsiao, S. Y. Chen, and S. Y. Cheng, Journal of Electrochemical Society **151**, G285 (2004).

8 S. C. Liou, C. S. Hsiao, and S. Y. Chen, Journal Crystal Growth **274**, 438 (2005)

9 J. Zhong, H. Chen, G. Saraf, Y. Lu, C. K. Choi, J. J. Song, D. M. Mackie, and H. Shen, Applied Physics Letter **90**, 203515 (2007).

10 Y. J. Lee, H. C. Kuo, T. C. Lu, and S. C. Wang, IEEE Journal of Quantum Electronics **42**, 1196 (2006).

11 Z. H. Feng, Y. D. Qi, Z. D. Lu, and K. M. Lau, Journal of Crystal Growth **272**, 327(2004).

12 D. S. Wuu, W. K. Wang, K. S. Wen, S. C. Huang, S. H. Lin, R. H. Horng, Y. S. Yu, and M. H. Pan, Journal of Electrochemical Society **153**, G765 (2006).

13 T. Nagai, T. Kawashima, M. Imura, M. Iwaya, S. Kamiyama, H. Amano,and I. Akasaki, Journal of Crystal Growth **298**, 288 (2007).

14 H. K. Cho, J. Y. Lee, K. S. Kim, G. M. Yang, J. H. Song, and P. W. Yu, Journal of Applied Physics **89**, 2617 (2001).

15 K. Kusakabe, A. Kikuchi, and K. Kishino, Japan Journal of Applied Physics **40**, L192 (2001).

16 K. Ueda, Y. Tsuchida, N. Hagura, F. Iskandar, K. Okuyama, and Y. Endo, Applied Physics Letter **92**, 101101 (2008).

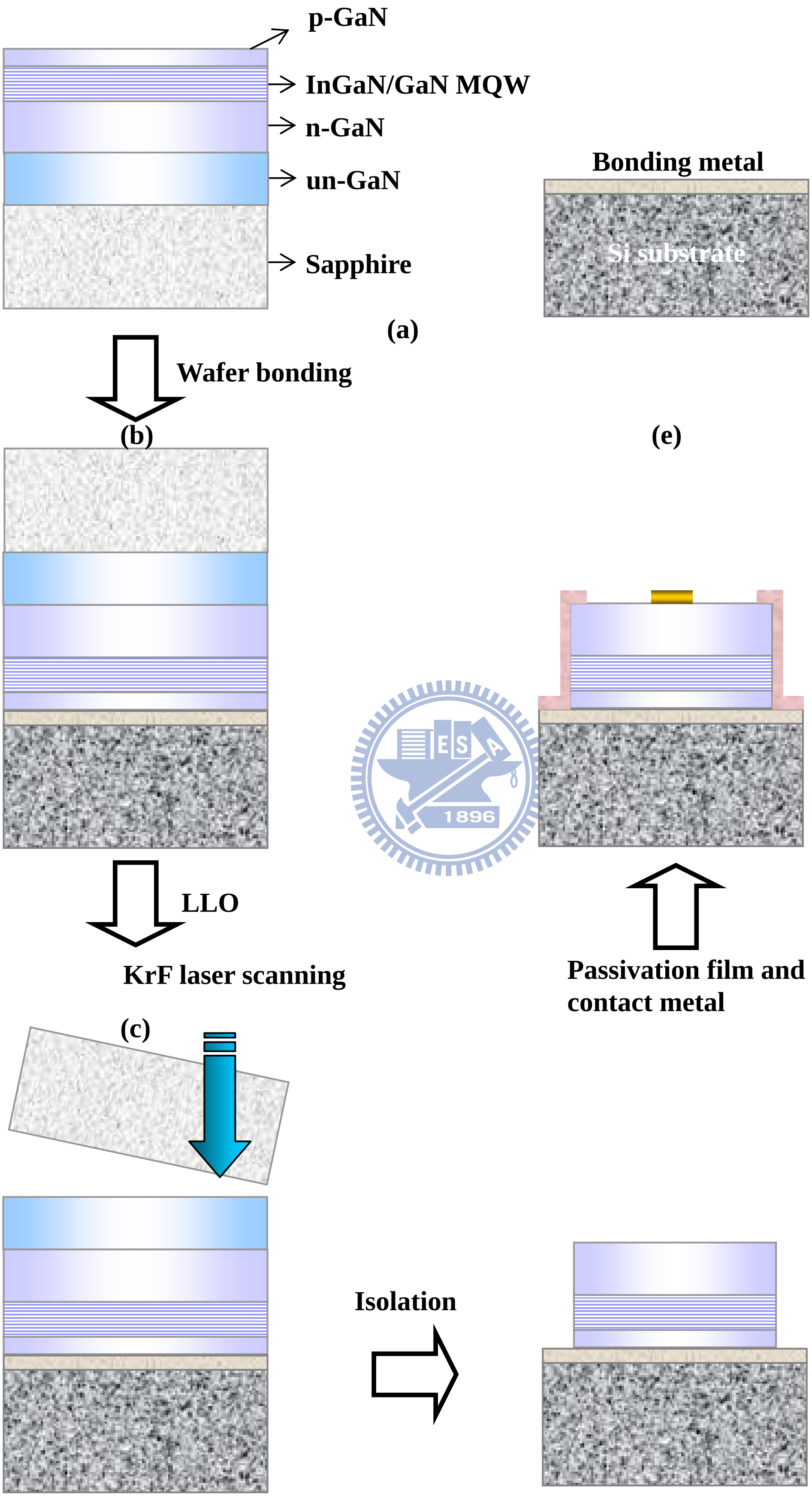

Figure 3.1 The schematic illustrations of the GaN-based vertical-LEDs process flow chart.

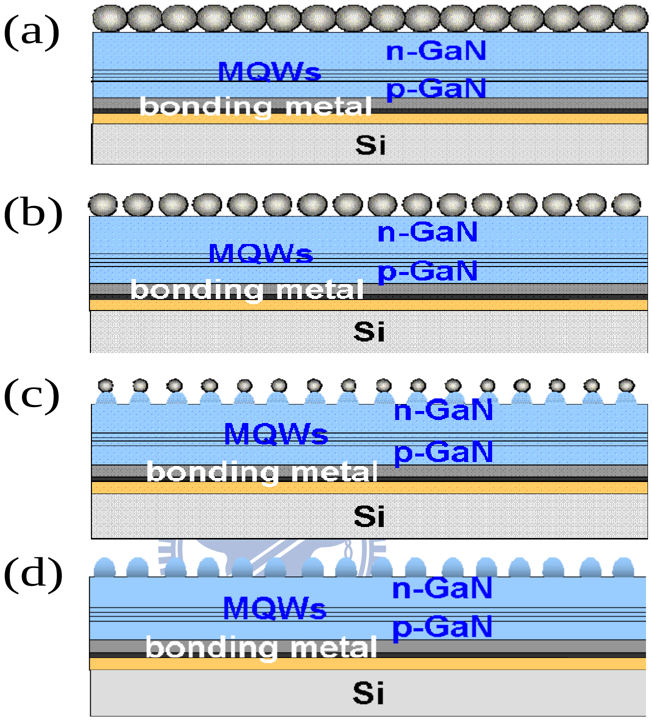

Figure 3.2 Schematics of the fabrication of high-aspect-ratio GaN nanorods utilizing the self-assembled silica nanospheres on the n-type GaN layer: (a) a monolayer of silica nanospheres by spin coating; (b) the formation of self-assembled surface structures after ICP and (c) the removal of residual nanospheres.

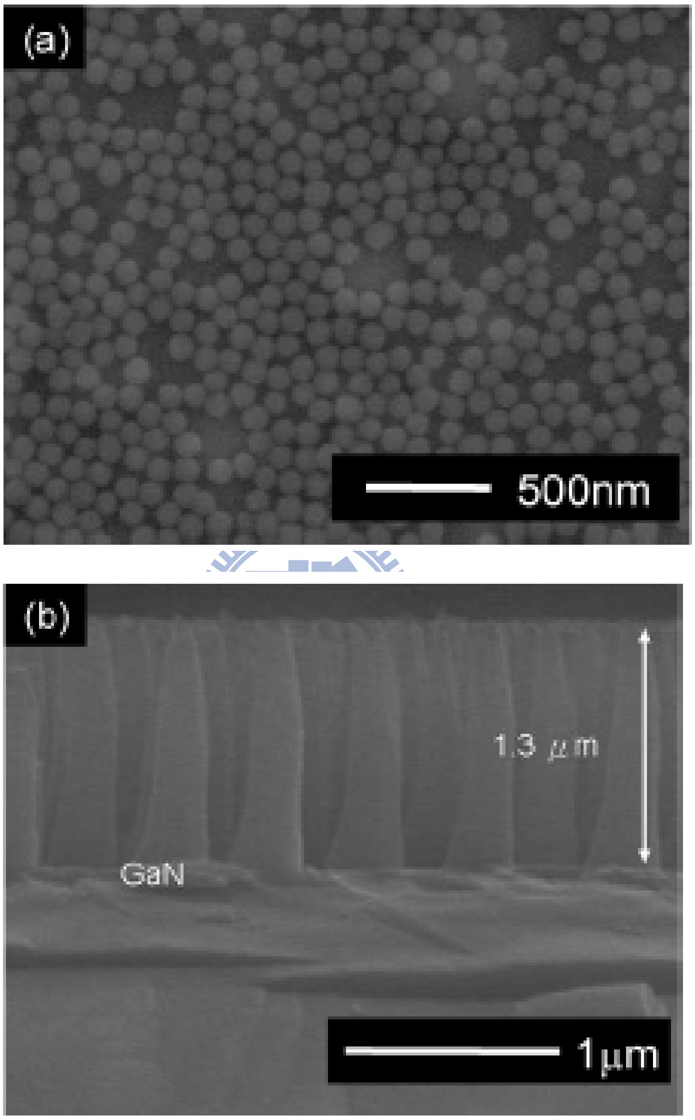

Figure 3.3 SEM images of (a) the densely packed silica spheres on GaN, showing a mean diameter of ~100 nm with a uniformity of better than 1%; (b) the cross-sectional view of the fabricated nanorods with a base diameter of 200 nm and a height of 1.3 μm, similar to cone structures.

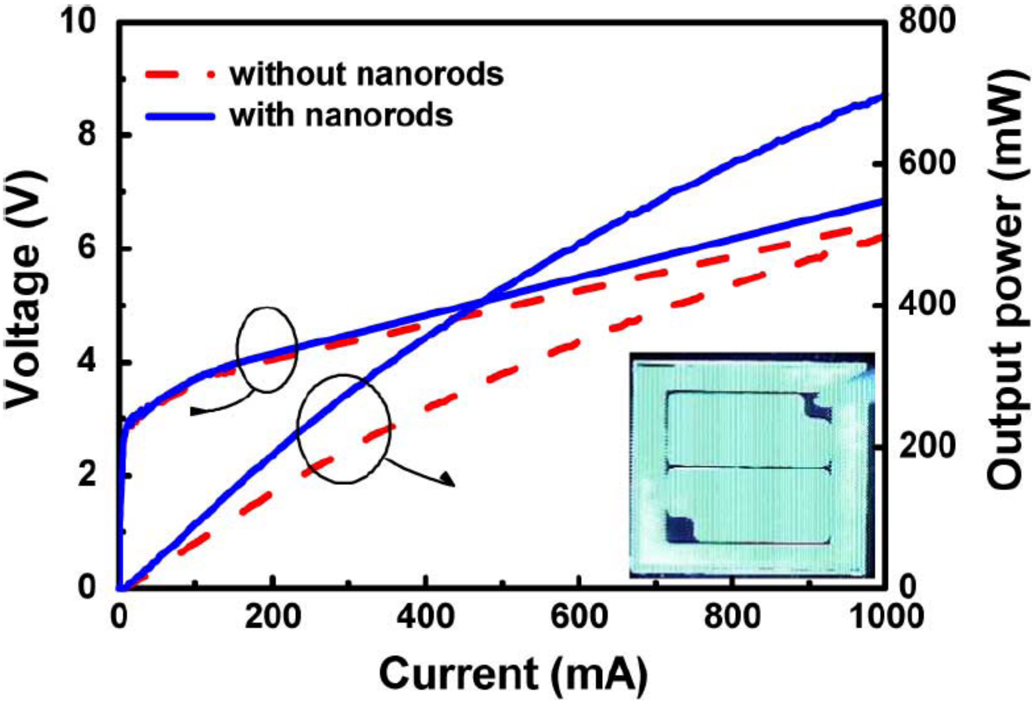

Figure 3.4 Voltage and light output intensity versus forward current characteristics for a conventional GaN-based vertical-LED (without nanorods) and the vertical-LEDs with nanorod arrays. The inset shows the uniform light emission from the vertical-LEDs with nanorod arrays at a driving current of 350 mA.

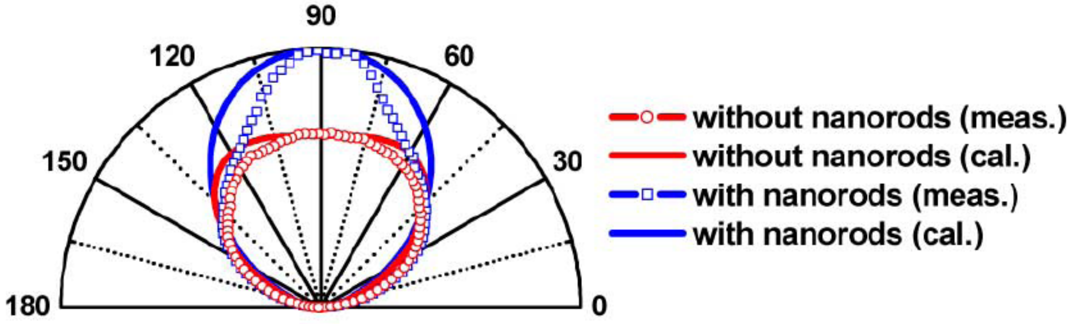

Figure 3.5 Measured and simulated emission profiles of GaN-based vertical-LEDs with and without nanorod arrays.

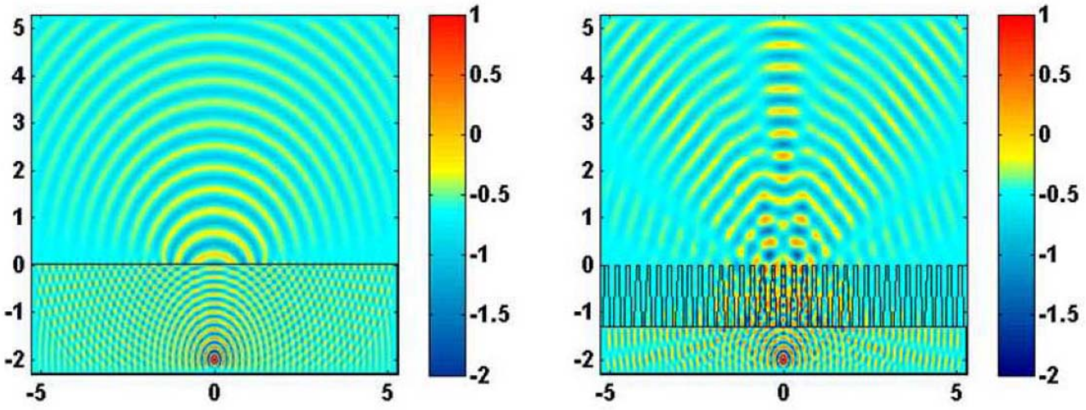

(a) (b)

Figure 3.6 The simulated wave propagation results of vertical-LEDs (a) without and (b) with high-aspect-ratio GaN nanorods.

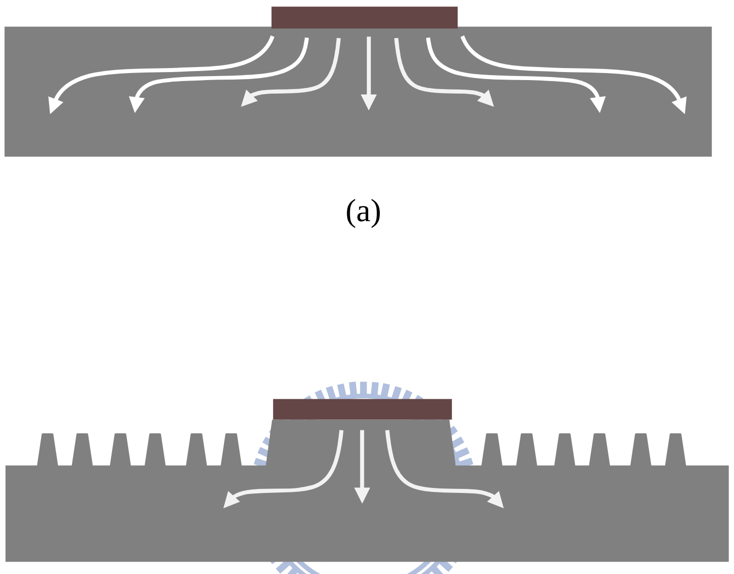

(a)

(b)

Figure 3.7 The schematic of reduced current spreading path (a) before and (b) after GaN nanorod formation by ICP etching.

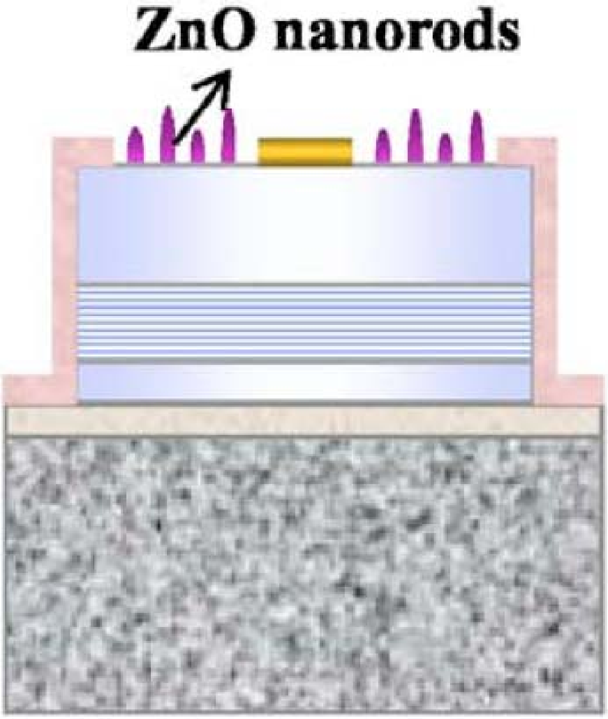

Figure 3.8 The proposed structure of vertical-LEDs with synthesized ZnO nanorods on the surface

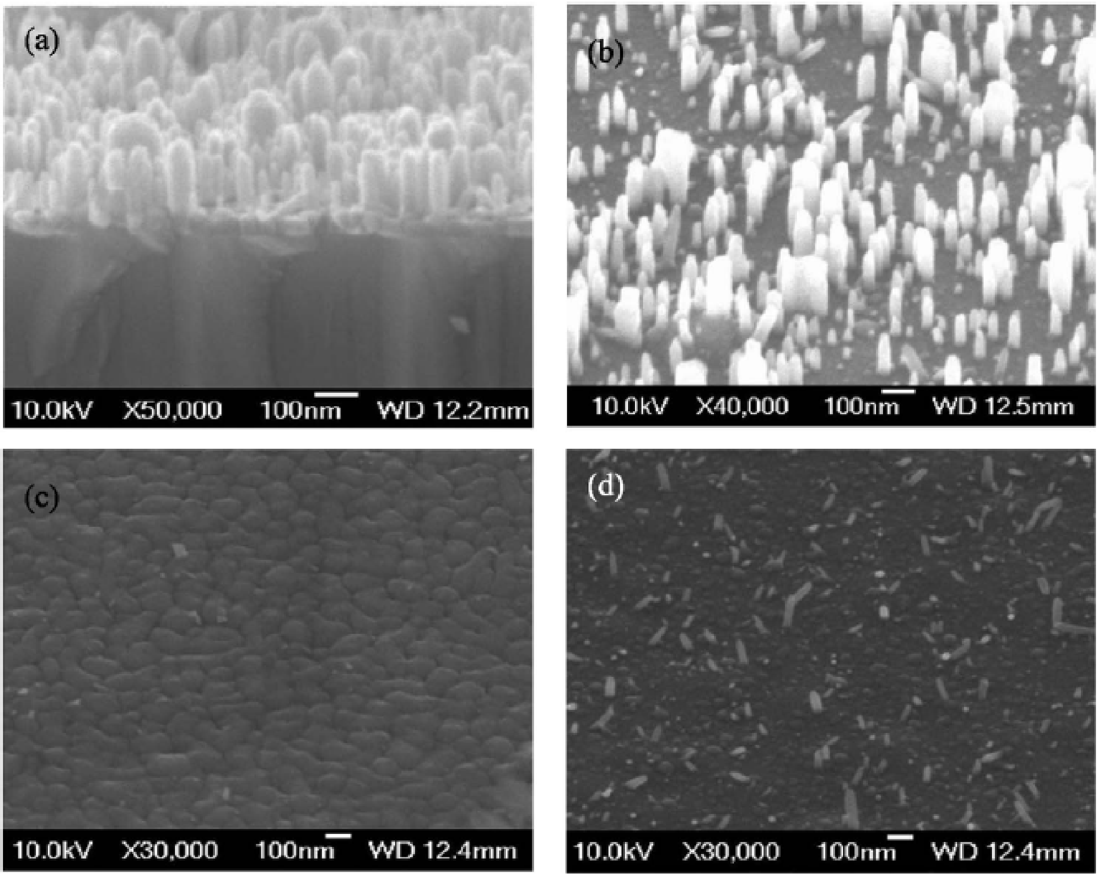

Figure 3.9 SEM images of the GaN-based vertical-LEDs with ZnO nanorod arrays: (a) cross-sectional image of the synthesized ZnO nanorod arrays, (b) images of the n-GaN surface, (c) images of the bonding pad metal surface, and (d) images of the passivation SiO_2 surface.

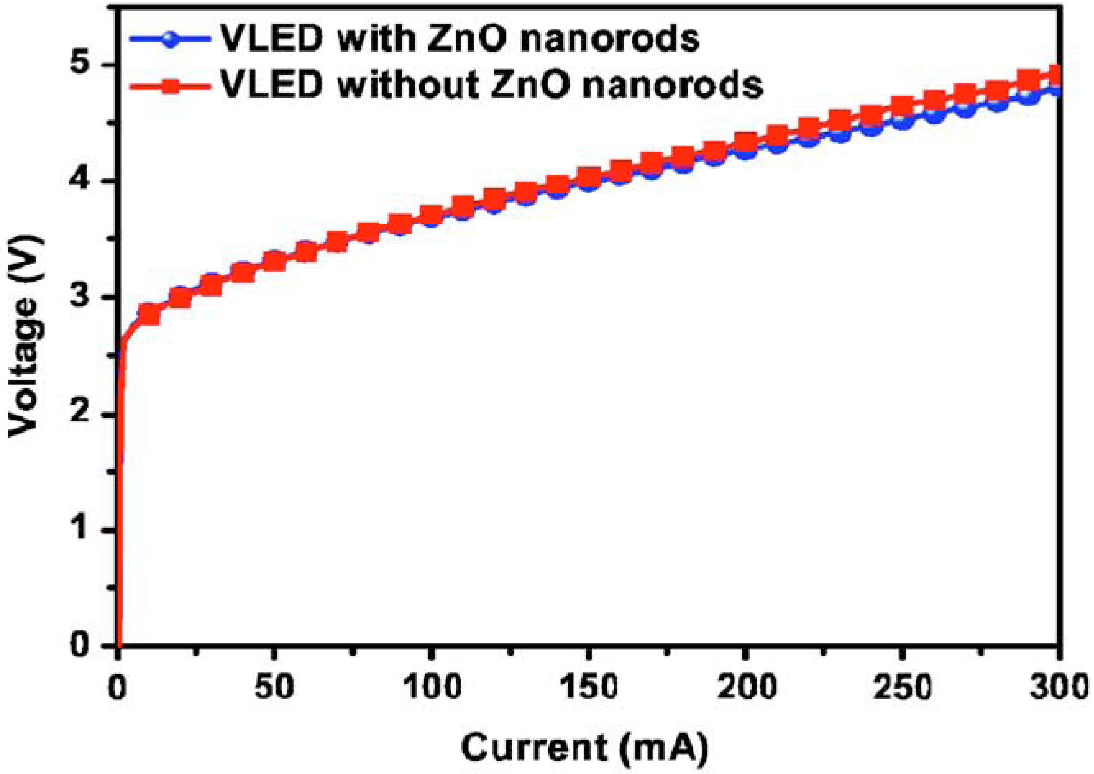

Figure 3.10 Curves of vertical-LEDs with and without ZnO nanorods on n-GaN surface.

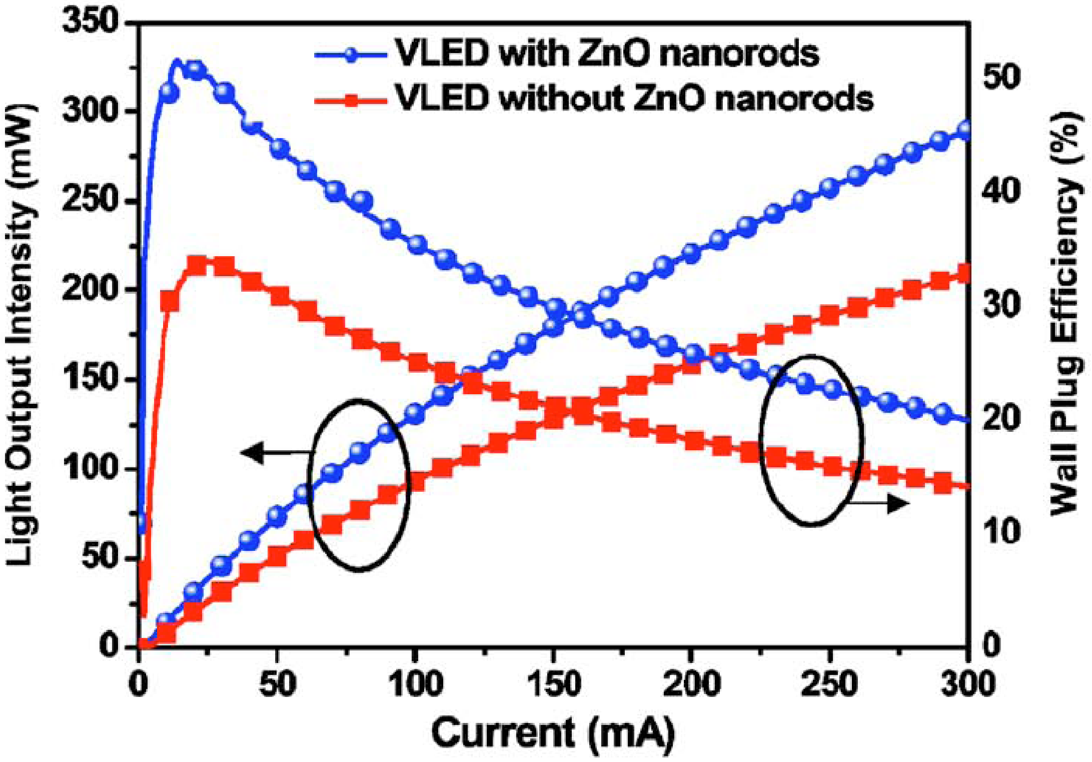

Figure 3.11 Light output power and wall plug efficiency curves of vertical-LEDs with and without ZnO nanorods on n-GaN surface.

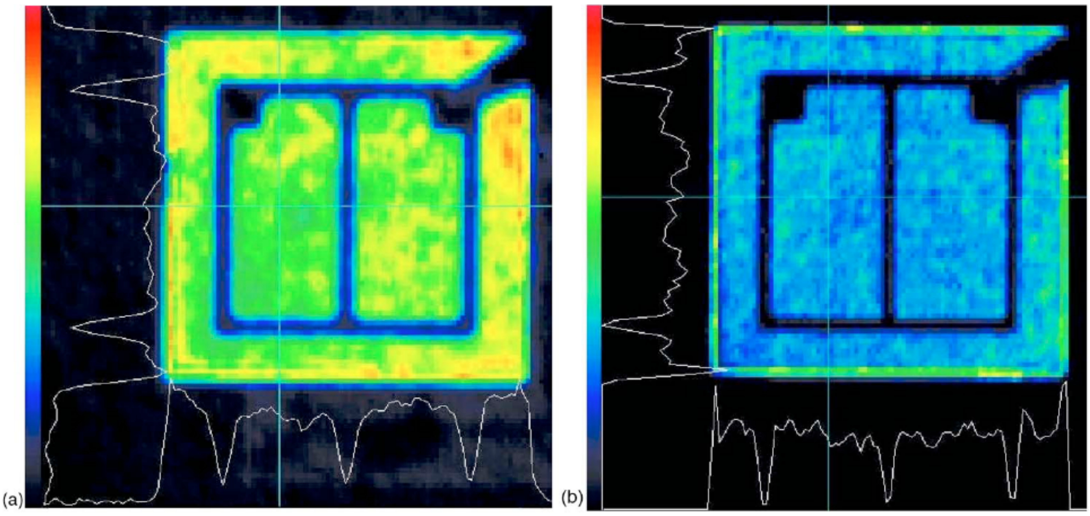

Figure 3.12 Intensity distribution of the GaN-based vertical-LEDs (a) with and (b) without a ZnO nanorod array omnidirectional extraction surface at a driving current of 200 mA.

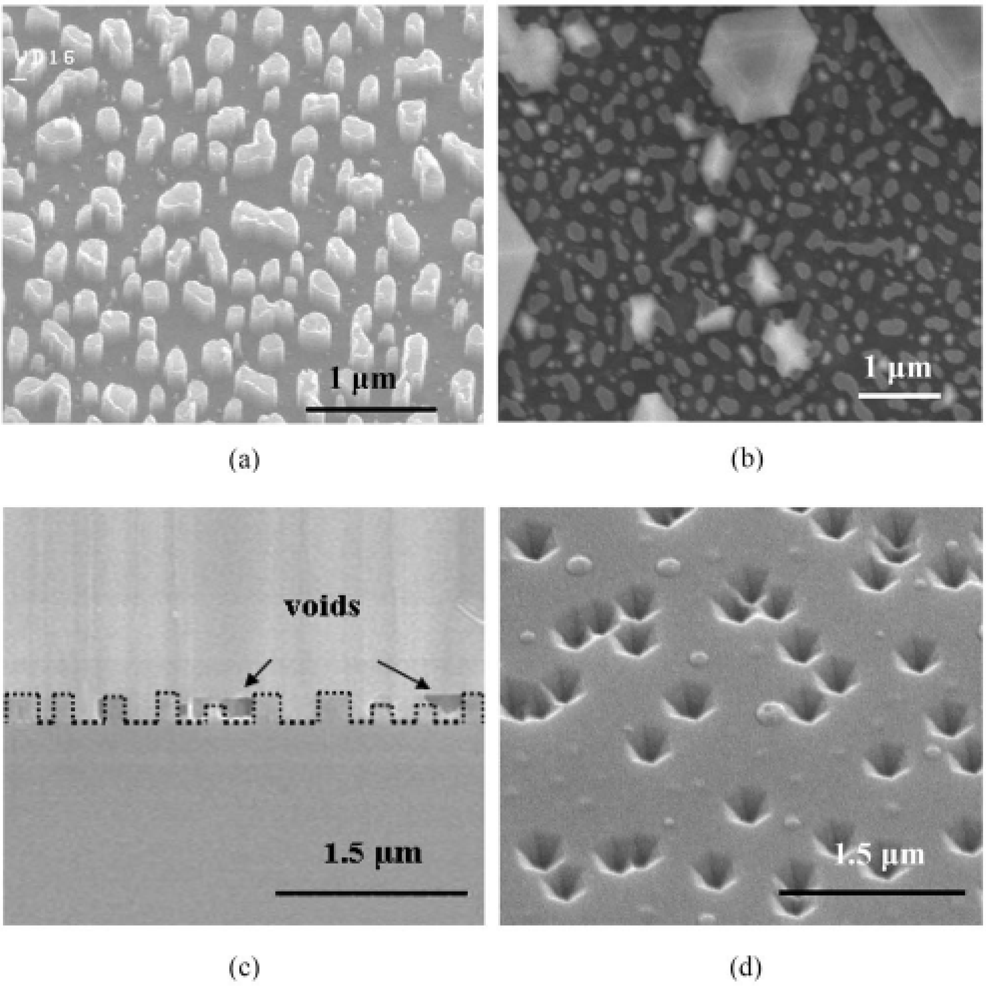

Figure 3.13 SEM images of (a) the fabricated SiO_2 nanorod array, (b) GaN nuclei on the SiO_2 NAPSS as growth seeds, (c) the GaN epilayer on a NAPSS in the cross-sectional view, and (d) the epitaxial pits on the *p*-GaN surface.

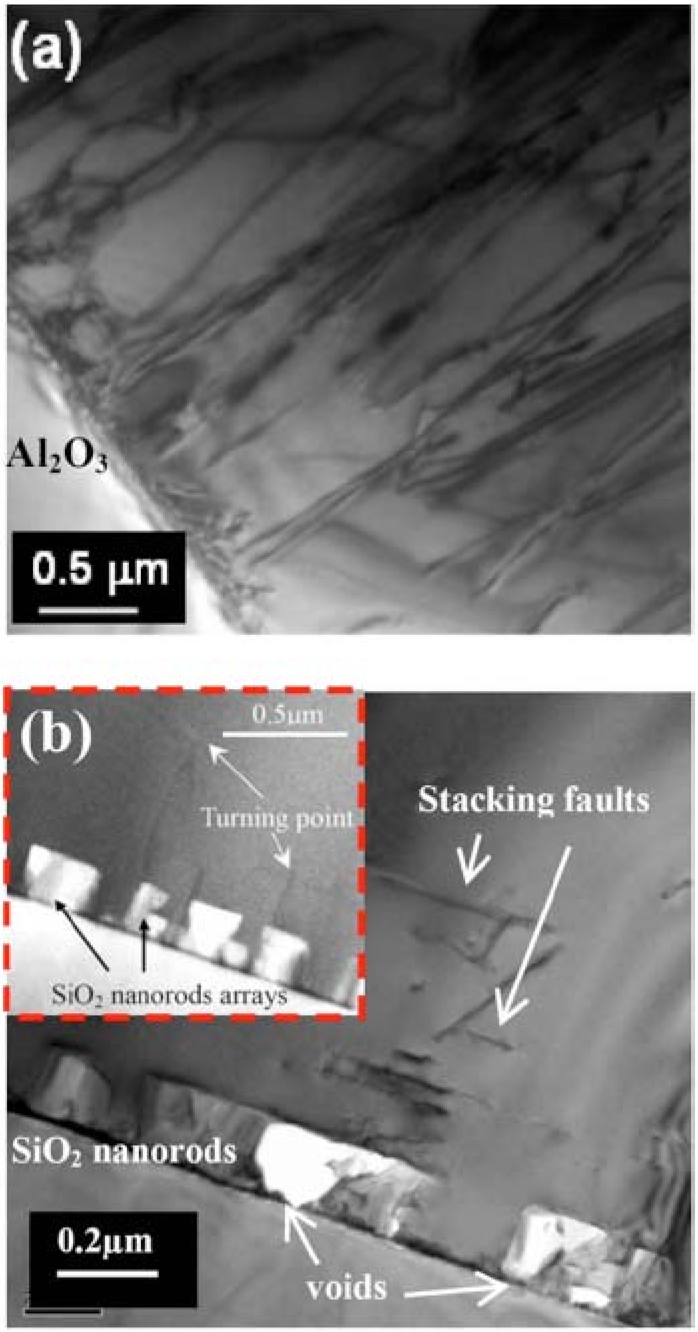

Figure 3.14 The TEM images of the GaN/sapphire interface for the GaN epilayer grown on (a) a planar sapphire substrate and (b) on a NAPSS. The inset of (b) shows the dislocation bending phenomenon with visible turning points.

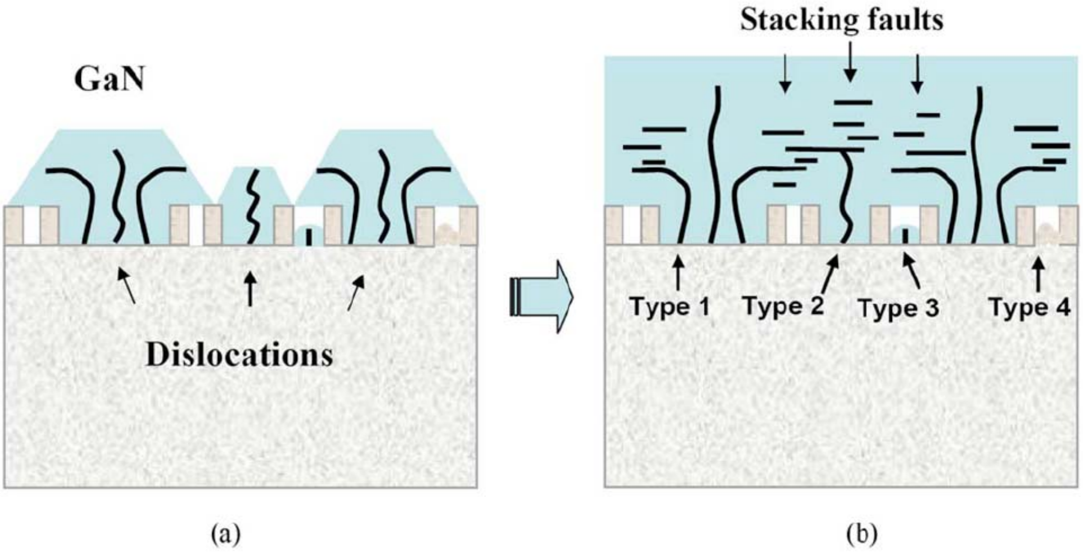

Figure 3.15 The schematics of (a) the overgrowth process and the formation of dislocations, stacking faults, and voids at the initial stage of epitaxy, and (b) four potential mechanisms accounted for the reduction of the TDD.

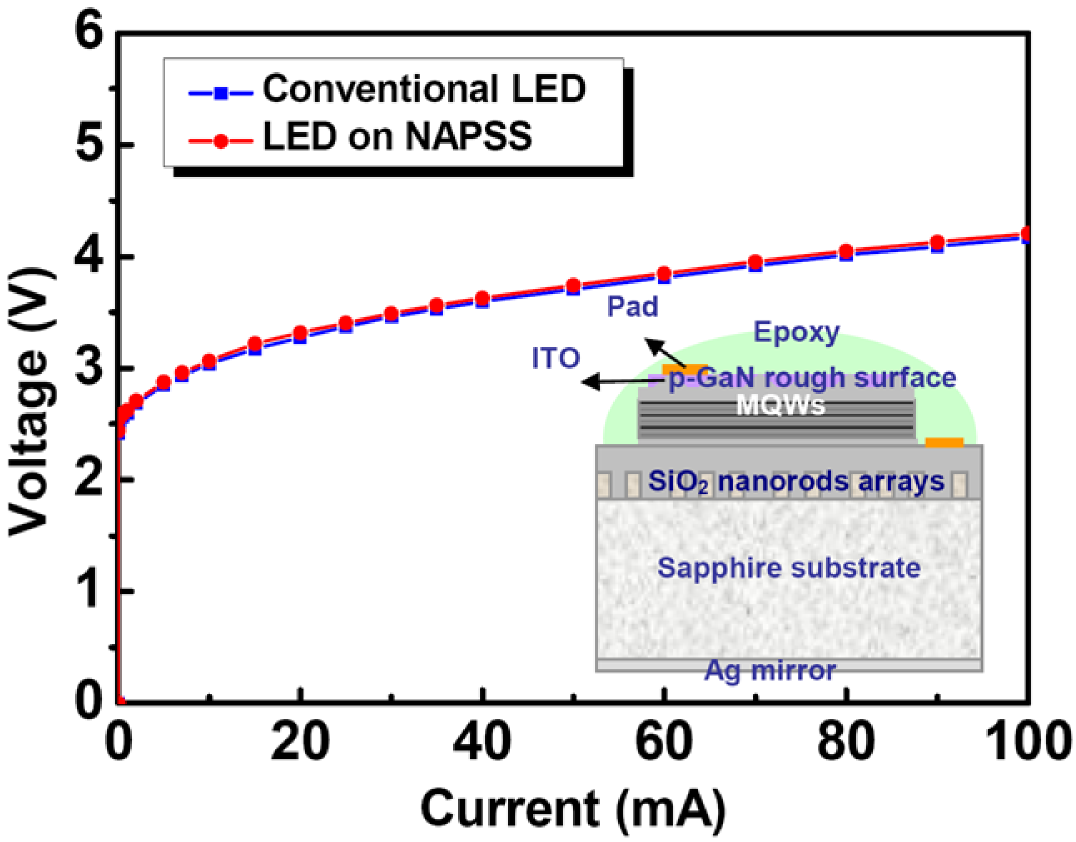

Figure 3.16 Current-voltage curves of a NAPSS and a conventional LED, where the inset shows a schematic of a NAPSS LED,

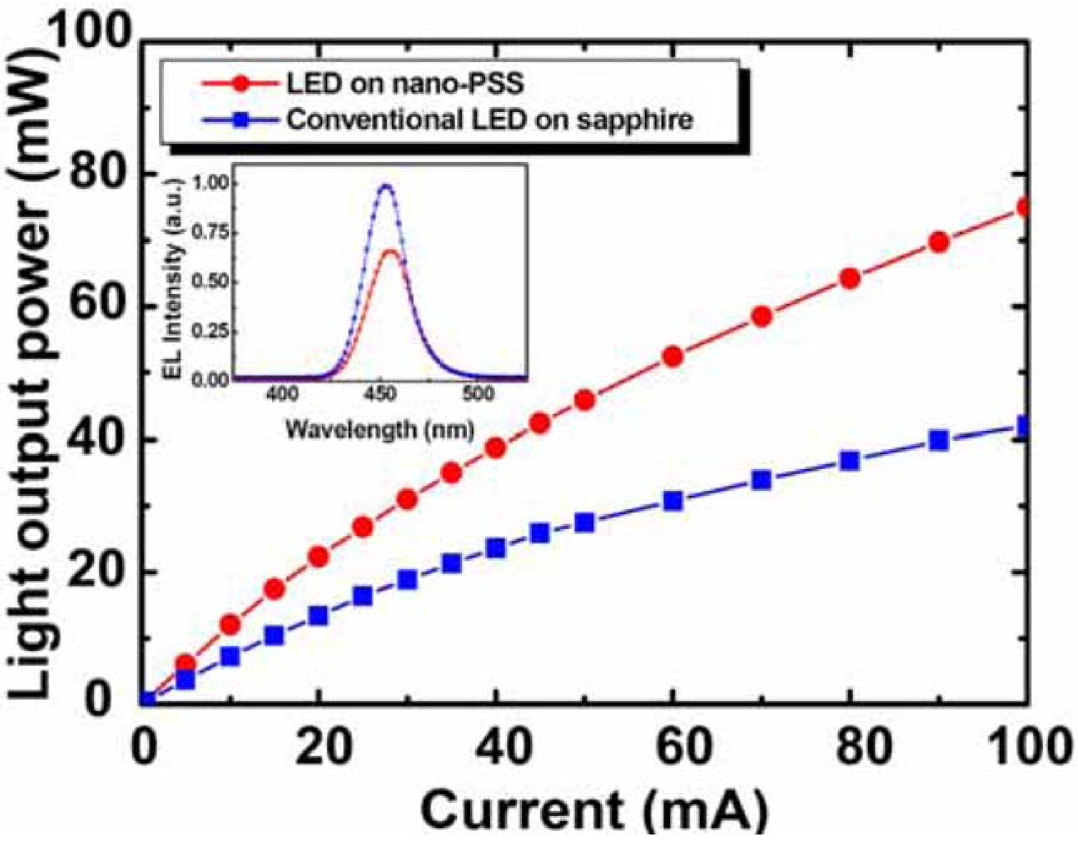

Figure 3.17 The current-output power curves, where the inset shows the electroluminescence spectra for both devices at a driving current of 20 mA.

CHAPTER 4

Improvement of Internal Quantum Efficiency by LED Grown on Patterned Sapphire Substrate

We had demonstrated several methods to improve the LED light extraction efficiencies by combining nano technologies. Nevertheless, the EQE, which was used to evaluate LED performance, was the product of IQE and ExE. That means, both IQE and ExE should be further improved for the next-generation high efficiency solid-state lighting system. Beside the methods we proposed in previous chapter, many methods regarding to ExE had been developed, such as surface roughening [1, 2], photonic crystal [3, 4], chip shaping [5], backside reflector [6], and so on. However, the study on improving IQE of III-nitride LEDs is relatively fewer. One of the reasons is the absent of a convincing approach to evaluate the IQE of LEDs. The general approach to evaluate the IQE of LEDs is to compare the PL intensity between low and room temperatures; however, the selection of pumping laser wavelength, power density and temperature would profoundly affect the measured results. Very recently, S Watanabe *et al.* had proposed a method to determine the IQE of LEDs by performing excitation power density and temperature dependent PL [7]. In comparison to the traditional measurement method, the proposed method is believed more accurate since the efficiency under different pumping density was considered. Based on their results, the variation of the IQE of InGaN/GaN LEDs with increasing excitation power at 11 K and 300 K was observed. Nevertheless, the reason for causing that variation was not clearly discovered. It is so important to understand the physical mechanisms of emission process that enables us to find out a guideline to improve the IQE.

In this chapter, we proposed a method to improve the IQE by growing GaN-based LEDs on patterned sapphire substrates (PSS), and investigated the physical mechanism behind by analyzing the emission energy, full-width at half maximum (FWHM) of the emission spectra and carrier recombination dynamic by time-resolved photoluminescence (TRPL) measurement.

4-1 Theory of IQE Measurement Method

We first note that the traditional method to define the IQE could be realized by figure 4.1. Generally, we used to perform a temperature dependent PL measurement and investigate the PL intensity variation curves with temperature. It is a non-destructive method to understand the internal material characteristics and quality. It provides useful information about emission wavelength, light intensity and other optical properties. During the experiment period, the intensity gradually reduced with the rising temperature. We could reasonably assume there are no non-radiative recombination at 0 K and the IQE approaches 1 which means one photon generated in the MQW while one laser photon was injected into the MQWs. In the meantime, we assume the ExE would not change with the increasing temperature. Therefore, the IQE could be defined as equation 4-1 by the traditional method:

$$\eta_{\text{int}}(T) = \frac{I(T)}{I(0)} \qquad (4\text{-}1)$$

where I(0) stands for the PL intensity at 0K and I(T) implies the PL intensity under specific temperature. We note that this method ignores the influence of injected laser power density which is not valid in blue GaN-based LED material system. Hence, we quote reference [7] to give a new definition by PL method. We performed the power-dependent PL measurement at low temperature and room temperature and define it by observing the tendency of the curves. This could be expressed as the following equation 4-2:

$$\eta_{PL} = C\frac{I_{PL}/E_{PL}}{I_{inj}/E_{inj}} \Rightarrow \eta_{\text{int}} \qquad (4\text{-}2)$$

where I_{PL} is the collected PL intensity; I_{inj} is the injected laser intensity; E_{PL} is the measured light photon energy; E_{inj} is injected photon energy and C is a constant which is related to carrier injection efficiency, light extraction efficiency and correction efficiency of PL.

While the injected laser power increased, the collected light intensity also increased. Generally, we could collect higher PL intensity at low temperature than that in room temperature. Therefore, the collected intensity versus the laser power at low temperature and room temperature could be depicted as figure 4.2 (a). We then can calculate the collected photons to be divided by the injected laser photons, by equation 4-2. A maximum number would be observed at some power of low temperature curve. After normalization to the peak, it could be shown as figure 4.2(b). Finally, we could define the IQE at room temperature at different laser power.

PL measurement setup

For excitation power and temperature dependent PL measurement, the laser source used in this research is femto-second-pulse Ti:sapphire. The output laser wavelength could be tuned to be around 760-820 nm by adjusting the internal resonant length and gain profile. A frequency doubler and tripler crystal is setup at the laser output optical path. Here, we adopted the doubler crystal to have a wavelength at around 380-410 nm could be obtained. It is specifically important in avoiding the absorption of GaN material itself and ensured most of the injected laser photons could excited the photons inside the MQWs. We note that this assumption essential while we predicted the injected carrier density. The tuned the 380-410 nm laser was then incident into the sample surface vertically. The sample was mounted in a closed-cycle He cryostate with a temperature controller which could be precisely controlled in the temperature region around 15 to 300 K. By the temperature controller with a set of wire heater, we could perform a serious of temperature-dependent experiments from 15 to 300 K. The luminescence signal dispersed through a 0.55-meter monochromator was detected by the photomultiplier tube (PMT). Not only optical properties like emission wavelength, intensity and FWHM were acquired, a time-resolved photoluminescence (TRPL) experiments could be performed simultaneously by setting a beam splitter to reflect part of light into a monochromator. It helps us to obtain the carrier lifetime from this lighting material. To sum up, we are able to realize the whole lighting mechanism by this PL measurement system. The setup detail of temperature dependent PL and TRPL are shown in figure 4.3.

<u>Sample preparation</u>

There are several types of the PSS arrangement like strip [8] or island-like [9] structures. Not only the effect of geometric light reflection issue was considered, the crystal quality after epi-process is also an important issue here. So, the designed patterns on sapphire substrate in this research are two dimensional hole-arrays arranged as hexagonal lattice with lattice constant of 7 μm and hole diameter of 3 μm. After the patterns were defined, the PSS samples were then undergone the ICP dry etching process to make the PSS. The SEM images of the fabricated PSS samples were shown in figure 4.4. The etched hole is 0.5-μm in depth and has triangular-shaped *C*-plane in the center, surrounded by three {1-102} *R*-plane facets. The fabrication details of PSS can be found elsewhere [9, 10]. The LED structure was then grown on planar substrate and PSS by low-pressure MOCVD. The LED structure consisted of a 30-nm-thick AlN nucleation layer, a 2-μm-thick Si-doped n-type GaN, and an unintentionally doped active layer with $In_xGa_{1-x}N$/GaN MQWs, and a 0.2-μm-thick Mg-doped p-type GaN. The doping concentration of n- and p-type GaN was nominally 5 x 10^{18} and 1 x 10^{19} cm^{-3}, respectively. The MQWs layers comprised 16 periods of an $In_{0.15}Ga_{0.85}N$ well (~2 nm) and a GaN barrier (~16 nm). On the purpose of comparison, a LED grown on flat sapphire with identical epi-structures was prepared.

4-2 Experiments

After the facility setup, we are then starting the optical experiments. A filter and a power meter were placed before sample chamber to modify and control the laser output power. By rotating the filter, we could vary the excitation power changing from 5x10^{-3} mW to 80 mW. We note in every PL measurement setup, the diameter of laser spot might have different spot size. Therefore, though we could plot the relationship between the injected power and the efficiency, it will be more convenient for comparison and reflect the influence of the carrier density more clearly, if we could transfer the power intro carrier density. To do that, we could follow the equation below to transfer our injected power to carrier density:

$$\text{Injected Carrier Density} = \frac{P}{(h\nu) * \phi * d_{active} * f} * \exp(-\alpha_{GaN} d_{GaN}) * \left[1 - \exp(-\alpha_{InGaN} d_{active})\right] * (1 - R) \tag{4-3}$$

The injected carrier density is determined primarily by the power of pumping laser (P), the energy of injected photon ($h\nu$), the spot size of pumping laser (ϕ), the thickness of GaN and active region (d_{GaN} ,d_{active}), the repetition rate of pumping laser (f), the absorption efficiency of GaN and InGaN (α_{GaN}, α_{InGaN}), and the reflectance of pumping laser (R), as expressed by the following equation. Experimentally, we choose ϕ = 50 μm, d_{GaN} = 200 nm, d_{active} =270 nm, α_{InGaN} =10^5 cm^{-1}, and R=0.17 to calculate the injected carrier density in our samples. Here we ignore the absorption of GaN since the energy of pumping photons is less than its energy bandgap,i.e. α_{GaN} =0. For the measurement of temperature dependent time-resolved PL (TRPL), the frequency doubled femto-second-pulse Ti:sapphire laser was operated on 390 nm with 2mW.

The repetition rate of the laser is 76 MHz whose time interval is 13 ns. The luminescence decay was measured with time correlated single photon counting (TCSPC) system in conjunction with a 0.55-meter monochromator. Time-resolution for the detection is about 4 ps.

4-3 Results and Discussion

We first performed the power-dependent PL measurement at 15 and 300 K and plot the efficiency curves of both PSS and reference samples in figure 4.5 after normalizing to its peak at low temperature. For the LED grown on planar sapphire substrate, one could clearly see that the IQE increases with injected carrier density to reach its maximum and decreases as the injected carrier density further increases. The tendency of two efficiency curves at 15 K and 300 K is quite similar. But under low injection carrier density range, the IQE at 300 K increases more pronounced than it at 15 K. Moreover, the corresponding density to the peak efficiency (~62%) in 300 K is at injected carrier density of about 10^{17} cm^{-3}, which is lager than it at 15 K, about 10^{16} cm^{-3}. A much larger variation of the IQE was observed over the injection carrier range at 300 K than 15 K.

For the LED grown on PSS, a similar dependence of the IQE on the injected carrier density was observed. However, in term of the peak efficiency (~70%) in 300 K at injected carrier density of 1x 10^{17} cm^{-3}, the IQE of LED grown on the PSS was enhanced by ~13%. It means that under the same injected power of pumping laser, there is about 13% enhancement for the converted photon carriers within the active region, as compared to the conventional LED structure grown on planar sapphire substrate. We believe the higher IQE for the LED grown on PSS is due to the better crystalline quality, attributed to the interaction between stack faults and threading dislocations, as studied in our previous work [9]. We now discuss the mechanism responsible for the dependence of IQE on the injected carrier density for both LEDs grown on planar sapphire substrate and PSS.

In general, the collected PL intensity, L, is proportional to the injected carrier density, I, with a power index P which could be expressed as [11, 12]

$$L \, \alpha \, I^{P} \qquad (4\text{-}4)$$

where parameter P physically reflects the various recombination processes. If P equals to 1, it indicates the radiative recombination dominates. On the other hand, if $P>1$, the Shockley-Read-Hall (SRH) recombination occurs, relating to the presence of nonradiative centers that provide a shunt path to the current. Figure 4.6 summarized the relationship between injected carrier density and the PL intensity for both LED grown on planar sapphire substrate (top one) and PSS (bottom one).

At 15 K for both samples, the intensity is linearly varied with excitation power density ($P = 1$), which indicates that the radiative recombination dominates the recombination process at all injected carrier density range and the nonradietive centers are quenched at low temperature. However, under low excitation power density at 300 K, the superlinear dependence of L on I are observed for both samples, showing that the defect related nonradiative recombination dominates in this low carrier injection range. But as injected carriers continuously increased, the linear dependence of the PL intensity to the injected carrier density is exhibited. It shall be noted here for both samples in 300 K, the value of P decreases to 1 gradually with the increasing of injected carrier density, instead of jump from

1.49 to 1 for PSS sample (or 2 to 1 for planar sample). It means the nonradiative centers are saturated and leads to the gradual suppression of the nonradiative recombination with the injected carrier density; therefore, the radiative recombination starts to dominate the recombination process, resulting in the pronounced increasing of the IQE, as shown in figure 4.5, for the region of injected carrier density less than 10^{17} cm^{-3}. In addition, since the LED grown on the planar sapphire substrate has higher threading dislocations than that grown on the PSS, the value of P in the superlinear zone is greater for the LED grown on planar sapphire substrate (P=2) than for the LED grown on PSS (P=1.49). Here we mainly focused on analyzing the transition process from the region dominated by nonradiative at low injection region to radiative recombination at high injection region. It should be noted that at an extremely high injection region, which is over 10^{18} cm^{-3}, another mechanism will be dominated to lower the efficiency which is called efficiency droop. This mechanism strongly deteriorates the device performance especially for the high current operating devices. More discussion at this efficiency droop phenomenon could be found in the next chapter.

To further study the mechanisms responsible for the variation of the IQE in figure 4.5, more optical properties were investigated as below. We first investigate these optical characteristics of both samples at low temperature. Figure 4.7 and 4.8 shows the emission peak energy and the FWHM of spectra as a function of the injected carrier density at 15 K for both LEDs grown on the planar sapphire substrate (figure 4.7) and the PSS (figure 4.8). Accompanied with the emission energy and FWHM, the corresponding carrier lifetime for both samples were also measured and provided in both figures for supporting the analysis of carrier dynamics.

In figure 4.7(a), for the LED grown on planar sapphire substrate in 15 K, several unique optical properties were observed. First, the emission peak energy gradually increases with the injected carrier density. Second, the FWHM of spectra shrinks when the injection carrier density ranging from 5 x 10^{13} cm^{-3} to 1 x 10^{16} cm^{-3}, and an opposite trend was observed as the injection carriers further increased. In general, there are two possible mechanisms for the blue-shift of emission energy with increasing injected carrier density. The first is coulomb screening of the quantum-confined Stark effect (QCSE). For the InGaN/GaN MQWs material, because the internal field direction is parallel to MQW growth direction, the device endures a strong QCSE. It caused a band tilting and a separation of wavefunction between electrons and holes, which resulting in a wavelength redshift and recombination efficiency reduction. On the other hand, the increasing of injected carrier density weakens the QCSE; that is what we called coulomb screening effect. Of course, an increasing of transition energy and efficiency should be observed if this effect dominates. Besides, as the screening effect dominates the emission process, it accompanied a reduction in FWHM. The second is band filling effect of localized states. That is an effect for carriers filled at a higher energy level while the injected carrier density increased continuously.

Due to indium composition inhomogeneity and monolayer thickness fluctuation of the InGaN MQWs, self-organized In-rich region is generated in InGaN active region, resulting in potential fluctuation of the energy bandgap [13-15]. Further increasing of injected carrier density, the filling effect of high energetic localized centers starts interfering and becomes dominated, that also induces a blue-shift of emission energy. However, unlike the effect of QCSE, this effect accompanies the broadening of FWHM. Clearly, we can conclude that in the region of injected carrier density from ~5 x 10^{13} cm^{-3} to ~1 x 10^{16} cm^{-3}, the gradual increase of emission energy and shrink of FWHM for the LED grown on planar sapphire substrate is mainly due to the coulomb screening of the QCSE, and that increases the overlap probability of wavefunction of electron and hole. Therefore, in the same region of injected carrier density (~5 x 10^{13} cm^{-3} to ~1 x 10^{16} cm^{-3}), its IQE also gradually increases, as shown in figure 4.5 (open square). As the injected carrier density is further increased (> 1 x 10^{16} cm^{-3}), band filling of localized states starts interfering and becomes dominated; the effect prompts the injected carriers to escape more easily from localized states. As a result, the IQE was further deteriorated with the injected carrier density larger than 1 x 10^{16} cm^{-3}.

In figure 4.7(b), we observed the gradually reduced carrier lifetime with the increasing of the injected carrier density. The decreasing of carrier lifetime with increasing injected carrier density could be attributed to the coulomb screening of internal electric in InGaN MQWs [16]. As injected carrier density in the QW increases, more excited carriers can screen the built-in electric field in QW, and that animates the recombination of electron-hole pair. As a result, the carrier recombination rate was accelerated, leading to a decrement of carrier lifetime. For higher injection carrier density (> 1 x 10^{16} cm^{-3}), we observe that the carrier lifetime keep decreasing, but a saturated tendency as injected carrier density higher than 2 x 10^{17} cm^{-3}. That is mainly due to the fact that the carrier at higher state by band filling effect would have shorter lifetime. And as long as these higher energy states were fully occupied, the corresponding carrier lifetime of emitted photon shall keep constant, even with further injection of carrier density. Here it is clear that our measurement of carrier lifetime well agrees with the shift of main emission peak.

As for the LED grown on the PSS in 15 K (figure 4.7(a)), basically we can adopt the same carrier dynamics to clarify the dependence of emission peak energy and the FWHM on the injected carrier density. However, in the bottom of figure 4.8(b), we observe that under exactly the same injected carrier density, the carrier lifetime of the LED grown on the PSS is around 10ns longer than that of the LED grown on the planar sapphire substrate. We believe it is due to the fewer threading dislocations in the LED grown on the PSS. In general, the nonradiative recombination rate is much quicker than the radiative recombination rate, and more nonradiative centers were expected in the LED grown on the planar sapphire substrate. Therefore, in term of the carrier lifetime of emitted photon, the LED grown on the PSS shall have longer carrier lifetime than that grown on the planar sapphire substrate. It is also consistent with the evaluation of the IQE in figure 4.5, as one can observe the higher efficiency value on the LED grown on the PSS than that grown on the planar sapphire substrate in 15 K.

To further examine the mechanism responsible for the tendency of the IQE in 300 K, we perform the similar analysis for both LED devices. For the LED grown on the planar sapphire substrate as shown in figure 4.9, we could divide three parts of this curve for discussion. At first glance, the tendency in region of the injected carrier density from ~5 x 10^{15} cm^{-3} to ~7 x 10^{17} cm^{-3} in figure 4.9, that is very similar to it at 15 K. Moreover, as compared to the top of Fig. 3 (solid square, 300 K), the parameter P in this region equals to 1, indicating the radiative recombination dominates. Therefore, the physical mechanisms of this region can be classified to two stages. First is preliminary dominated coulomb screening of the QCSE and then the subsequent interfering of band filling effect of localized states.

However, for the initial case of the region with the injected carrier density from 1 x 10^{14} cm^{-3} to 1 x 10^{15} cm^{-3}, different phenomenon was observed. First, in contrast to the results measured at 15 K as shown in figure 4.7, the emission energy shows the red-shift and the FWHM broadens with increasing injected carrier density. Second, the parameter P in this region equals to 2, indicating the nonradiative recombination dominates the carrier recombination process. Third, as compared to figure 4.7, it can be found the emission energy at 300 K under low injected carrier density is higher than it at 15 K, which shows that the carriers recombined at higher energy states at 300K under low injected carrier density condition. Finally, in figure 4.9(b), the carrier lifetime increases to the maximum of ~45 ns with the injected carrier density from 1 x 10^{14} cm^{-3} to 1 x 10^{15} cm^{-3}, and remains unchanged from 1 x 10^{15} cm^{-3} to 5 x 10^{15} cm^{-3}.As further increase the injected carrier density (>5 x 10^{15} cm^{-3}), the corresponding carrier lifetime droops gradually.

To summarize the different phenomenon mentioned above, at lowest injected carrier density, due to nonradiative process dominates the carrier recombination process (P=2), the carrier lifetime is shortened, and that prompts excited carriers to recombine at higher energy extended states before reaching into lower energy localized states [17]. Thus as compared to the recombination in low energy localized state in 15 K, the transition of these higher energy extended states would emit higher photon energy. Since there may exist many of higher energy extended states, this kind of recombination would accompany by the broadening of FWHM. Moreover, with the increasing of the injected carrier density from 1 x 10^{14} cm^{-3} to 1 x 10^{15} cm^{-3}, the nonradiative recombination was gradually bleached out and, on the contrary, the radiative process comes to be dominating. Hence an increment of lifetime was observed in this region (figure 4.9(b)). Once the carrier lifetime increases, the excited carriers can transfer from higher extended states to lower localized states, and accompanied with the red-shift of emission energy. As a result, in the region of injected carrier density from 1 x 10^{14} cm^{-3} to 1 x 10^{15} cm^{-3} in 300 K, we can expect the higher emission energy than that in 15 K, the red-shift of emission energy, the broadening of the FWHM, and the increasing of the carrier lifetime. For the region of the injected carrier density from 1 x 10^{15} cm^{-3} to 5 x 10^{15} cm^{-3}, it could be seemed as a quasi-equilibrium state of the injected carriers, thus an unchanged of carrier lifetime was observed. After that (> 5 x 10^{15} cm^{-3}), similar phenomenon as we discussed in figure 4.7 was observed. Therefore, we could conclude that for the LED grown on the planar sapphire substrate, the main mechanism for causing the difference between the IQE curves in 15 K and 300 K is the thermal activated nonradiative centers especially at the stage of low injected carrier density. The majority of injected carrier was exhausted by the nonradiative centers and fails to effectively screen the QCSE resulting in low IQE at 300 K.

In figure 4.10(a), we show the emission energy and the FWHM as function of injected power density at 300 K for the LED grown on the PSS. The corresponding carrier lifetime for the sample is also shown in figure 4.10(b). As compared to the sample LED measured in 15 K (Fig. 4b), for the injected carrier density from 1 x 10^{14} cm^{-3} to 1 x 10^{15} cm^{-3}, we can observe the higher emission energy, the red-shift of emission energy, and the increasing of the carrier lifetime, and that is similar to the previous analysis for the LED grown on the planar sapphire substrate. However, we do not observe the broadening of the FWHM in this region. We believe it is due to the fewer threading dislocations existing in the LED grown the PSS, and thus reduces the transition from higher energy extended states. For the inject carrier density from 1 x 10^{15} cm^{-3} to 5 x 10^{15} cm^{-3}, we also observe the unchanged of the carrier lifetime; however, its maximum carrier lifetime of ~60 ns is longer than that of the LED grown on the planar sapphire substrate(~45 ns). It means fewer nonradiative centers would interfere and affect the transition of injected carriers, and that is well consistent with the experimental observation of FWHM. Again, for the injected carrier density larger than 5 x 10^{15} cm^{-3}, the radiative recombination becomes dominated (P=1), and that would lead to the preliminary coulomb screening of the QCSE and the subsequent band filling effect of localized states as we mentioned before.

Finally, we would like comment briefly on the origin of higher IQE for the LED grown on the PSS. All the information provided above is the summary and comparison of both samples at 15 and 300 K. Here, we collected the temperature dependent PL intensity and plot the normalized intensity with inversed temperature which is understood as Arrhenius plot in figure 4.11. Then, this temperature dependent curve could be fitted by the following equation to get the activation energy:

$$I_T = I_0 / [1 + A\exp(-E_a / kT) + B\exp(-E_b / kT)] \tag{4-5}$$

where I_T, I_0 are the integrated PL intensity for T and 0 K, A and B are constants, k is the Boltzmann constant, T is the temperature, E_a is the activation energy for PL quenching, and E_b is generally associated to the free exciton binding energy [18]. The fit activation energy for the LED grown on the planar sapphire substrate and the PSS are 32.4 meV and 61.7 meV, respectively. In general, the activation energy can be explained by the ability to confine the carriers within the potential minima. One could understand it by the schematic of activation energy in figure 4.12. In InGaN material system, because the In inhomogeneous, there are a large In fluctuation and a various localization states. The average of this localization could be quantized as an effective localized state. On the other hand, because of a large density of dislocation which results in a nonradiative recombination, we could also summarize this state as a effective defect state. The difference between these two states could be viewed as the activation energy. Besides, one could also realize it as energy to enable a confined electron trapped in the localized state escaping from it. Thus the higher value of the activation energy indicates the stronger confinement of injected carriers and that certainly promises the higher IQE.

In addition to the fitted activation energy from the temperature dependent PL experiments, similar evidence could be found in the comparison of emission wavelength. We compared the emission wavelength and energy of samples grown on PSS and flat sapphire substrate as shown in figure 4.13(a) and (b). As the injected carrier density increased, the emission wavelength continuously increased in both samples. Nevertheless, if we focus on comparing the wavelength difference between carrier density of 1x10^{18} cm^{-3} and 10^{17} cm^{-3}, PSS has a larger wavelength difference, 5.75 nm, than that of flat sample, 5 nm, at low temperature. Similarly, the difference is 3.54 nm for PSS sample and 5.9 nm for flat sample at room temperature. As we understood, the high injection period is dominated by band filling effect; the larger wavelength shift implies the samples could endure a larger carrier density but still effectively recombination. These observations provide evidence that the PSS do benefit for a better crystal quality and improve the IQE performance.

Reference:

[1] Y. J. Lee, H. C. Kuo, S. C. Wang, T. C. Hsu, M. H. Hsieh, M. J. Jou, and B. J. Lee, IEEE Photonic Technology Letter **17**, 2289 (2005).

[2] T. Fujii, Y. Gao, R. Sharma, E. L. Hu, S. P. DenBaars, and S. Nakamura, Applied Physics Letter **84**, 855 (2004).

[3] S. Fan, P.R. Villeneuve, J.D. Joannopoulos, and E.F. Schubert, Physics Review Letter **78,** 3294 (1997).

[4] T. N. Oder, K. H. Kim, J. Y. Lin, and H. X. Jiang, Applied Physics Letter **84**, 466 (2004).

[5] C. C. Kao, H. C. Kuo, H. W. Huang, J. T. Chu, Y. C. Peng, Y. L. Hsieh, C. Y. Luo, S. C. Wang, C.C. Yu and C. F. Lin, IEEE Photonics Technology Letters **17,** 19 (2005).

[6] Y. J. Lee, J.M.Hwang, T. C. Hsu, M. H. Hsieh, M. J. Jou, B. J. Lee, T.C. Lu, H.C. Kuo, and S.C. Wang, EEE Photonic Technology Letter **18,** 724 (2006).

[7] S. Watanabe, N. Yamada, M. Nagashima, Y. Ueki, C. Sasaki, Y. Yamada, T. Taguchi, K. Tadatomo, H. Okagawa, and H. Kudo, Applied Physics Letter **83**, 4906 (2003).

[8] C. Netzel, T. Wernicke, U. Zeimer, F. Brunnera, M. Weyers, M. Kneissl, Journal of Crystal Growth **310**, 8 (2008)

[9] Y. J. Lee, T.C. Lu, H.C. Kuo, S.C. Wang, K. W. Ng, K. M. Lau, Z. P. Yang, Allan S.P. Chang, and S. Y. Lin, IEEE Journal of Lightwave Technology **26**, 1455 (2008).

[10] Y. J. Lee, J.M. Hwang, T. C. Hsu, M. H. Hsieh, M. J. Jou, B. J. Lee, T.C. Lu, H.C. Kuo, and S.C. Wang, IEEE Photonic Technology Letter **18**, 1152 (2006) .

[11] I. Ma'rtil, E. Redondo, and A. Ojeda, Journal of Applied Physics **81,** 2442 (1997).

[12] X. A. Cao, E. B. Stokes, P. M. Sandvik,, S. F. LeBoeuf, J. Kretchmer, and D. Walker, IEEE Electronic Device Letter **23**, 535 (2002).

[13] S. Chichibu, T. Sota, K. Wada, and S. Nakamura, Journal of Vacuum Science and Technology B **16**, 2204 (1998).

[14] T. Wang, D. Nakagawa, J. Wang, T. Sugahara, and S. Sakai, Applied Physics Letter**73,**

3571 (2007).

[15] T. Kuroda, and A. Tackeuchi, Journal of Applied Physics **92,** 3071 (2002).

[16] Y. Narukawa, S. Saijou, Y. Kawakami, S. Fujita, T. Mukai, and S. Nakamura, Applied Physics Letter **74**, 558 (1999).

[17] Y. H. Cho, G. H. Gainer, A. J. Fischer, J. J. Song, S. Keller, U. K. Mishra, and S. P. DenBaars, Applied Physics Letter **73**, 1370 (1998).

[18] C. C. Yu, C. F. Chu, J. Y. Tsai, C. F. Lin and S. C. Wang, Journal of Applied Physics **92,** 1881 (2002)

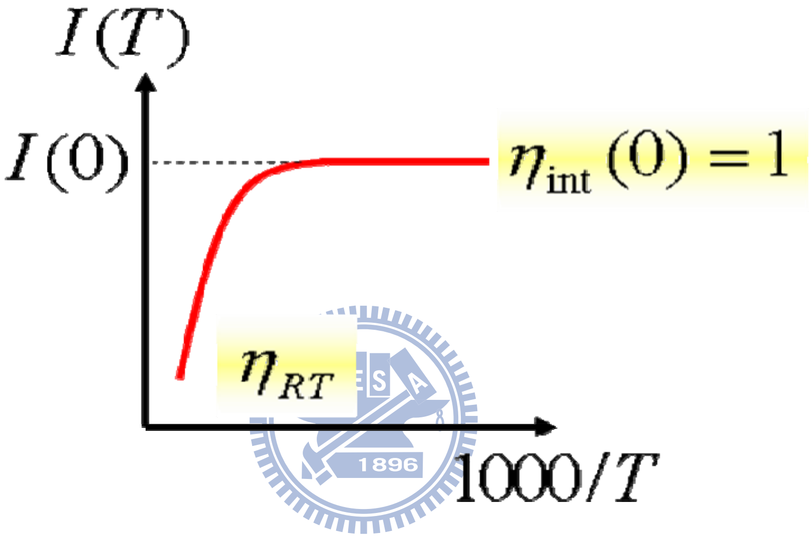

Figure 4.1 The temperature dependent IQE curves

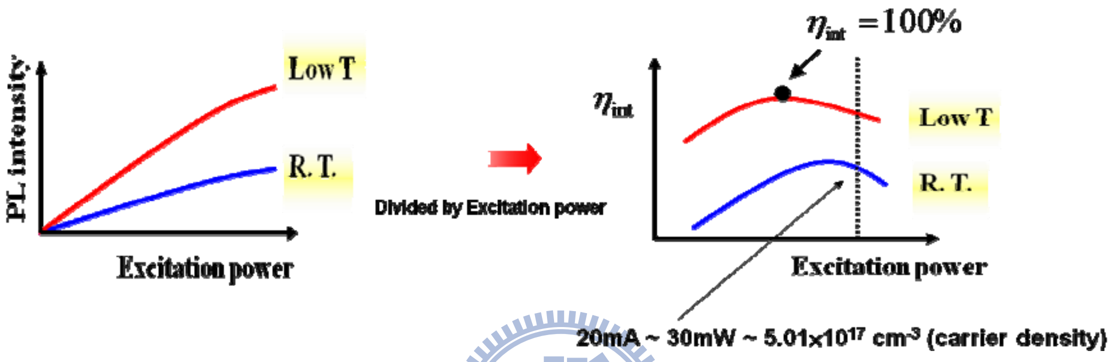

(a) (b)

Figure 4.2 (a) the collected intensity versus the laser power at low temperature and room temperature and (b) the curves after normalization

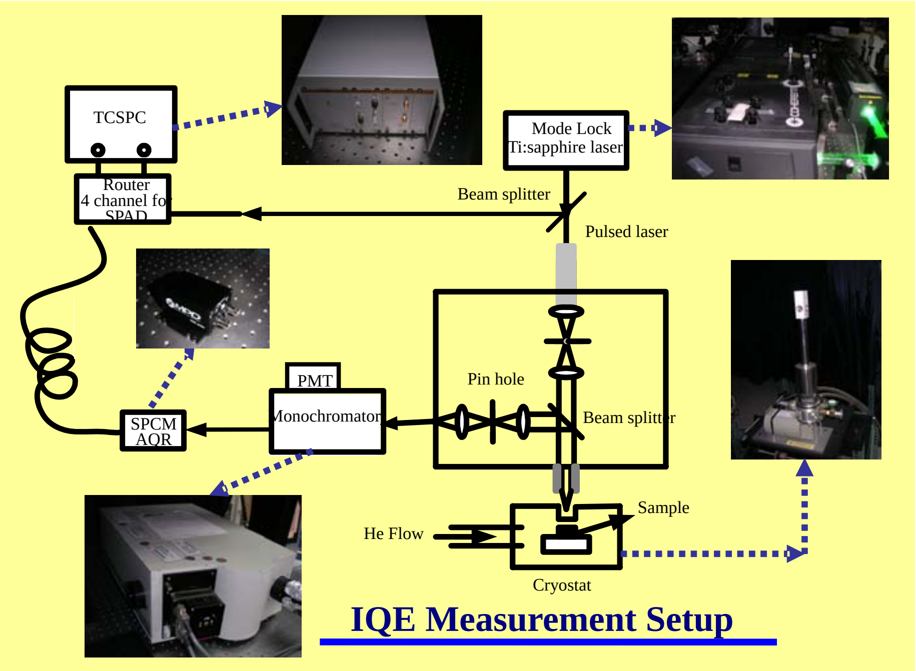

Figure 4.3 The setup detail of temperature dependent PL and TRPL

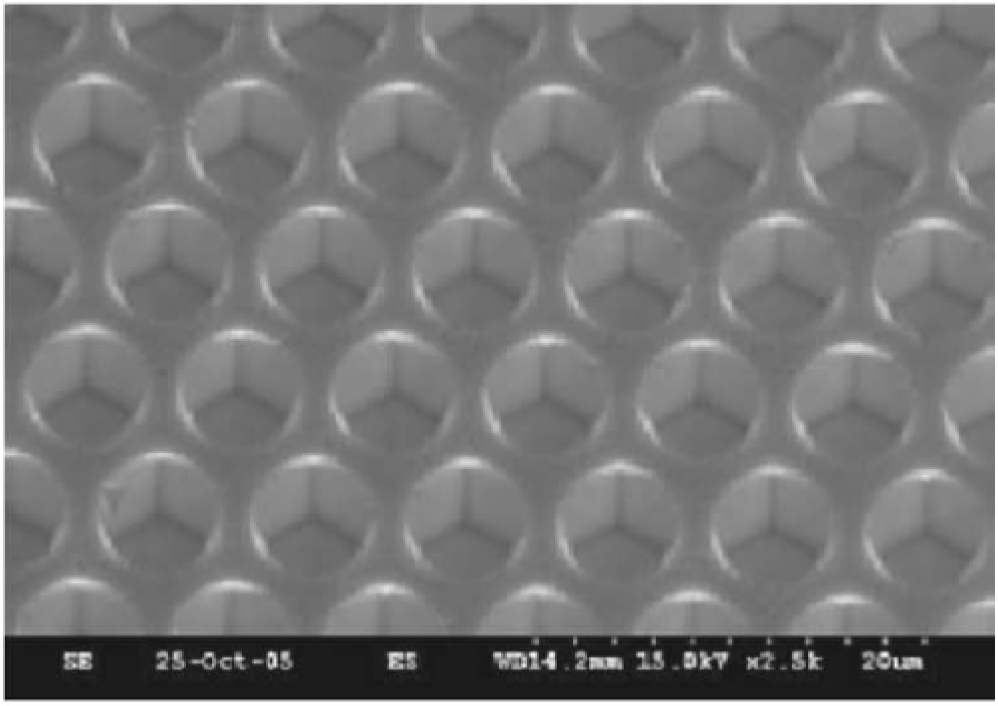

Figure 4.4 SEM images of PSS used in this research

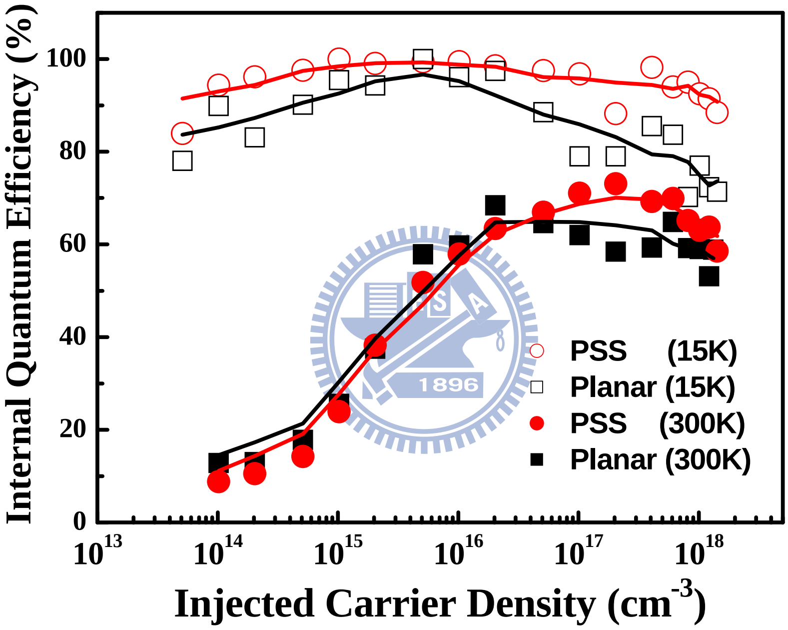

Figure 4.5 The power-dependent PL efficiency curves of PSS and reference samples at 15 and 300 K

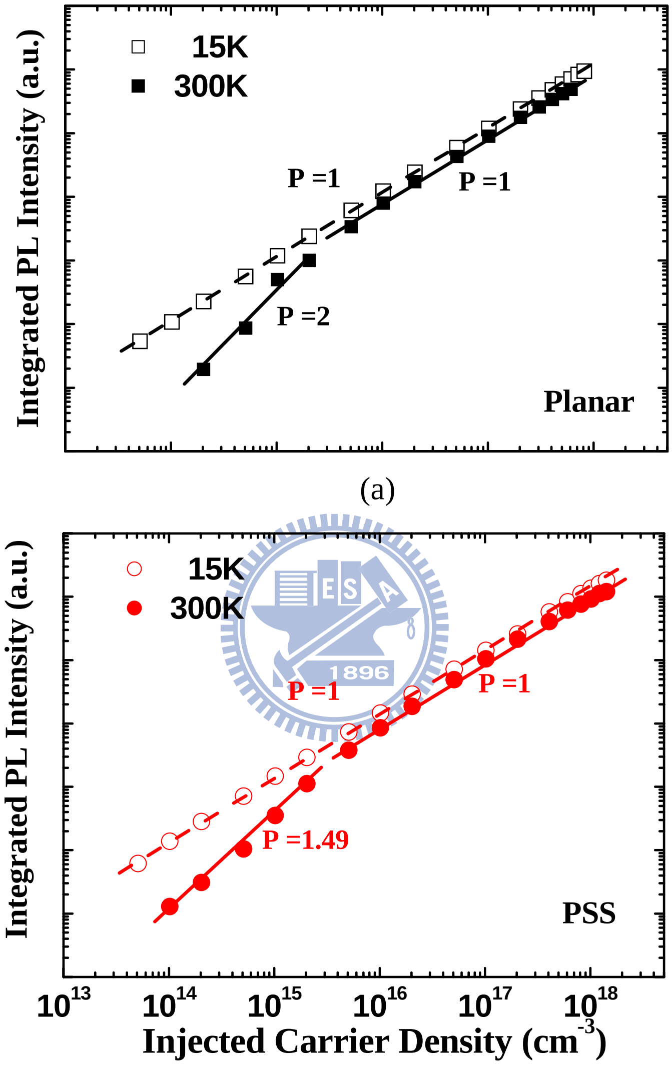

(a)

(b)

Figure 4.6 The curves of integrated PL intensity versus the injected carrier density of (a) planar and (b) PSS samples

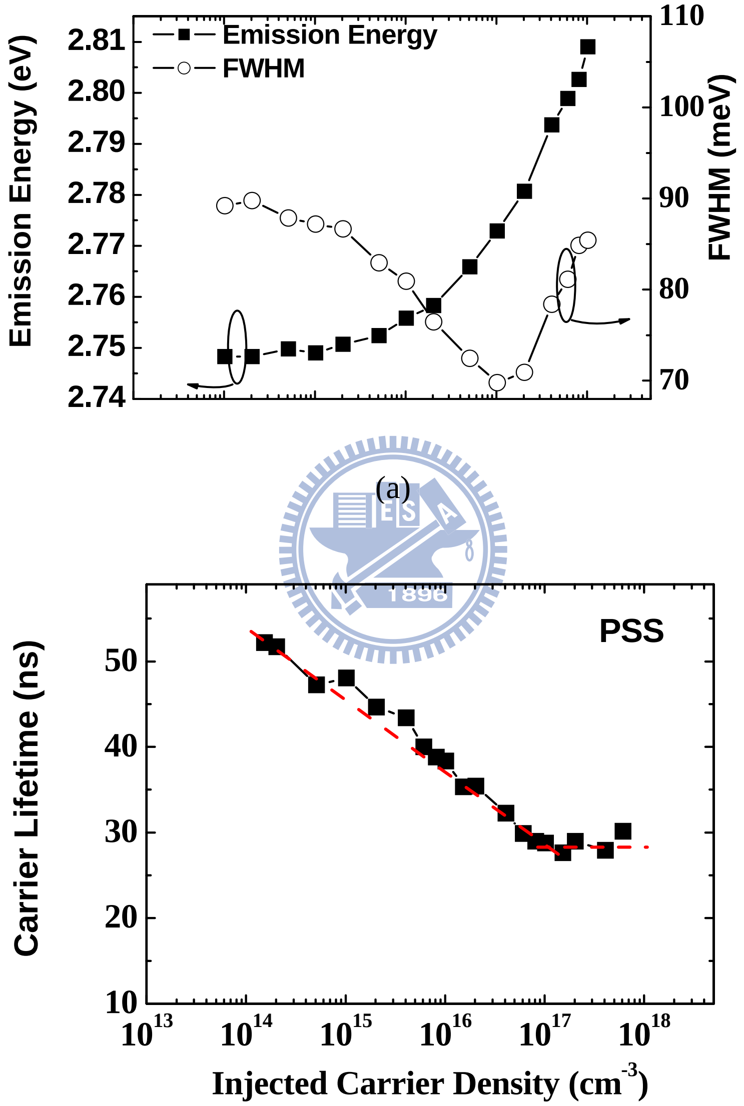

(a)

(b)

Figure 4.7 (a) The emission peak energy and the FWHM of spectra and (b) carrier lifetime, as a function of the injected carrier density at 15 K for LEDs grown on the planar sapphire substrate

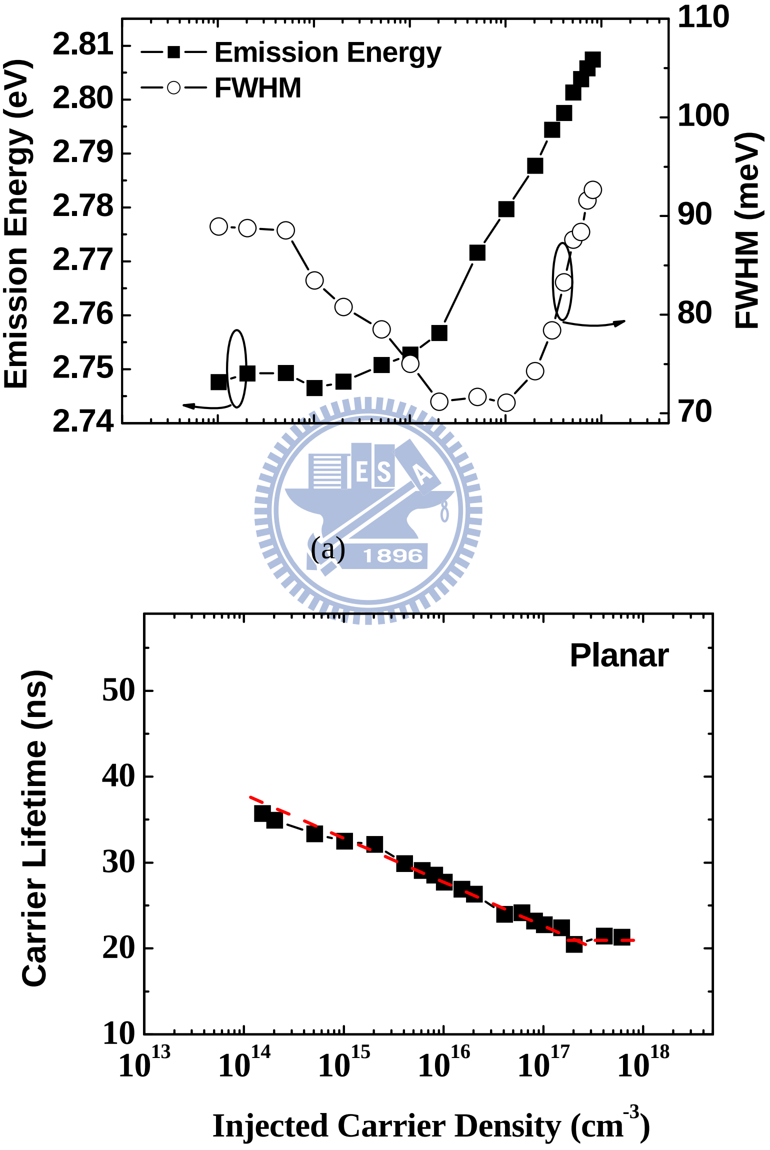

(a)

(b)

Figure 4.8 (a) The emission peak energy and the FWHM of spectra and (b) carrier lifetime, as a function of the injected carrier density at 15 K for LEDs grown on planar sapphire substrate

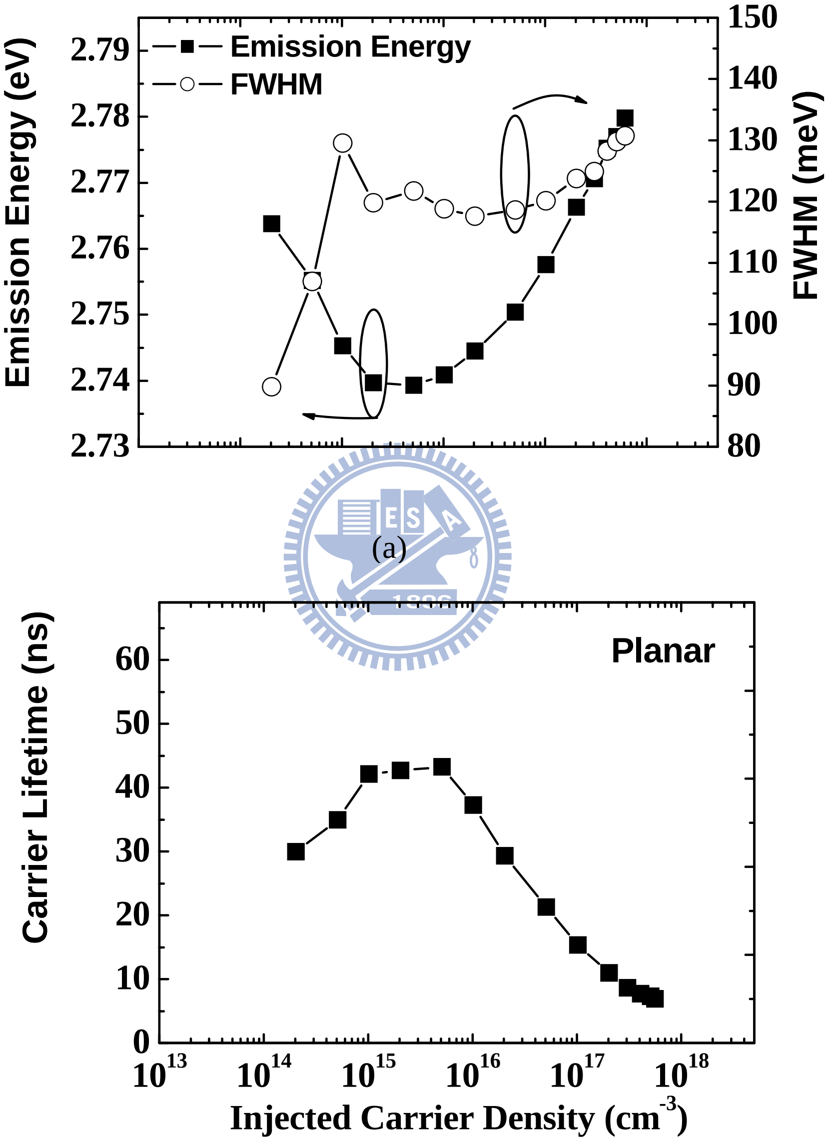

(a)

(b)

Figure 4.9 The emission peak energy and the FWHM of spectra and (b) carrier lifetime, as a function of the injected carrier density at 300 K for LEDs grown on planar sapphire substrate

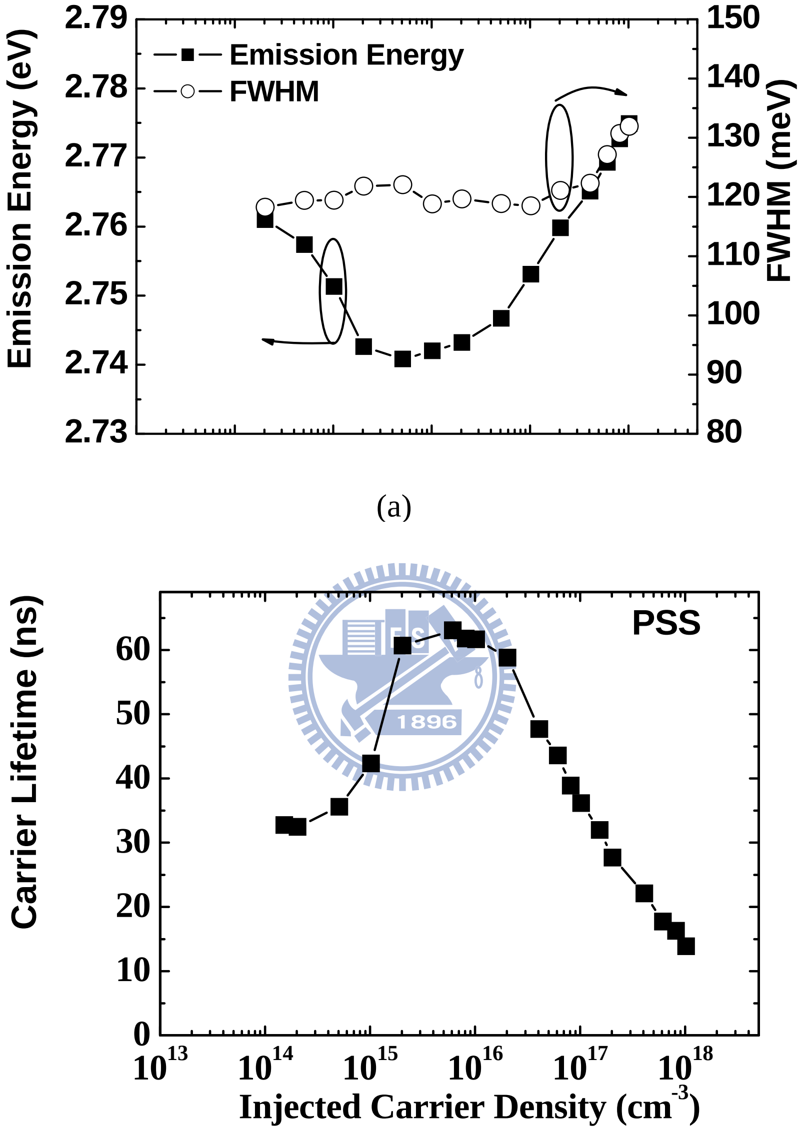

(a)

(b)

Figure 4.10 (a) The emission peak energy and the FWHM of spectra and (b) carrier lifetime, as a function of the injected carrier density at 15 K for LEDs grown on the patterned sapphire substrate

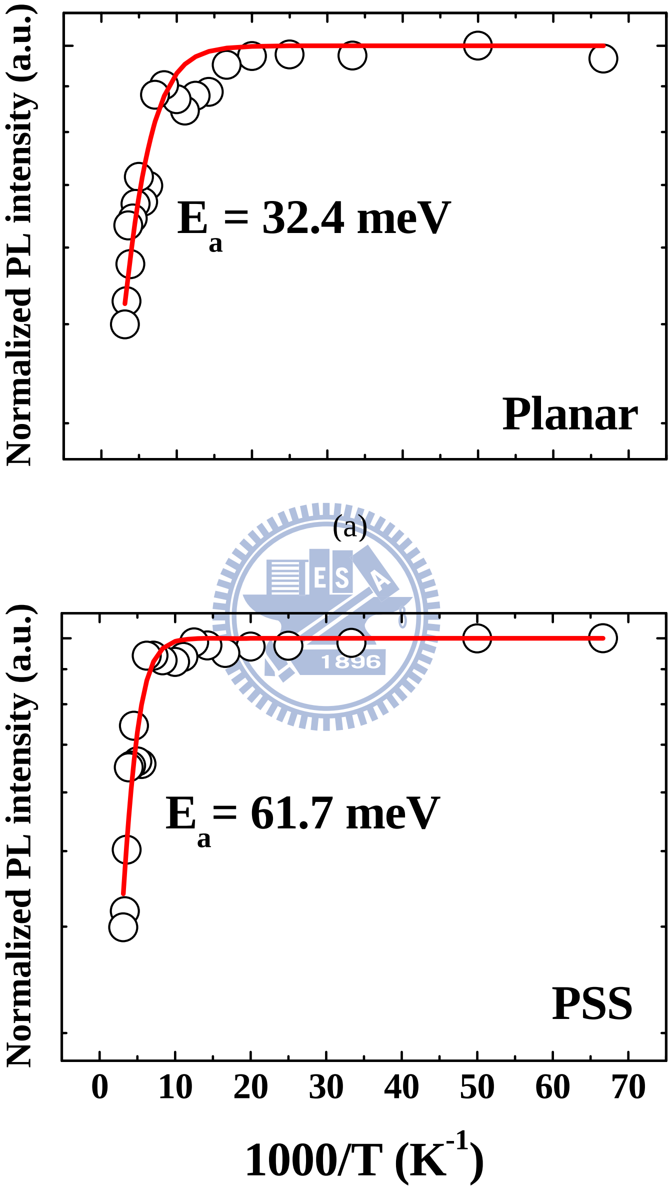

(a)

(b)

Figure 4.11Normalized integrated PL intensity as a function of 1/*T* for LEDs grown on the planar sapphire substrate (top) and the PSS (bottom). The activation energy is obtained from the Arrhenius plot.

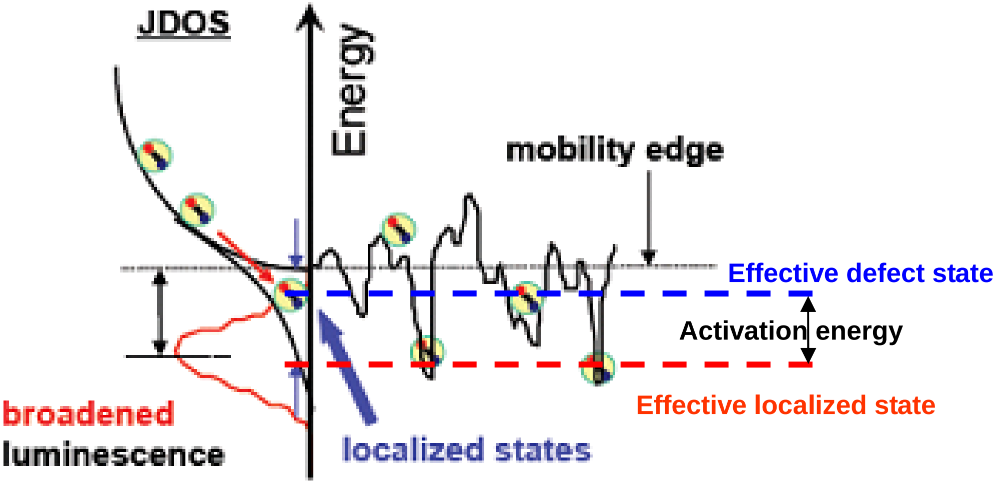

Figure 4.12 Schematic drawing of effective localized states, defect states and activation energy

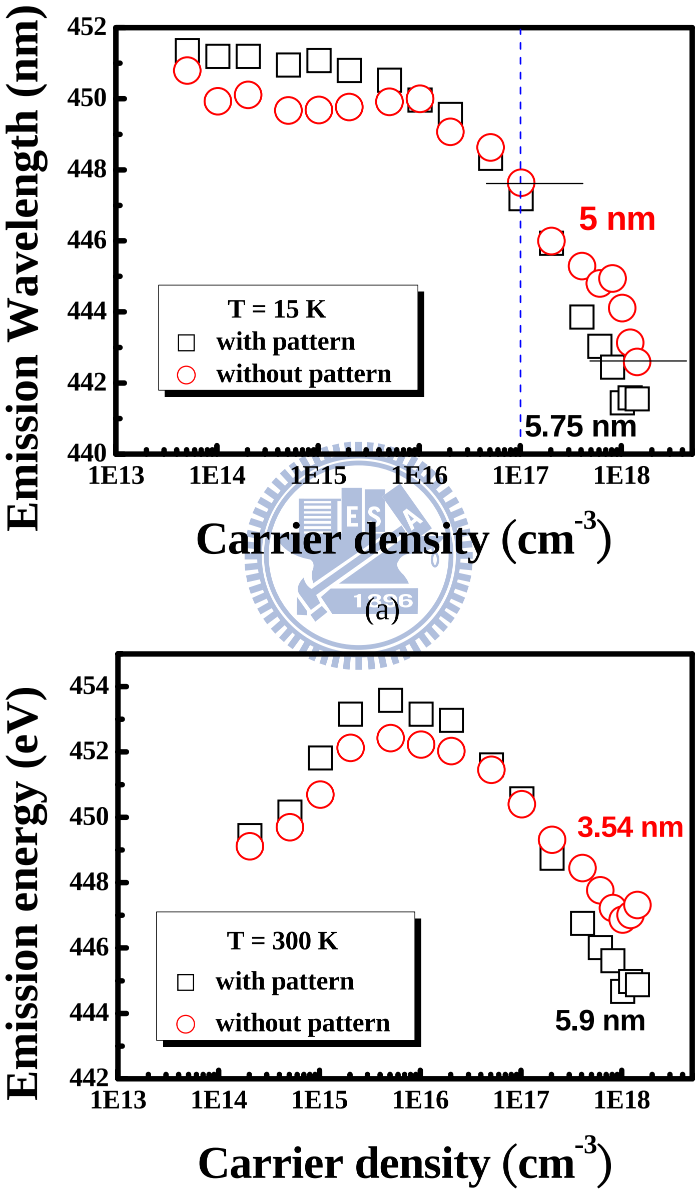

(a)

(b)

Figure 4.13 The emission wavelength and energy of samples grown on PSS and flat sapphire substrate under different carrier density

CHAPTER 5

Electroluminescence and Efficiency Droop Analysis of LED Grown on Patterned Sapphire Substrate

Recently some research groups have investigated temperature dependence of the electroluminescence (EL) spectral intensity [1-3], which reveals anomalous EL quenching at lower temperatures below 100 K. It is found that the anomalous temperature dependence of the EL efficiency is caused by interplay of the carrier capture and the IQE. One interesting observation of the InGaN/GaN QW diodes so far is, in contrast to PL performance, the EL efficiency dramatically decreases when the diode temperature is decreased below 100 K, where the improved EL efficiency is generally expected due to the decreased nonradiative recombination processes. One of the anticipated genuine causes for the low temperature EL quenching may be ascribed to the deep Mg acceptor level of 170 meV in p-GaN [4], which might be deactivated at lower temperatures below 100 K. Therefore, holes are failed to be injected into the MQWs active region from the p-GaN layer, especially when the electron blocking p-type AlGaN barrier is introduced near p-GaN side. In this chapter, we performed a temperature dependent EL measurement to realize device performance under different temperature condition. The details of physical mechanisms for the EL and efficiency droop-related characteristics were studied. Besides, a simulation software, Advanced Physical Models Semiconductor Devices (APSYS) was used and an electric model was established to investigate the carrier transport inside the LED structure. The details of the LED structure, temperature-dependent EL measurement, simulation and modeling will be discussed in this chapter.

5-1 Temperature Dependent EL Measurement Instrument

In this EL measurement system, the used current source is Kiethley 238. The best measurement resolution at 1 nA injection could reach 10 fA with a accuracy of 0.3%. We could also perform a serious of current-voltage measurement and data storage by LabView human-machine control interface. A zoom microscope is used to observe the patterned electrode which enabled us locating the probe to pads. For blue GaN-based LED device, because of the isolated substrate, usually there are two pads on top which means at least two isolated probes is necessary. Therefore, two set of isolated three axial stages with probes were employed for current injection. Once we could successfully inject the current into device, the next problem is how we collect the emitted light. Traditionally, we used to collect the light by a lens set and coupled into a fiber connected to a spectrum meter. However, due to the requirement of large space for manipulating the two probes, collecting emitted light by lens set is allowed here. So, we adopted the method to build in a third tree axial stage with a 200 μm fiber within the chamber. The emitted light will be coupled into the fiber directly and then, the light detected by a 0.32 monochromator (Jobin-Yvon Triax-320) with 1800, 1200, and 300 grooves/mm grating and the maximum width if the entrance slit was 1 mm. For the chamber design, the samples were placed in the closed-cycle cryostat with a temperature controller ranging from low temperature to room temperature. The cooling system is an open-cycle, which means liquid helium, 4K, or liquid nitrogen, 77K, injected in one tube and then leaked from the other tube. Though a larger amount of liquid source was needed, this kind of open cycle system provides a stable environment to avoid the shaking influence. The setup of the temperature dependent EL measurement system was shown in figure 5.1.

5-2 Sample Preparation

The sample used in this chapter was commercial InGaN/GaN MQW UV LEDs grown by MOCVD. The PSS geometry was the same as the substrate in previous chapter. The sample consists 1.5 μm undoped n-GaN, a 2 μm Si-doped n-type GaN, and an unintentionally doped active layer with $In_xGa_{1-x}N$/GaN MQWs, and a 20nm p-AlGaN electron blocking layer (EBL), a 50nm p-$Al_{0.2}Ga_{0.95}N$, and 20nm Mg-doped p-type GaN. The doped concentration of n- and p-type GaN is nominally 5×10^{18} and $1 \times 10^{19} cm^{-3}$, respectively, the MQWs layer comprise 6 periods InGaN well (~2.5nm) and GaN barrier (~1.5nm). The sample structure is shown in figure 5.2. The target wavelength is around 400 nm. Basically we would justify the IQE improvement by PL method; however, what we are interested here is the temperature dependent EL performance and efficiency droop phenomenon. So we choose a shorter wavelength device in this chapter. The fabrication processes of InGaN/GaN UV LED show in figure 5.3. Since we aimed to understand the internal material characteristics, instead of a high power device like we mentioned in chapter 3, we utilized a normal device process to form a p-side up device. First, a mesa structure was formed by ICP etching to define the device geometry. The fabricated sizes of both devices were 350x350 mm^2. Then, a TCL of indium-tin-oxide (ITO) was deposited by E-gun evaporator on whole surface. After we defined the pattern of TCL by second mask, the spare section was removed by ITO etcher. Finally, the p- and n-electrodes were then deposited by E-gun evaporator again for wire bonding or probing. Relative to the vertical-type device, this kind of structure is easier in process and suitable for a rapid test and device identification.

5-3 Results and Discussion

We then performed the temperature dependent EL measurements on the prepared UV LEDs on PSS and flat substrate sample. The APSYS simulation and an equivalent circuit model will be also developed. The details will be discussed in the following sections.

5-3.1 Temperature dependent EL characteristics

Temperature dependence EL at various injection current levels has been measured from 30 to 300 K. Before we start to discuss the variation of both samples under different temperature and injected current, we could take a look at the spectrums at several specific conditions. The three-dimensional (3D) plots of the EL spectrums at three injection currents of 0.1, 1, and 20 mA with different environment temperature were chosen and shown in figure 5.4 (a) to (c), respectively. First, when the injected current was as low as 0.1 mA in figure 5.4(a), we could observe a maximum at lowest temperature of 30 K in both samples. The intensity gradually decreased with the increasing temperature. Since the injected current maintains constant through whole measurement period, we could realize it as a reduced efficiency while the temperature increased. This result could be understood by relating to the behavior of nonradiative recombination process. The increased temperature would activate the nonradiative centers and deteriorate the device lighting efficiency. Since it is determined by the numbers of nonradiative centers and we had confirmed the PSS's effect to improve IQE, therefore, it is not surprising to observe a sharper slope of efficiency in flat sapphire sample.

When the injected current level increased to 1 mA, we notice that the curves had similar tendency with that at 0.1 mA, but the slope becomes smoother. It is then reasonable to assume there must exist some additional factor to influence the efficiency behavior and contribute to an opposite trend to the nonradiative centers. If we further increased the injection current to 20 mA, we found the efficiency peaks moved from the lowest temperature to about 80-100K. It means this unexpected factor lowering the efficiency at low temperature becomes stronger at high injection level. Therefore, the next step for our discussion is to find out what the mechanism is to cause the opposite trend, and realize the efficiency trend comes from at different current and environment temperature condition.

Temperature dependent EL at constant low current injection

In order to realize the origin of the efficiency curves, we discussed the whole results by four different conditions, that is temperature dependent EL at constant low and high current injection and current dependent EL at constant low and high environment temperature, respectively. Here, we started the discussion from the condition of a temperature dependent curve at constant low current injection of 0.1 mA.

As shown in figure 5.5(a), the efficiency decreased as the increasing temperature in both samples. Generally, thermal quenching phenomenon was observed in InGaN-based structures. At low injection current, the carrier injected into quantum well, and then the carriers can be confined due to the localized states in the In-rich region. In InGaN-based structures, the emission came from the localized states, which could trap carriers within this potential minimum. We could refer to the model of InGaN material system in figure 4.12. When the temperature increased, the carrier received activation energy to be thermalized and escaped from localized centers to defect or nonradiative centers resulting in the EL efficiency decreased. This mechanism caused a decrement in efficiency with increasing temperature as the red line in figure 5.5(b). However, we find not only the efficiency, but the voltage has an obvious increment with decreasing temperature. This forward voltage increasing of InGaN/GaN UV LEDs is believed due to the hole concentrations and mobility decrement [5] at low temperature operation. The authors in [5] had studied the variation of electron and hole concentration and mobility as shown in figure 5.6(a) and (b). From figure 5.6(a), the electron mobility becomes a half to a third from room temperature to 100 K but the hole mobility drops to one order of magnitude lower than that in room temperature as shown in figure 5.6(b). Lower the environment temperature, poorer the activated hole concentration and mobility. Hence, this will cause an observation of efficiency decrement as the environment temperature was cooling down as represented in the green line in figure 5.5(b). Finally, we could realize the efficiency tendency as the blue line. We note that, since the operation voltage shown in figure 5.5(c) does not vary that serious with the decreasing temperature, the efficiency suppression by green line is not that obvious. That is the reason we could still observe an efficiency peak at lowest temperature.

Temperature dependent EL at constant high current injection

We then move to the condition of constant high current injection condition, 20 mA, with a varied temperature as shown in figure 5.7. Compared to low injection case, the peak shifts to higher temperature. It is then interesting to find out what causes the difference. Basically, the influence of nonradiative centers did not change with the injection current, so the curve of nonradiative centers remains the same with the condition of low injection as the red line in figure 5.7. Followed by our previous assumption, the greatly reduced hole mobility suppress the efficiency especially at low temperature. This phenomenon could be realized and quantized by observing the voltage variation from room temperature to low temperature. While the injected current is 0.1 mA, the operation voltage varied about 0.5 V from room temperature to low temperature but it increased about 1.4 V at 20 mA current injection. This implies the influence of the poorer hole mobility becomes stronger than low injection level. So, the curve of the hole concentration and mobility could be expressed as the green line in figure 5.7(b) and the efficiency curve is represented as the blue line.

In figure 5.7(c), the forward voltage increased about 1 and 1.4 V for PSS and flat sapphire UV LED, respectively. Therefore, we conclude that the variation of operation voltage plays an important role in temperature dependence EL efficiency, especially, the EL efficiency may be affected when decreasing temperature at high injection current. In high injection current, it appears that the carriers are effectively captured by active centers in the MQW under the application of lower forward voltage at room temperature. But, forward voltage increased while decreasing temperature, they are rather transferred to nonradiative recombination centers as a result of escape from the MQW region, thus reducing the EL efficiency. This is because the carriers can escape out of the well region due to the external field effects as shown in figure 5.8. We also demonstrated that the higher field existing in the well under the higher forward voltage decreases the radiative recombination rate, which also causes the reduced EL intensity.

Current dependent EL at constant low environment temperature

We had discussed about the conditions of temperature dependent results at low and high current injection. Next, we tried to understand the current dependent EL at a low and room temperature case. We first plotted the efficiency curves from 0.1 to 100 mA at low temperature, 30 K, environment as shown in figure 5.9(a). The EL quantum efficiency at 30K increased slightly with increasing injection current before injection current is below 1 mA. Recall the IQE measurement form PL method; we conclude the initial stage with an increased IQE is belonging to the compensation of the nanradiative recombination centers. Though we cooling down the temperature to about 77 K, it is believed that is not sufficient to suppress all inherent dislocation. Therefore, the injected carriers were attributed to compensate the nonradiative recombination centers, and reach the maximum at about 1 mA. We find the black line, PSS UV LED, is higher than without PSS UV LED in red line before 1 mA. It could be explained as the PSS sample has fewer dislocations than the flat sample, so a higher and smoother IQE curve is observed.

While further increasing injection current, the EL efficiency drops rapidly, we observed that the reduction of EL efficiency of PSS InGaN/GaN UV LED is very similar to without PSS structure. The results indicated that the reduction of dislocation density didn't affect the efficiency seriously at high injection current. Therefore, we could understand the effect of nonradiative centers as a red curve shown in figure 5.9(b). Then, we look forward the role of hole concentration and mobility. Since the environment temperature was fixed in this case, the amount of operation voltage should be proportional to the injected current only. Therefore, the efficiency should be decreased with the increasing current. The EL efficiency reduction at high injection currents is coming from the higher forward voltage which results in carriers escape from the quantum well and overflow to p-GaN. This influence could be represented as the green line in figure 5.9(b) and the efficiency is black one. Relative the device operated at room temperature, the voltage variation is much serious as injected current increased as shown in figure 5.9(c). Therefore, the efficiency slope is sharper than in room temperature case.

Current dependent EL at room temperature

At the last case, we move to the case of injected current dependent EL efficiency at room temperature. The measured efficiency curves were shown in figure 5.10(a). The EL efficiency if both samples increased at the initial stage with a peak at about 8 mA and drops as the current continuously increased. Similar to above cases, we could understand the curved by dividing into two stages. First is the influence of dislocation at initial stage and second is hole concentration and mobility. Since the device is operated at room temperature, the nonradiative recombination strongly dominated the efficiency performance and that is the reason of PSS sample enjoyed a higher IQE than flat sample. This could undoubtedly be presented as the red line in figure 5.10(b). For the hole performance, since room temperature has little effect to the amount of activated hole concentration, it is quite flat during whole current region as the green line in figure 5.10(b). Hence, the efficiency is combined as the black line. One thing should be noted is the operation voltage difference between PSS and flat sample is negligible as shown in figure 5.10(c). So the high current region remains identical tendency to the low injection region, we could observe a higher EL IQE curve in PSS than flat sample in the whole current injection period.

5-3.2 Equivalent circuit analysis for temperature dependent EL efficiency

We summarized the temperature dependent EL efficiency curves in figure 5.11(a) and (b), which acted as a function of injection current of PSS and without PSS InGaN/GaN UV LED, respectively. At first glance, one could find that every temperature, as the injected current increased, has peak efficiency. However, this peak position varied as the temperature changed. For example, it is around 8 mA when the temperature is above 120 K and gradually moved to 1 mA when temperature was decreased to 80 K. Moreover, the maximum in whole the measurement curves happened at 100 K for flat sample as shown in figure 5.11(a) and 80 K for PSS sample in figure 5.11(b), instead of the lowest temperature. Here, we adopted the equivalent circuit model proposed by Shuji Nakamura and Steven P. Denbaars *et al.* [6] for better understanding of the temperature dependence EL efficiency tendency. They claimed four components putting in the equivalent circuit model illustrated in figure 5.12(a). This circuit model ensures all injected carriers are traced and are not unintentionally lost. The resistor R_1 represents current leakage paths, such as extended crystal defects and sample surface, for example. This current component is not considered to involve carrier recombination, hence is purely carried by electrons. There are two diodes in this model. Diode D_1 is responsible for current flow due to radiative recombination. This current component results in photon emission and detection upon recombination. Diode D_2 is responsible for nonradiative recombination current. Such recombination occurs via nonradiative recombination centers (NRCs) and does not emit photons within the wavelength range of interest. These two types of recombination are not limited within or near the active region. They are distinguished by whether a photon is emitted and detected within the wavelength range of interest upon a recombination event. Another resistor R_2 combined with a switch represents carrier overflow. This component is considered to be the electron unipolar current, i.e., is carried by electrons that do not recombine with holes and exit the system to the p-type contact. Current division between I_{D1} (through D_1) and I_{D2} (through D_2) is defined as:

$$\beta = \frac{I_{D1}}{I_{D1} + I_{D2}} = \frac{r_R}{r_R + r_{NR}} \qquad (5\text{-}1)$$

where r_R is the radiative recombination rate and r_{NR} is the nonradiative recombination rate. EL efficiency is defined in this current range as

$$\eta = \frac{I_{D1}}{I_T} = \beta \frac{I_D}{I_T} \qquad (5\text{-}2)$$

where $I_D = I_{D1} + I_{D2}$ and $I_T = I_D + I_{R1}$ have been implemented. Ohms law and the diode equation are taken to identify the fundamental behavior of:

$$I_{R1} = \frac{V}{R_1} \tag{5-3}$$

$$I_D = I_{D0}[\exp(\frac{qv}{nkT}) - 1] \tag{5-4}$$

V is the applied voltage, I_{D0} is the diode saturation current, q is the unit charge, n is the ideality factor, k is the Boltzmann constant, and T is the absolute temperature. Equations (5-3) and (5-4) can be related via V to obtain from eq. (5-2) as

$$\eta = \beta(T)[\frac{1}{I_D}\frac{nkT}{qR_1}\ln(\frac{I_D}{I_{D0}}+1)-1]^{-1} \tag{5-5}$$

By substituting β=1 and I_{D0}=10 pA into equation 5-5, we could estimate the efficiency number with different R_1 as shown in figure 5.12(b). Since the efficiency is inverse proportional to R_1, it reaches the ideal maximum, ~1, while R_1 is infinite. On the other hand, the efficiency decreased if R_1 becomes smaller. Therefore, we can observe the entire curve gradually shifts upwards towards EL efficiency ~ 1 as a result of nonradiative recombination centers deactivation when temperature is reduced. In this model, the EL efficiency increased when increasing injection current, and the EL efficiency curve bending less sharp while temperature is decreasing. The phenomenon indicated that the significant leakage current existed, and the leakage current is reduced when temperature decreased. It also coincides with the results we found in figure 5.9(a), that is, the PSS sample has less dislocation density, i.e., the larger R_1 and contributes to a higher IQE.

We finally summarized the EL efficiency as a function of injection current at 77 and 300 K and normalized to the maximum number at 77 K as shown in figure 5.13. The EL efficiency is 60.3%, and 41.6% at 20 mA of PSS and without PSS InGaN/GaN UV LED, respectively. From this comparison results, we could reasonably assume that we could also get an IQE number by this method once we could estimate and get the peak number. The next problem will be, since we had established a method for IQE estimating by PL method, what the difference between these two methods. Therefore, the comparison between these two methods will be discussed.

5-3.3 Comparison of IQE Measurement by PL and EL Methods

We performed the IQE measurement by PL method and compared the results between these two, PL and EL, as shown in figure 5.14. Here we transformed the laser power in PL and injected current in EL method into carrier density in a unit of particles per centimeter cubic. For current and carrier density transformation, we need to calculate the active area and assume the current spreading in whole active region uniformly. Then, we could put the EL and PL results in a figure for comparison. The IQE tendency of EL and PL at low and room temperature are showing there. The solid lines represent the results from EL method and hallow lines represent the results from PL method. The normalized peak position does not have obvious difference between these two methods; however, the curves at room temperature have an apparent difference. We could understand it by dividing into low temperature and room temperature cases.

For low temperature case, the PL efficiency is higher than EL efficiency at low carrier injection level, that means there exists more leakage paths while EL injection. More leakage current occurred when electrical injected carrier into quantum well to be captured by nonradiative recombination centers in n-GaN. Figure 5.15(a) demonstrated that some leakage current appeared in n-GaN and capture the injected electrons to deteriorate the device efficiency. On the other hand, it would not happen when the electrons were resonant pumped by a 390 nm laser and being able to well confined in MQWs without being absorbed by defects in n-GaN. Further increasing injected carrier density, the PL and EL efficiency decreased due to carrier began to overflow from quantum well to p-GaN layer as shown in figure 5.15(b). And we found that the EL efficiency decreased more rapidly at high injected carrier density, it can be attributed to the forward voltage increased when increasing injected carrier density and pushing carriers escaping from the quantum well and overflow to p-GaN resulting an efficiency reduction.

For room temperature side, we observed a higher IQE curve in both PSS and flat sample from PL results than EL case. We depicted the schematic of electron an hole injection recombination as shown in figure 5.16. As we know, both electron and hole concentration and mobility decreased when decreasing temperature, but the degree of decrement in holes is nearly one magnitude serious than electrons. This fact caused that hole concentration distribution is extremely non-uniform and insufficient to fill up whole the active region. Therefore, some electrons migrate to the last few pairs of MQWs near p-GaN and recombine at the surface finally. This could fully explain the lower IQE curves from EL results than PL.

5-3.4 APSYS simulation

From the discussion above, we could conclude that there are two main factors influencing the device efficiency under current injection condition, the density of dislocation and hole concentration and mobility variation. The dislocation density has been verified by TEM and IQE measurement in previous chapter; however, we had not been able to verify the effect of hole characteristics. In this section, we tried to verify it by the help of packaged simulation software, APSYS. Since the activated hole concentration and hole mobility would be strongly reduced under a low temperature condition, we simulated a condition of three order of magnitude reduction in concentration and mobility. The simulated *I-V* curves were shown in figure 5.17. The solid line represents our experimental results and the dash line stands for the simulation results. It is quite match between our simulated and experimental results. can see the simulation of I-V curve is similar to experimental results. Furthermore, based on this parameters, we simulated the electron and hole distribution inside the MQWs as shown in figure 5.19(a) and (b), respectively. The black and red line represents the condition at 300 and 77K, respectively. The electron concentration distribution is quite uniform, but still a higher (~five times) electron concentration is observed near p-GaN than near n-GaN as shown in figure 5.18(a). This investigation also coincides with our contention before for some electrons would transport to p-GaN easily due to the non-uniform hole distribution. Figure 5.18(b) displays the hole concentration distribution in MQW, we found a more serious non-uniform distribution of hole concentration in the MQWs. The hole concentration in MQW near p-GaN is over one order of magnitude than near n-GaN. The shortage of injected holes failed to effectively recombine with the electrons, so that some of the injected electrons reach the p-GaN and exit the system without being able to recombine. Then, figure 5.19 shows the radiative recombination rate of each quantum well, we observed a higher readiative recombination rate near p-GaN due to the insufficient hole injection to MQWs. Consequently, the results verified the EL efficiency droop more rapidly at lower temperature.

Finally, figure 5.20 shows the band diagram at high injection current of InGaN/GaN MQW at low and room temperature. From this picture, high forward voltages for significant currents to flow, so that the conduction band on the n-side of the device is significantly higher than the conduction band on the p-side. This makes it energetically favorable for electrons to escape to the p-side of the device. The band inclined caused that more carriers overflow from quantum well and transport to p-GaN, the results make the EL efficiency droop quickly at lower temperature.

Reference:

[1] Hori, D. Yasunaga, A. Satake, and K. Fujiwara, Applied Physics Letter **79**, 3723 (2001)

[2] C. M. Lee, C. C. Chuo, J. F. Dai, X. F. Zheng, and J. I. Chyi, Journal of Applied Physics **89**, 6554 (2001)

[3] C. L. Yang, L. Ding, J. N. Wang, K. K. Fung, W. K. Ge, H. Liang, L. S. Yu, Y. D. Qi, D. L. Wang, Z. D. Lu, and K. M. Lau, Journal of Applied Physics **98**, 023703 (2005)

[4] S. Grzanka, G. Franssen, G. Targowski, K. Krowicki, T. Suski, R. Czemecki, P. Perlin, and M. Leszczyski, Applied Physics Letter **90**, 103507 (2007)

[5] P. Bakmiwewa, A. Hori, A. Satake, K. Fujiwara, Physica E **21**, 636 (2004)

[6] H. Masui, T. Ive, M. C. Schmidt, H. Sato, H. Asamizu, S. nakamura, and S. P. Denbaars, Japan Journal of Applied Physics **47**, 2112 (2008)

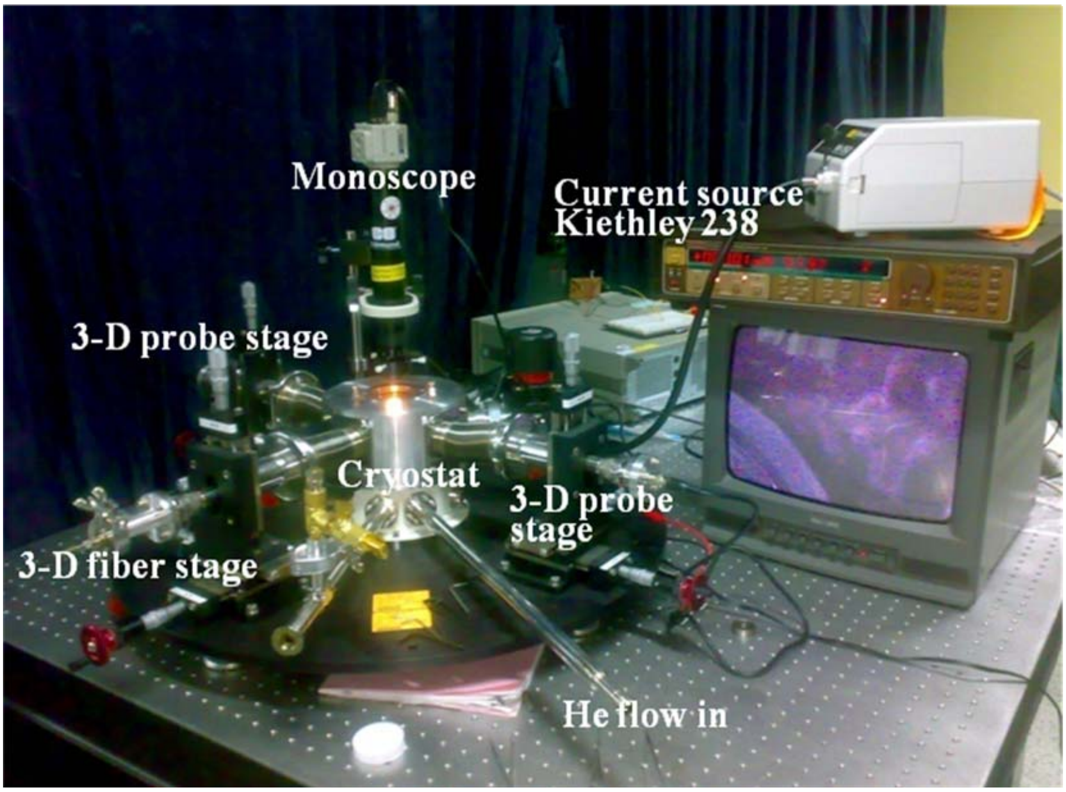

Figure 5.1 The schematic of temperature dependent electroluminescence measurement instrument.

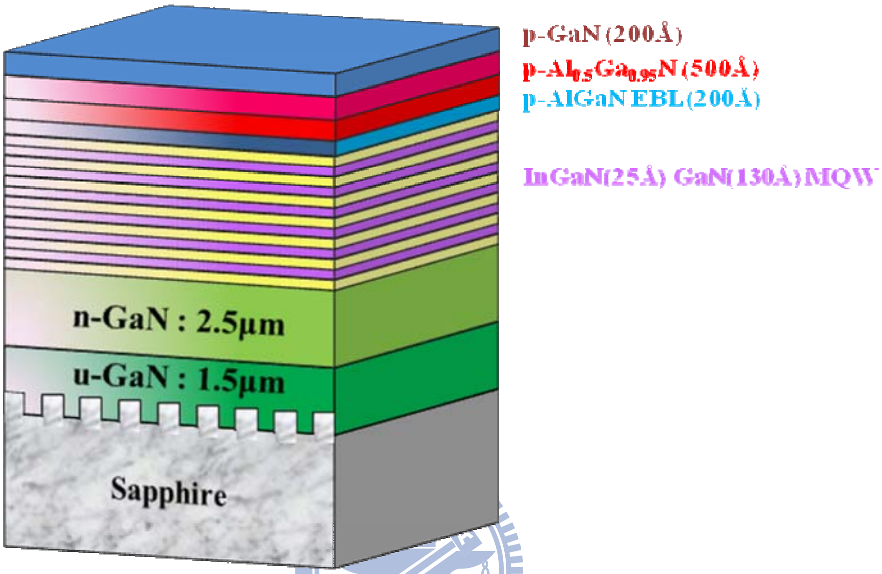

Figure 5.2 The schematic of UV LED structure

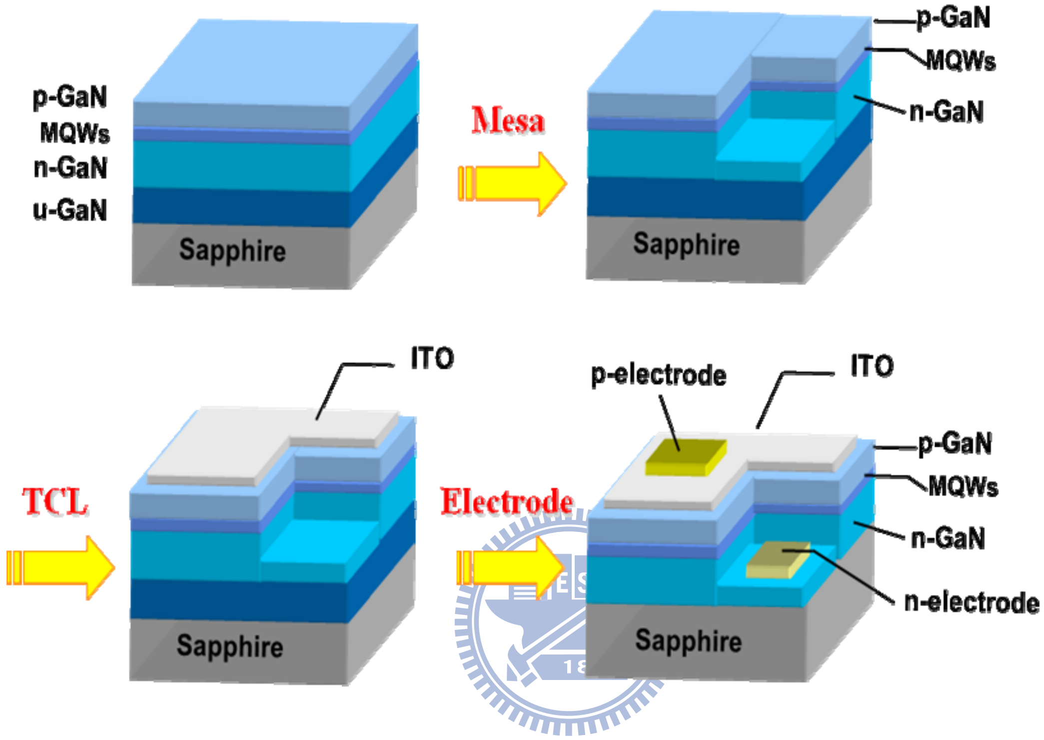

Figure 5.3 The schematic of sapphire-based UV LED fabrication processes

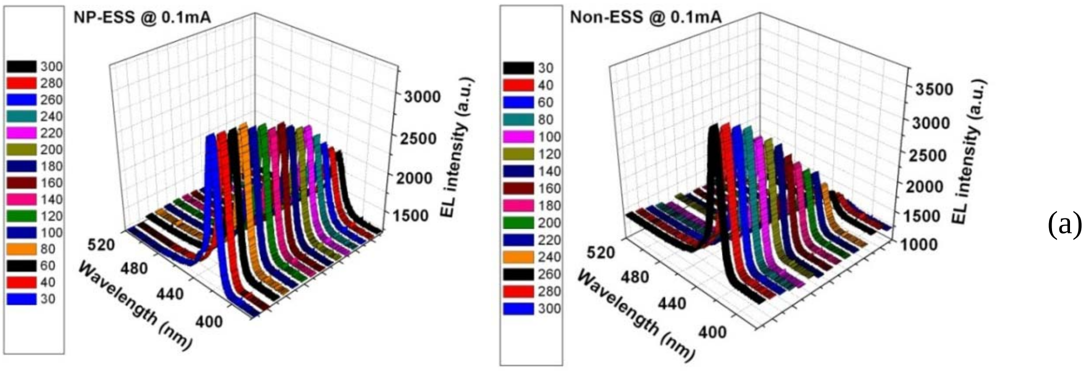

Injection current of 0.1mA

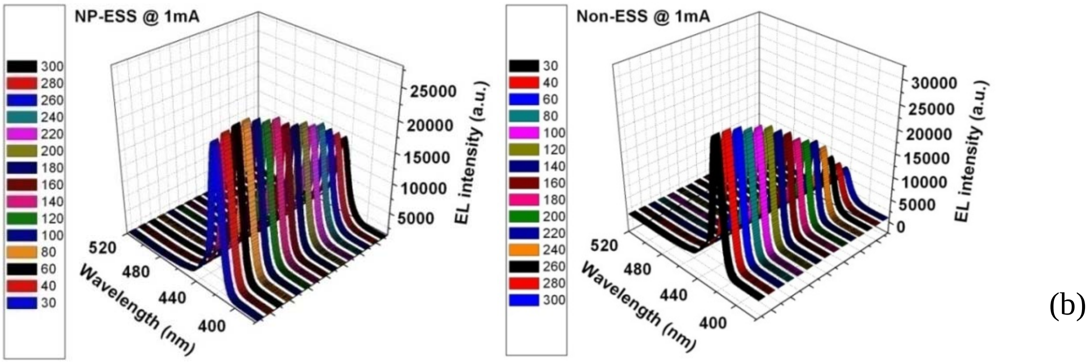

Injection current of 1mA

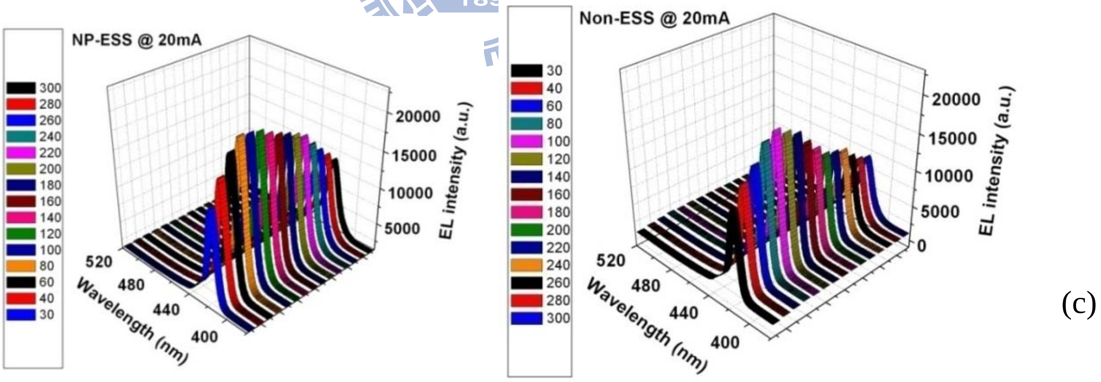

Injection current of 20mA

Figure 5.4 Temperature dependence of the EL spectra for InGaN/GaN UV LED at injection currents of (a) 0.1 mA, (b) 1 mA, and(c) 20 mA.

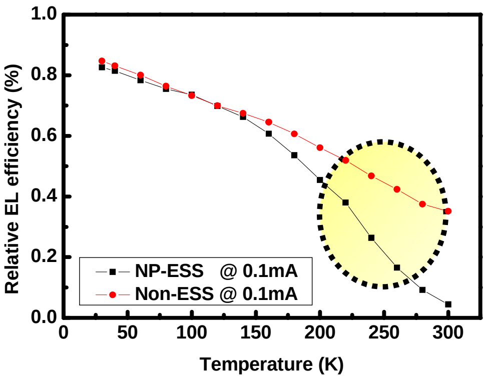

(a)

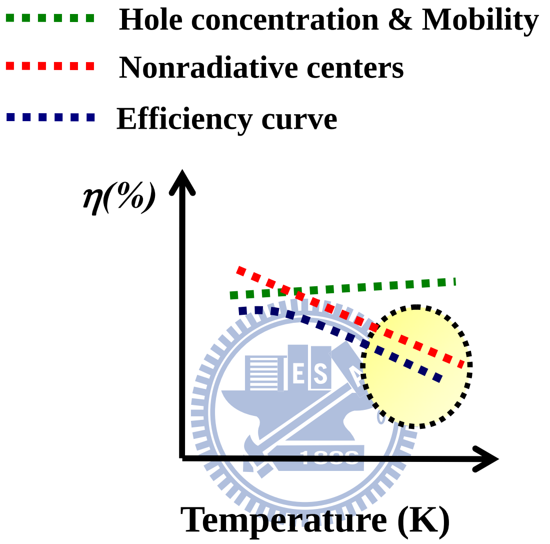

(b)

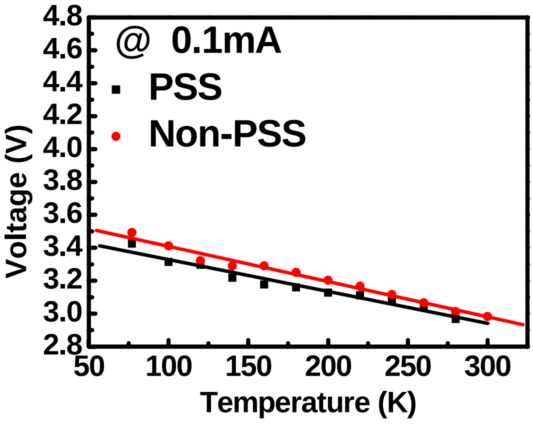

(c)

Figure 5.5 Temperature dependence of the EL efficiency of PSS and flat sapphire sample at 0.1mA. (b) Schematic drawing of temperature dependence EL efficiency. (c) Temperature dependence forward voltage variation at 0.1mA

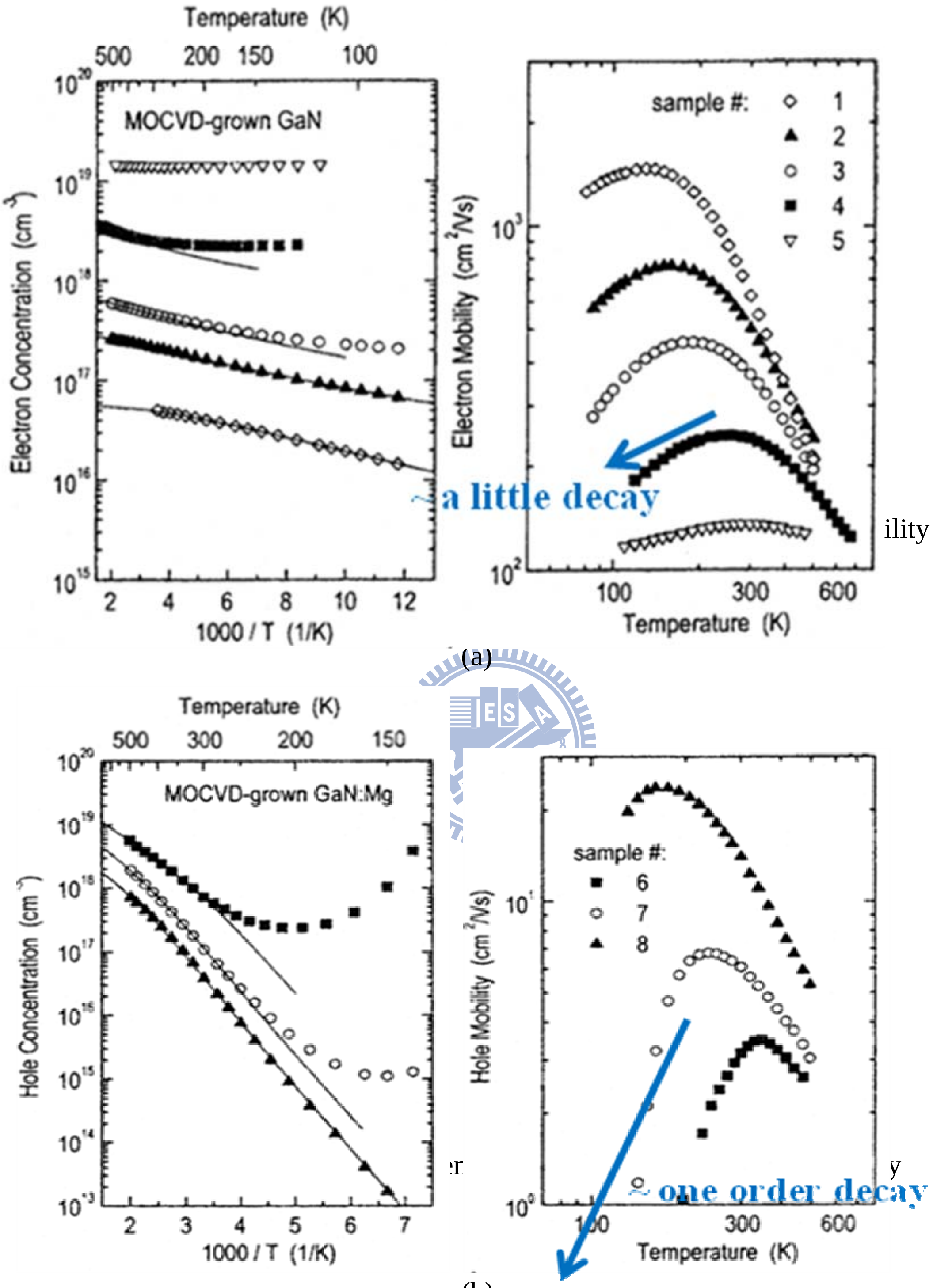

(a)

(b)

Figure 5.6 Temperature dependence (a) electron concentration and mobility and (b) hole concentration and mobility variation

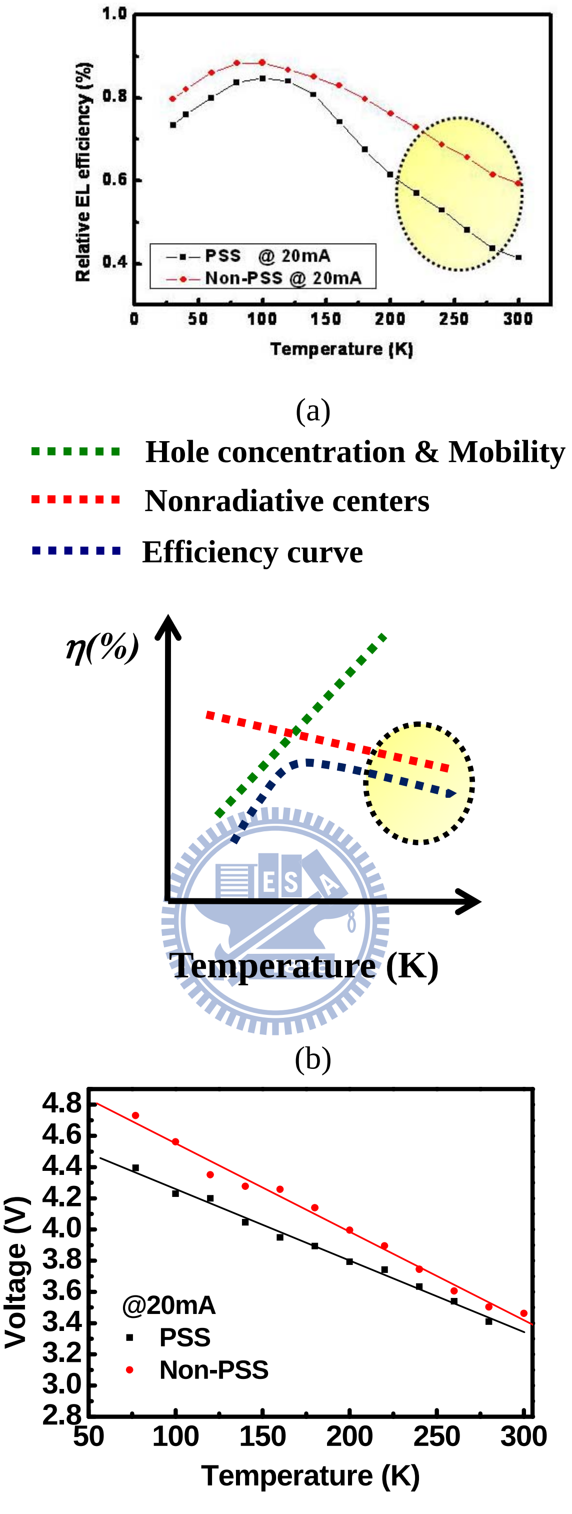

(a)

(b)

(c)

Figure 5.7 Temperature dependence of the EL efficiency of PSS and flat sapphire sample at 20 mA. (b) Schematic drawing of temperature dependence EL efficiency. (c) Temperature dependence forward voltage variation at 20 mA

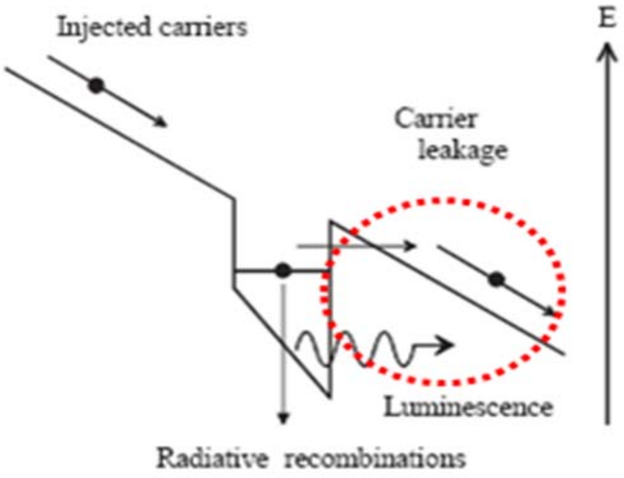

Figure 5.8 Schematic model for carrier capturing influenced under higher voltage

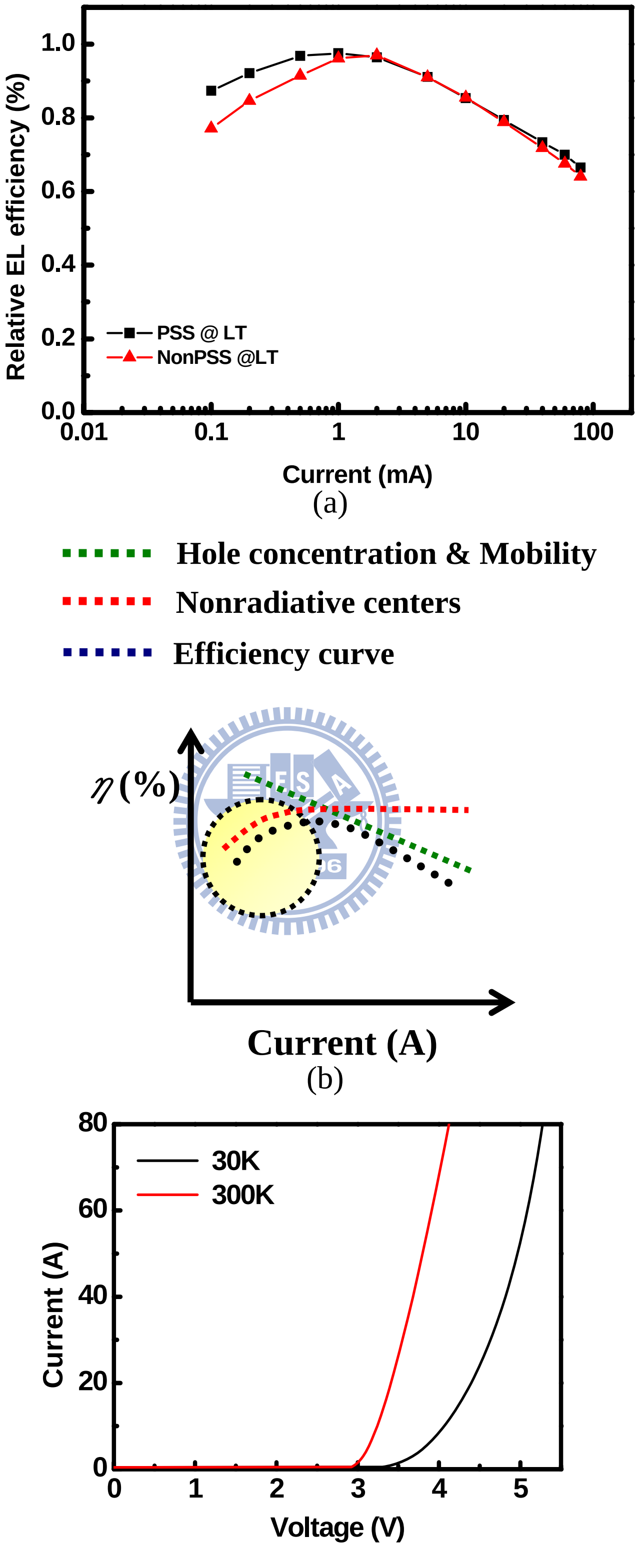

(a)

(b)

(c)

Figure 5.9 (a) Current dependence of the EL efficiency at 30K. (b) Schematic drawing of current dependence EL efficiency. (c) Current dependence forward voltage at 30K

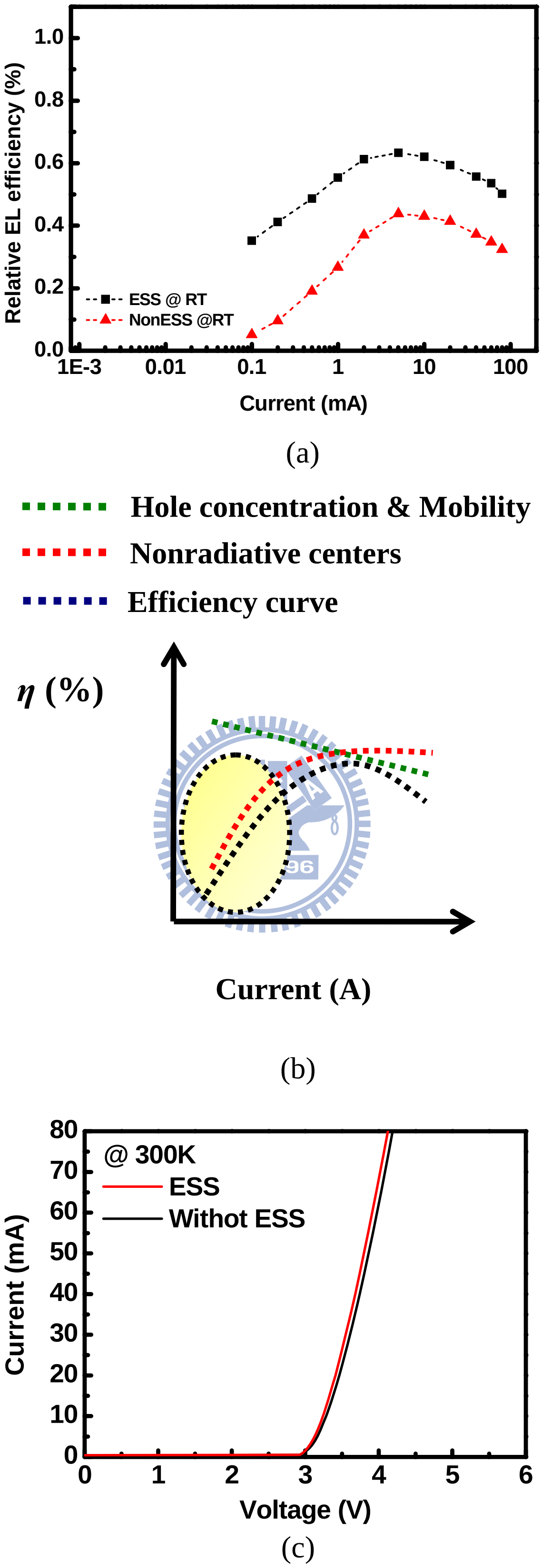

(a)

(b)

(c)

Figure 5.10 Current dependence of the EL efficiency at 300K. (b) Schematic drawing of current dependence EL efficiency. (c) Current dependence forward voltage at 300K

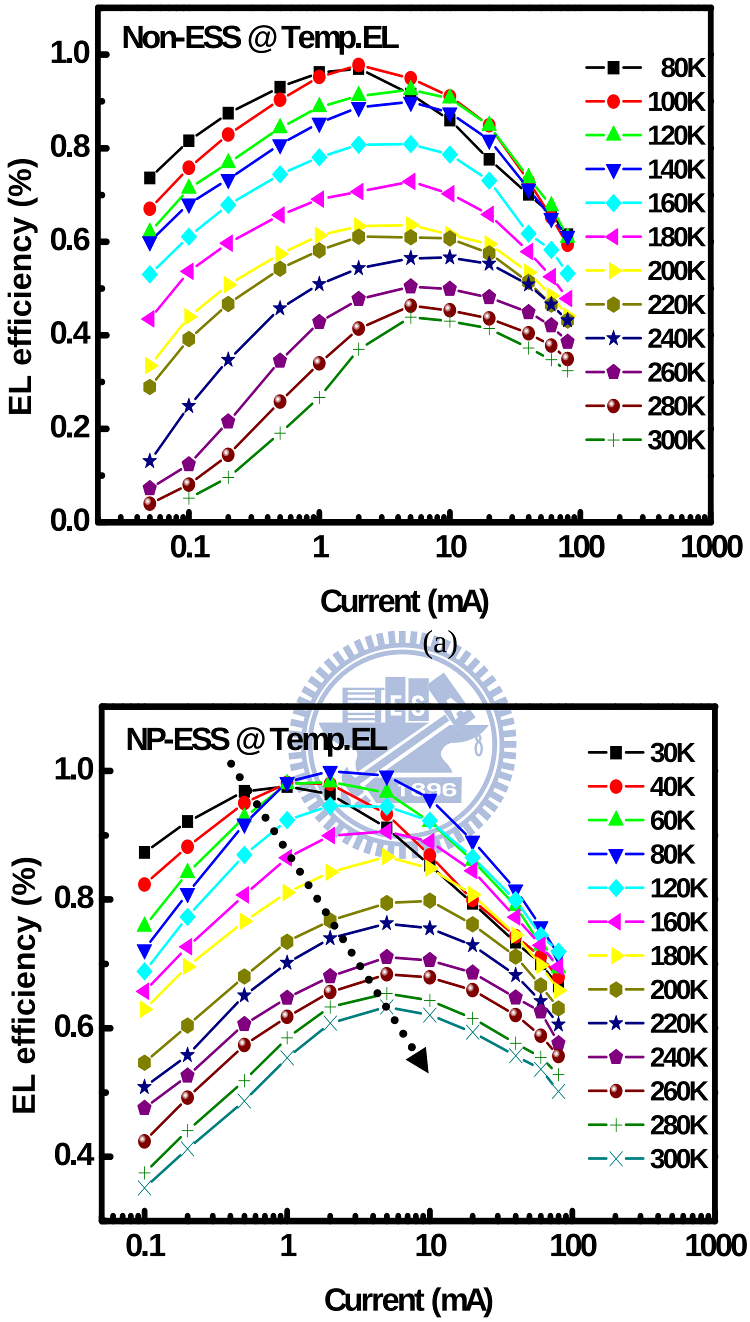

(a)

(b)

Figure 5.11 Temperature dependent EL efficiency as a function of injection current of (a) LED on flat sapphire and (b) PSS InGaN/GaN UV LED

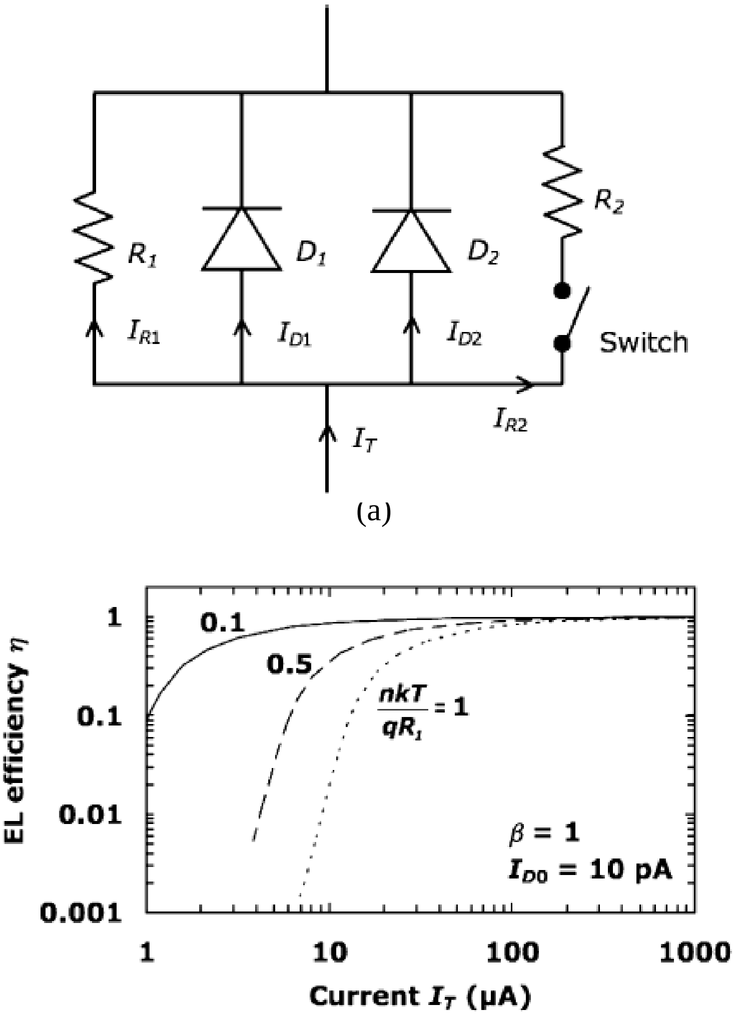

(a)

(b)

Figure 5.12 (a) An equivalent circuit to represent the four current components: leakage current I_{R1} by resistor R_1, radiative current I_{D1} by diode D_1, nonradiative current I_{D2} by diode D_2, and carrier-overflow current I_{R2} by resistor R_2 with a switch. (b) EL efficiency as a function of current in the low-current range,

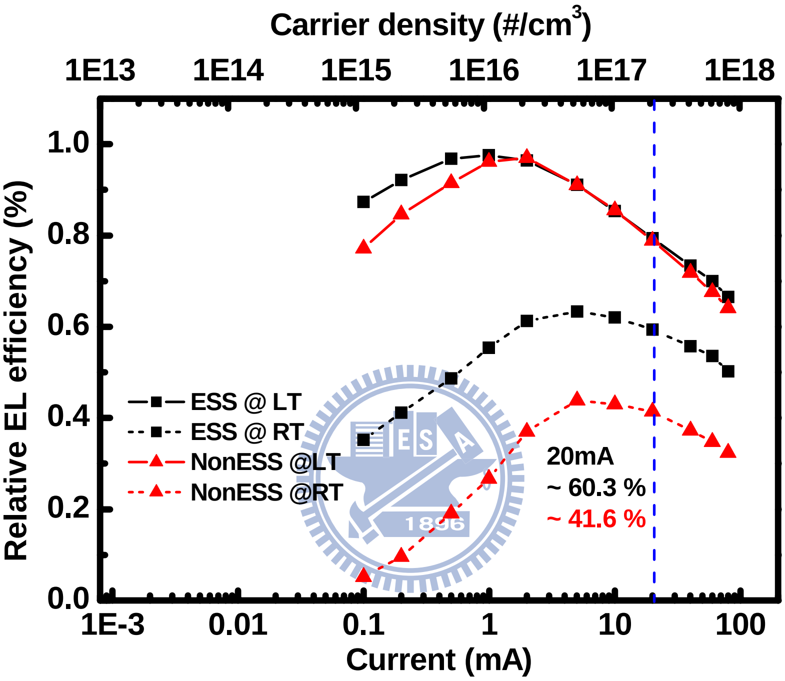

Figure 5.13 EL efficiency as a function of injection current at 77K and 300K

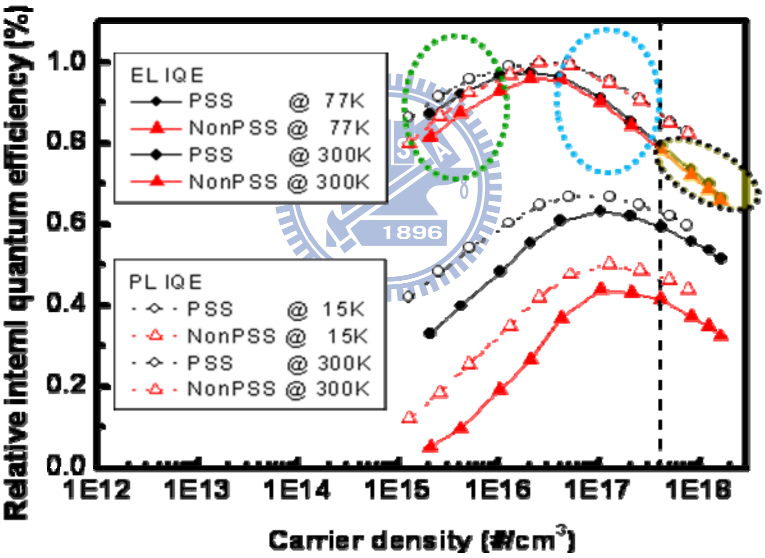

Figure 5.14 EL and PL efficiency as a function of injection current at low temperature and room temperature

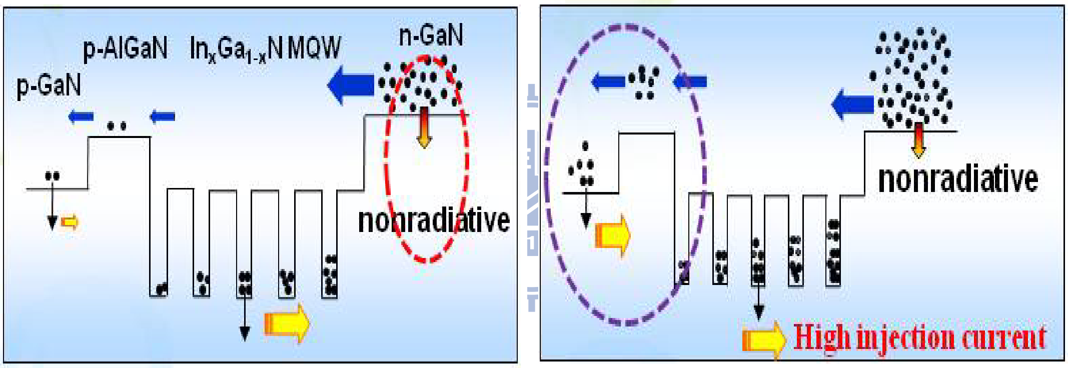

Figure 5.15 Schematic drawing of carrier transport at low and high injection current

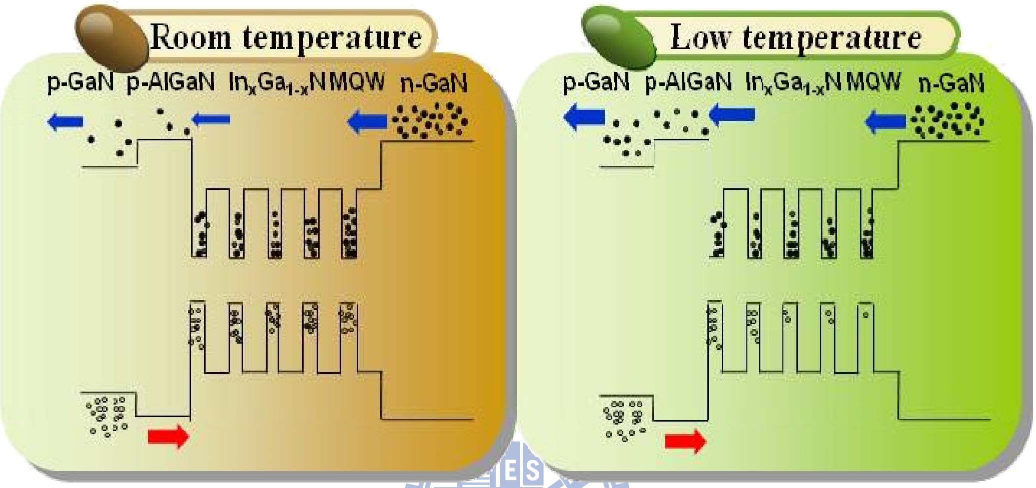

Figure 5.16 Schematic drawing of electron and hole concentration distribution at low and high injection current

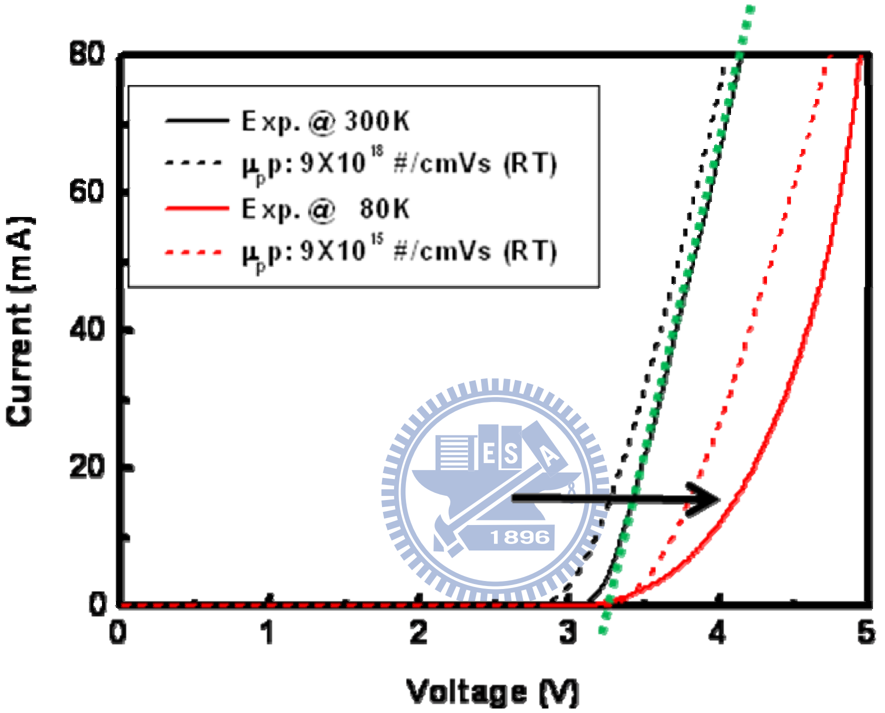

Figure 5.17 I-V curve of simulation with different hole concentration and mobility

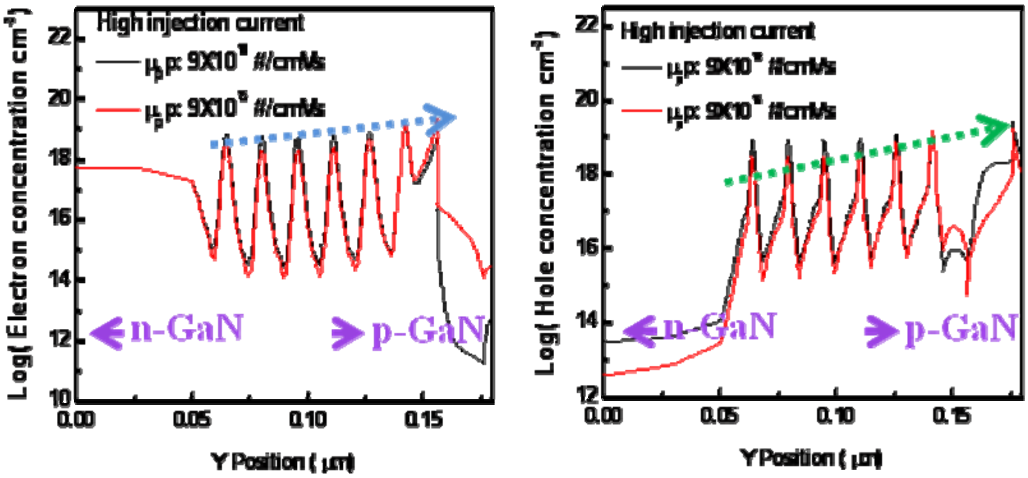

(a) (b)

Figure 5.18 Electron and hole concentration distribution at high injection current

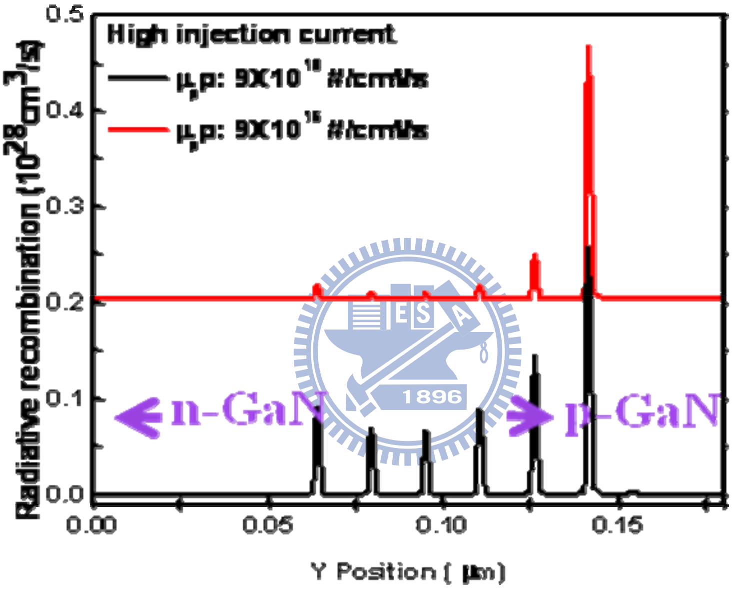

Figure 5.19 Radiative recombination at high injection current of InGaN/GaN MQW

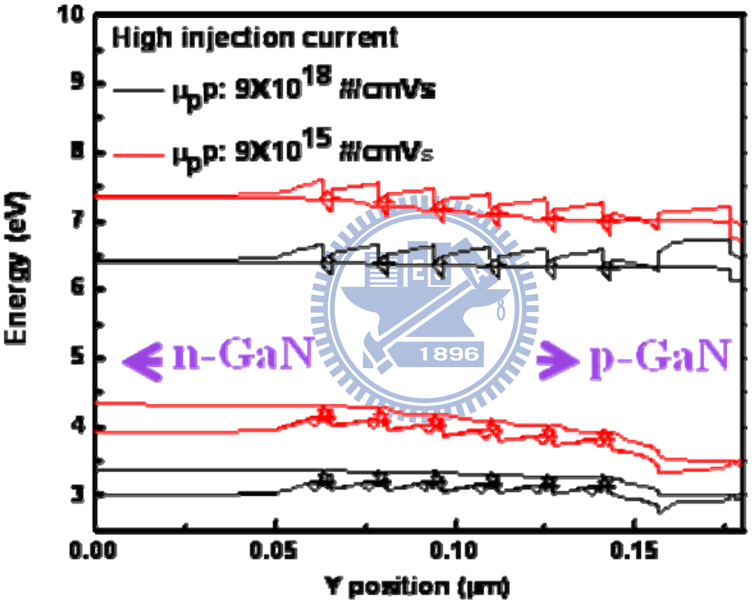

Figure 5.20 Band diagram at high injection current of InGaN/GaN MQW

CHAPTER 6

Summary

To sum up, in this dissertation, we had successfully developed a novel method to fabricate GaN nanorod structures. The optical properties, such as emitting intensity, wavelength shift than bulk materials and anti-reflection properties had been fully discovered. Besides, a VFF model had also developed to analysis the influence of strain relaxation by fabricating different sizes of GaN nanorods. Not only the optical properties, we applied these nano structures on the surface of GaN-based LEDs to improve the device performance. Both GaN nanorod formed by ICP etching method and ZnO nanorod by synthesizing at aqueous solution could contribute to higher luminescence efficiency. Besides the structure research, we also studied the fact of IQE improvement by LED grown on PSS substrate. Both PL and EL methods were established for verification. For PL method, the mechanism of how dislocation density affects IQE had been discovered. The EL measurement not only provides an important evidence of IQE improvement by PSS method, but also great help on realizing more about efficiency droop phenomenon. The achievement in this dissertation is significant for the realization of next generation solid state lighting.

Publication List

(A) Journal Papers :

[1] **C. H. Chiu**, Peichen Yu, H. C. Kuo, C. C. Chen, T. C. Lu, S. C. Wang, S. H. Hsu, Y. J. Cheng, and Y. C. Chang, "Broadband and omnidirectional antireflection employing disordered GaN nanopillars", Optics Express **16**, 8748 (2008)

[2] **C. H. Chiu**, S. Y. Kuo, M. H. Lo, C. C. Ke, T. C. Wang, Y. T. Lee, H. C. Kuo, T. C. Lu, and S. C. Wang, "Optical properties of *a*-plane InGaN/GaN multiple quantum wells on *r*-plane sapphire substrates with different indium compositions", Journal of Applied Physics 105, 063105 (2009)

[3] C. H. Chang, P. Yu, **C.H. Chiu**, C. S. Yang, J. C. Yu, H. C. Kuo, S. H. Hsu, and Y. C. Chang, "Efficiency Enhancement of GaAs Photovoltaics Employing Anti-Reflective Indium-Tin-Oxide Nano-Columns", Advanced Material **21**, 1618-1621 (2009)

[4] P. Yu, **C. H. Chiu**, Y. R. Wu, H. H. Yen, J. R. Chen, C. C. Kao, H. W. Yang , H. C. Kuo, T. C. Lu, W. Y. Yeh, and S. C. Wang, "Strain Relaxation Induced Micro-Photoluminescence Characteristics of a Single InGaN-based Nanopillar Fabricated by Focused Ion Beam Milling", Applied Physics Letter **93**, 081110 (2008) and was selected in Virtual Journal of Nanoscale Science & Technology **18**, (2008)

[5] **C. H. Chiu**, H. H. Yen, C. L. Chao, Z. Y. Li, Peichen Yu, H. C. Kuo, T. C. Lu, S. C. Wang, K. M. Lau, and S. J. Cheng, "Nanoscale Epitaxial Lateral Overgrowth of GaN-based Light Emitting Diodes on a SiO_2 Nanorod-Array Patterned Sapphire Template", Applied Physics Letter **93**, 081108 (2008)

[6] **C. H. Chiu**, M. H. Lo, T. C. Lu, Peichen Yu, H. W. Huang, H. C. Kuo, and S.C. Wang, "Nano-processing Techniques Applied in GaN-based Light Emitting Devices with Self-assembly Ni Nano-masks", Journal of Lightwave Technology **26**, 1445

(2008)

[7] **C. H. Chiu**, C. E. Lee, C. L. Chao, B. S. Cheng, H. W. Huang, H. C. Kuo, T. C. Lu, S. C. Wang, W. L. Kuo, C. S. Hsiao, and S. Y. Chen, “Enhancement of Light Output Intensity by Integrating ZnO Nanorod Arrays on GaN-Based LLO Vertical LEDs,” Electrochemical and Solid-State Letters **11**, H84 (2008)

[8] **C. H. Chiu**, T. C. Lu, H. W. Huang, C. F. Lai, C. C. Kao, J. T. Chu, C. C. Yu, H. C. Kuo, S. C. Wang, C. F. Lin and T. H. Hsueh, “Fabrication of InGaN/GaN nanorod light emitting diodes with self-assembled Ni metal islands”, Nanotechnology **18**, 445201 (2007)

[9] **C. H. Chiu**, H. C. Kuo, C. E. Lee, C. H. Lin, P. C. Cheng, H. W. Huang, T. C. Lu, S. C. Wang, K. M. Leung, ” Fabrication and characteristics of thin film InGaN/GaN light emitting diodes with TiO_2/SiO_2 omnidirectional reflectors”, Semiconductor Science and Technology **22**, 831 (2007)

[10] **C. H. Chiu**, H.C. Kuo, C. F. Lai, H. W. Huang, W. C. Wang, T.C. Lu and S. C. Wang, “Enhancement of InGaN/GaN flip chip Intiun-Tin-Oxide light emitting diodes with inclined sidewalls coated with TiO_2/SiO_2 omnidirectional reflector”, Journal of The Electrochemical Society **154,** H944 (2007)

[11] **C. H. Chiu**, M. H. Lo, C. F. Lai, T. C. Lu, H. W. Huang, Y. A. Chang, T. H. Hsueh, C. C. Yu, H. C. Kuo, S. C. Wang, C. F. Lin and Y. K. Kuo, “Optical properties of $In_{0.3}Ga_{0.7}N/GaN$ green emission nanorods fabricated by plasma etching”, Nanotechnology **18**, 335706 (2007)

[12] **C. H. Chiu**, Zhen-Yu Li, C.L. Chao, M.H. Lo, H.C. Kuo, P.C. Yu, T.C. Lu, S.C. Wang, K.M. Lau, S.J. Cheng, “Efficiency enhancement of UV/blue light emitting diodes via nanoscaled epitaxial lateral overgrowth of GaN on a SiO2 nanorod-array patterned sapphire substrate” Journal of Crystal Growth **310**, 5170 (2008)

[13] **C. H. Chiu**, C. E. Lee, M. H. Lo, H. W. Huang, T. C. Lu, H. C. Kuo, and S. C. Wang "Metal Organic Chemical Vapor Deposition Growth of GaN-Based Light Emitting Diodes With Naturally Formed Nano Pyramids" Japanese Journal of Applied Physics **47**, 2954 (2008)

[14] Yuh-Renn Wu, **Ching-Hua Chiu**, Cheng-Yu Chang, Peichen Yu, and Hao-Chung Kuo, "Size-Dependent Strain Relaxation and Emission Characteristics of InGaN/GaN Nanorod Light Emitting Diodes," IEEE J. Select. Topics Quantum Electron. **15**, 1226 (2009)

[15] Ya-Ju Lee, **C. H. Chiu**, P. C. Lin, T. C. Lu, H. C. Kuo and S. C. Wang, "Study of the Excitation Power Dependent Internal Quantum Efficiency in InGaN/GaN LEDs Grown on Patterned Sapphire Substrate," IEEE J. Select. Topics Quantum Electron. **15**, 1137 (2009)

[16] C. L. Chao, **C. H. Chiu**, Y. J. Lee, H. C. Kuo, P. C. Liu, J. D. Tsay, and S. J. Cheng, "Freestanding high quality GaN substrate by associated GaN nanorods self-separated hydride vapor-phase epitaxy" Applied Physics Letter **95**, 051905 (2008)

[17] M. A. Tsai, P. Yu; J. R. Chen, J. K. Huang, **C. H. Chiu**, H. C. Kuo, T. C. Lu, S. H. Lin, S. C. Wang, "Improving Light Output Power of the GaN-Based Vertical-Injection Light-Emitting Diodes by Mg+ Implanted Current Blocking Layer,**"** IEEE Photonic Technology Letter, **21**, 11 688-690 (2009)

[18] M. A. Tsai, P. Yu; C. L. Chao, **C. H. Chiu**, H. C. Kuo, S. H. Lin, J. J. Huang, T. C. Lu, S. C. Wang, "Efficiency Enhancement and Beam Shaping of GaN–InGaN Vertical-Injection Light-Emitting Diodes via High-Aspect-Ratio Nanorod Arrays," IEEE Photonics Technology Letters, **21**, 4, 257-259 (2009)

[19] Y. J. Lee, S. Y. Lin, **C. H. Chiu**, T. C. Lu, H. C. Kuo, S. C. Wang, S. Chhajed, J. K. Kim, and E. F. Schubert, "High output power density from GaN-based two-dimensional

nanorod light-emitting diode arrays” Applied Physics Letter **94**, 141111 (2009)

[20] B. S. Cheng, **C. H. Chiu**, K. J. Huang, C. F. Lai, H. C. Kuo, C. H. Lin, T. C. Lu, S. C. Wang and C. C. Yu, “Enhance light extraction of InGaN-based green LEDs by nano-imprinted 2D photonic crystal pattern,” Semiconductor Science and Technology 23 (2008)

[21] H. W. Huang, C. H. Lin, C. C. Yu, B. D. Lee, **C. H. Chiu**, C. F. Lai, H. C. Kuo, K. M. Leung, T. C. Lu and S. C. Wang, “Enhanced light output from a nitride-based power chip of green light-emitting diodes with nano-rough surface using nanoimprint lithography, ” Nanotechnology 19 (2008)

[22] H. W. Huang, C. H. Lin, C. C. Yu, B. D. Lee, **C. H. Chiu**, C. F. Lai, H. C. Kuo, K. M. Leung, T. C. Lu and S. C. Wang, “Improvement of light output in GaN-based power chip light-emitting diodes with a nano-rough surface by nanoimprint lithography,” Semiconductor Science and Technology **23** (2008)

[23] Z. Y. Li, M. H. Lo, **C. H. Chiu**, P. C. Lin, T. C. Lu, H. C. Kuo, and S. C. Wang, “Carrier localization degree of In0.2Ga0.8N/GaN multiple quantum wells grown on vicinal sapphire substrates” Journal of Applied Physics 105, 013103 (2009)

[24] Z. Y. Li, W. Y. Uen, M. H. Lo, **C. H. Chiu**, P. C. Lin, C. T. Hung, T. C. Lu, H. C. Kuo, S. C. Wang, Y. C. Huang, “Enhancing the emission efficiency of $In_{0.2}Ga_{0.8}N$/GaN MQW blue LED by using appropriately misoriented sapphire substrates,” J. Electrochem. Soc., 156, (2), H129-H133, (Dec. 9, 2008)

(B) Conference Papers:

[1] **C. Chiu**, P. Yu, J. Chen, C. Kao, H. Kuo, T. Lu, S. Wang, Y. Wu and H. Yang, “Optical Properties of a Strain Relaxed Single InGaN-based Nanopillar Fabricated by Focused Ion Beam Milling”, The Electrochemical Society 2008 Hawaiian

[2] **C. Chiu,** H. Kuo, T. Lu, S. Wang, C. Hsiao and S. Chen, “Light Output Power Enhancement of GaN-based Vertical Light Emitting Diodes via Fabricating Surface Nanorod Arrays”, The Electrochemical Society 2008 Hawaiian

[3] B. S. Cheng, **C. H. Chiu**, H. C. Kuo, T. C. Lu and S. C. Wang, “Improved light-output of thin-GaN light-emitting diode with micro-reflector and roughened surface” , Solid State Devices and Materials 2008 Japan

[4] S. W. Chen, **C. H. Chiu**, T. T. Kao, L. F. Lin, T. C. Lu, H. C. Kuo, S. C. Wang, “Light Output Enhancement of GaN-based Photonic Crystal LED with AlN/GaN DBR”, Solid State Devices and Materials 2008 Japan

[5] **C. H. Chiu**, Peichen Yu, C. C. Chen, H. C. Kuo, T. C. Lu, and S. C. Wang, S. S. Hsu, Y. J. Cheng, and Y. C. Chang, “Broad Angular and Spectral Anti-Reflection Employing GaN Nano-Pillar Structures”, CLEO 2008 San Jose

[6] Peichen Yu, M. A. Tasi, **C. H. Chiu**, H. C. Kuo, Y. R. Wu, “Strain relaxation characteristics of a single InGaN-based nanopillar fabricated by focused ion beam milling”, APOC 2008

[7] F I Lai, H. W. Huang , **C H Chiu**, C. F. Lai, T. C. Lu, H. C. Kuo, S. C. Wang,” InGaN MQW Nanorods LED Fabricated by ICP-RIE and PEC Oxidation Processes,” CLEO/QELS2007 Conference, Baltimore, Maryland, USA, May 6-11,2007., paper CMO3

[8] C.E. Lee, **C.H. Chiu**, M.H. Lo, H.W. Huang, T.C. Lu, H.C. Kuo, S.C. Wang “MOCVD Growth of GaN-Based LEDs With Naturally Formed Nano-pyramids”, Solid State Devices and Materials (SSDM 2007), Ibaraki, Japan

[9] **C. H. Chiu**, H. C. Kuo, C. E. Lee, C. H. Lin, B. S. Cheng, P. C. Cheng, H. W. Huang, T. C. Lu, S. C. Wang, and K. M. Leung “Study of the Thin-Film GaN-Based LEDs with TiO2/SiO2 OmnidirectionalReflectors and PEC Roughened Surfaces”, 212th ECS Meeting, Washington, DC, USA

[10] Y. J. Lee, **C. H. Chiu**, H. C. Kuo, T. C. Lu, S. C. Wang, Kar Wai Ng, Kei May Lau, Z. P. Yang, Allan S.P. Chang, and S. Y. Lin, " Simultaneously Enhancing Internal and Extraction Efficiencies of GaN-Based Light Emitting Diodes via Chemical-Wet-Etching Patterned-Sapphire-Substrate (CWE-PSS)", 212th ECS Meeting, Washington, DC, USA

[11] H. H. Yen, **C. H. Chiu**, Peichen Yu, C. C. Kao, C. Lin, H. C. Kuo, T. C. Lu and S. C. Wang, W. Y. Yeh, "Micro-Photoluminescence from a Single InGaN-based Nano-Pillar Fabricated by Focus Ion Beam Milling", CLEO 2008 San Jose

[12] **C. H. Chiu**, B. S. Cheng, H. C. Kuo, T. C. Lu, S. C. Wang, H. W. Huang, C. C. Yu, C. H. Lin, "High Efficiency White LEDs with 2D Photonic Quasi-Crystal and Patterned Sapphire Substrate" CLEO/QELS2008 Conference, San Jose, USA, vol. 1-9 pp. 2315-2316